6-1-2014

Silicon nano wires solar cell

Sara Mohamed

The American University in Cairo

School of Sciences and Engineering

Physics Department

Silicon Nano Wires Solar cell

A Thesis in Physics

by

Sara Hussein Abdel Razek Mohamed

Submitted in Partial Fulfillment of the Requirements for
the Degree of Masters of Science in Physics

May 2014

Silicon Nano Wires Solar cell

By

Sara Hussein Abdel Razek Mohamed

A Thesis Submitted to the American Uinversity in Cairo in Partial Fulfillment of the Requirements for the Degree of Masters of Science in Physics

Under the Supervision of

Dr. Mohamed A. Swillam
Assistant Professor,
Department of Physics,
The American University in Cairo

Dr. Nageh K. Allam
Assistant Professor,
Department of Physics,
The American University in Cairo

May 2014

Abstract

Improving the optical absorption capability of solar cells' materials is a crucial factor in increasing their power conversion efficiency. To this end, the absorption can be enhanced by minimizing the reflection and the transmission out from the absorbing layer. While the reflection can be minimized using an antireflection coating, the transmission can be minimized by exploiting a light- trapping mechanism. In this thesis, the Si nanowires have been utilized to enhance the absorption and photocurrent without the need for antireflection coating, and provide high field localization, which in turn enhances the overall efficiency of the solar cell.

Vertically orientated single crystalline silicon nanowire (SiNW) arrays with controlled diameters have been fabricated via a metal-assisted chemical etching (MACE) method. The diameter of the fabricated nanowires is controlled by simply varying the etching time in HF/H_2O_2 solution. The fabricated SiNWs have diameters ranging from 117 to 650 nm and length from 8 to 18 μm. The optical measurements show a significant difference in the reflectance/absorption of the SiNWs with different diameters, where the reflectance increases with increasing the diameter of the SiNWs. The optical absorption also has been measured at different incident light angle to determine the best angle for absorption. The best absorption angle for different diameters was 10^o.The SiNWs showed significant photoluminescence (PL) emission spectra with peaks lying between 380 and 670 nm. The PL intensity increases as the diameter increases and shows red shift for peaks at ~ 670 nm. The increase or decrease of reflectivity is coincident with PL intensity at wavelength ~ 660 nm. The x-ray diffraction (XRD) patterns and high-resolution transmission electron microscope (HR-TEM) confirm the high crystallinity of the fabricated SiNWs. In addition, the Raman spectra showed a shift in the first order transverse (1TO) band toward lower frequencies compared to that usually seen for c-Si.

The current-voltage characteristics have also been investigated using photoelectrochemical cell. The measurements have been done in two electrolytes; 10% HF 10% and hydrobromic acid (40%) and bromine (3%). The measurements have been done for the fabricated Si nanowires with different diameters under dark and illumination conditions. The resulted photocurrent decreases with increasing the diameter of SiNWs, which has been explained based on the Debye length of SiNWs.

Full wave electromagnetic analysis has been performed using finite difference time domain simulations (FDTD) to confirm the effect of change of diameter on the optical properties of the nanowires. The simulation results show good agreement with the experimental findings for the SiNWs of different diameters. Also, the simulation has been done for different incident light angles to investigate the best incident angle that results in the highest absorption and minimum reflection.

Contents

List of Figures

List of Tables

ACKNOWLEDGEMENTS

I would like to express my special appreciation and thanks to my supervisor Dr. Mohamed Swillam for his guidance, understanding, and most importantly, patience during my graduate studies. You have been a tremendous mentor for me. I would like to thank you for encouraging my research and for allowing me to grow as a research scientist. Your advice on both research as well as on my career have been priceless. You have introduced me to a silicon nanowire research topic and provided me precious ideas, which made the work possible.

I would also like to thank my co-advisor Dr. Nageh Allam. He encouraged me to not only grow as an experimentalist but also as an independent thinker. He was always caring to guide me to develop my skills and experience. He was always updating me by the recent research and opportunities that could improve my understanding and my future career.

I would like to thank the members of my thesis committee, Dr. Salah Elseikah and Dr. Khalid Kirah; I also want to thank you for letting my defense be an enjoyable moment, and for your brilliant comments and suggestions, thanks to you.

A special thanks to my Family. Words cannot express how grateful I am to my mother and my brothers for all of the scarifies that you have made on my behalf. Your prayer for me was what sustained me thus far. I would also like to thank all of my friends who supported me in writing, and incented me to strive towards my goal.

Chapter 1

Introduction and Scope of the Thesis

1.1 Demand of Renewable energy

The demand for renewable energy has increased in the last few years due to the limited availability of the widely used fossil fuel. Various types of energy are shown in Figure.1.1. Although fossil fuel supplies most of energy due to its low cost, it is responsible of increasing the pollution in the environment. Moreover, it is considered as a scarce energy source. Every year, the consumption of oils in fossil fuels is over 11 billion tons. If the increase in the population is neglected and this consumption value is consumed every year, the oil will vanish by 2052. [1] If the production of gas is increased to fill the gap left by oil, there will be additional eight years added. However, the consumption of fossil fuel is increasing every year due to increase of population. Consequently, the fossil fuels will run out earlier.

There are many clean and cheap alternative sources of energy that can be used instead of fossil fuel. There are many considerations for using energy including safety, economic, and environmental issues. Solar energy is suitable for all the aforementioned considerations. The solution for increasing demand of energy is the renewable energy. The sources of renewable energy represent three fifths of the market's electricity of the world by the middle of the 21st century. [2]

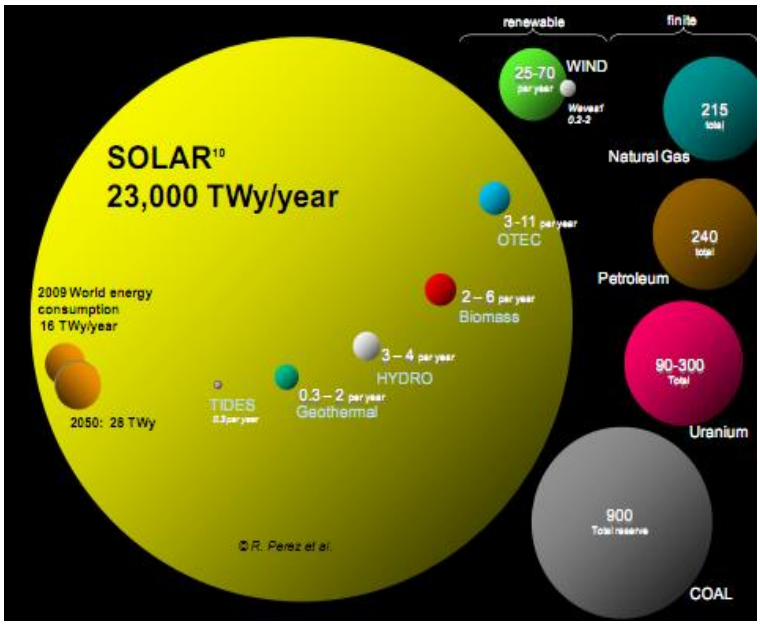

Figure 1.1annual summery of all types of energy. [3]

1.2 Photovoltaic solar energy: -

The solar radiation energy can be utilized for energy harvesting using two mechanisms; the first is through direct conversion from light to electricity, the second is based on exploiting the thermal effect via solar concentrators. For the first one the solar radiation is converted directly to electricity is called photovoltaic (PV) energy based on the photovoltaic effect. This effect implies the production of a potential difference at the junction that between two different materials. The solar concentrator systems concentrate the large area of sunlight by using mirror or lens. When the concentrated light is converted to heat, the electric power is generated through steam stations.

There are different applications that depend on using solar cells such as space and terrestrial application as presented in Figure.1.2. The efficiency of the solar cell, which used in space application, is measured before setting the solar cell on the space. Today, systems of PV have efficiency of 7 to 17 % for the terrestrial application.

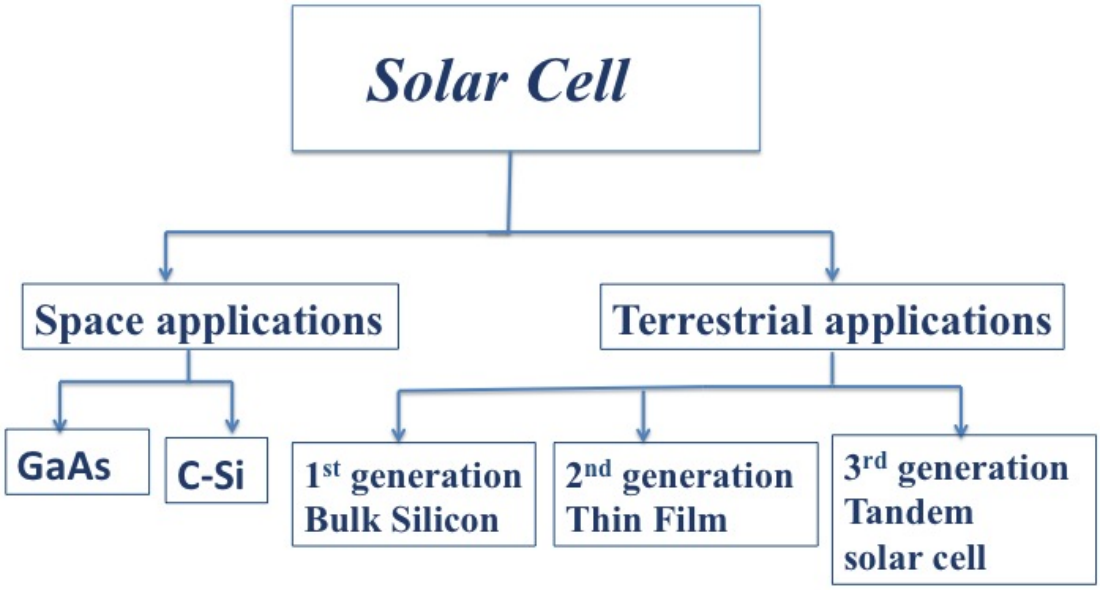

Figure 1.2 Overview of solar cell applications.

The rate of production solar cell is increasing from 1995 till now as shown in Figure.1.3. The global production was 0.6 GW at 1995 and has increased clearly from 2007 to be 10 GW.

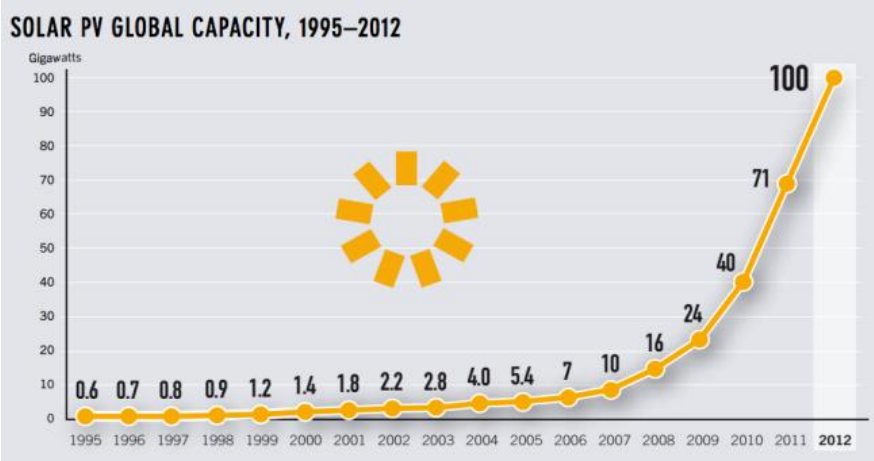

Figure 1.3 global production of electricity from solar PV 1995-2012. [3]

1.3 Silicon solar cell:

Silicon has the basic electronic characteristics suitable for solar cell applications. It is the second most abundant material on the earth that has electronic structure with a band gap appropriate for absorbing most of the visible light spectrum. Figure 1.4 shows the different structures of silicon that have recently been used for PV devices. [4] Although there are other types of solar cell materials such as copper indium selenide (CIS) and cadmium telluride (CdTe), silicon provides the higher light conversion efficiency. Figure1.5 shows the different light conversion efficiencies for different solar cell materials. The latest reports on the efficiency of monocrystalline Si is about 25 % on the lab scale, while the efficiency of CdTe is around 17%. Over the past ten years, research on Si-based solar cell has successfully improved the conversion efficiency from 12% to 15 %, while the efficiency of the CdTe solar cell has only ascended to 11%. [4]

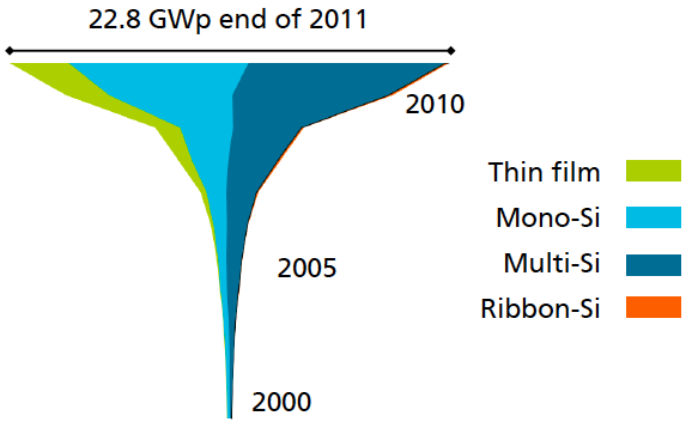

Figure 1.4 Global annual PV installation based on silicon. [4]

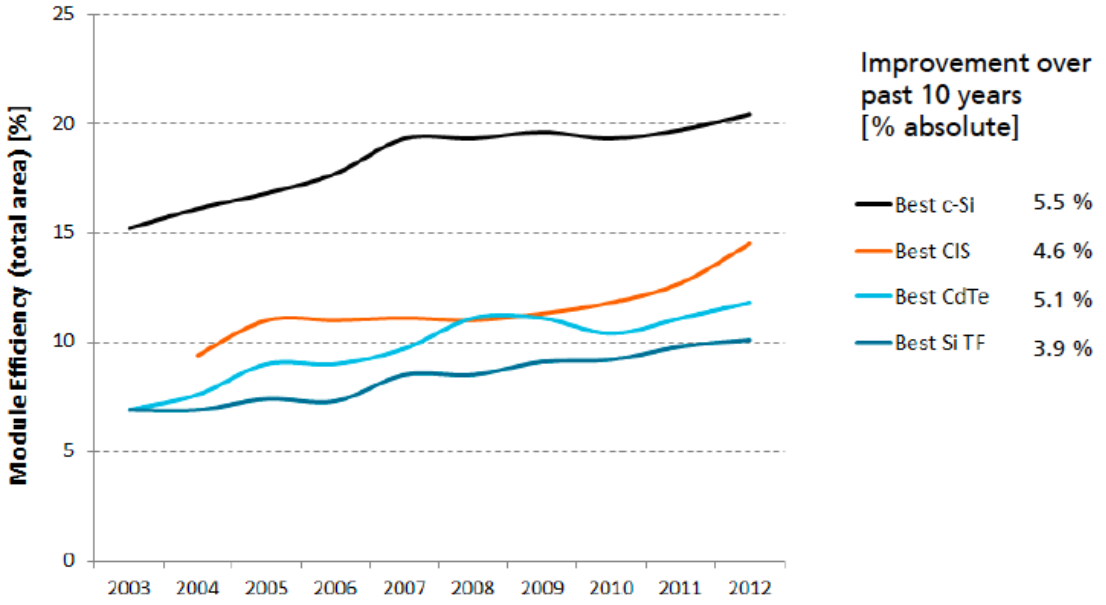

Figure 1.5 Efficiencies of different materials used for PV modules. [4]

The efficiency of solar cells has been improved through three generations. The first generation relied on bulk single-crystalline and multicrystalline silicon. It aimed at achieving high efficiency within Shockley-Queisser limit. [5] The second generation of solar cells aimed at reducing the fabrication cost through the development of thin film solar cell, however, the objective of fabrication of economically efficient solar cells was not greatly satisfied. Economically, the energy produced using the first and second-generation solar cells is more expensive than other sources of energy. Consequently, the need for a third generation solar cells, currently developing, combining recent advancements in materials and optical sciences is crucial. This generation of solar cells aims at reducing the cost and improving the efficiency of solar cells. The comparison between those three generations is represented in Figure 1.6.

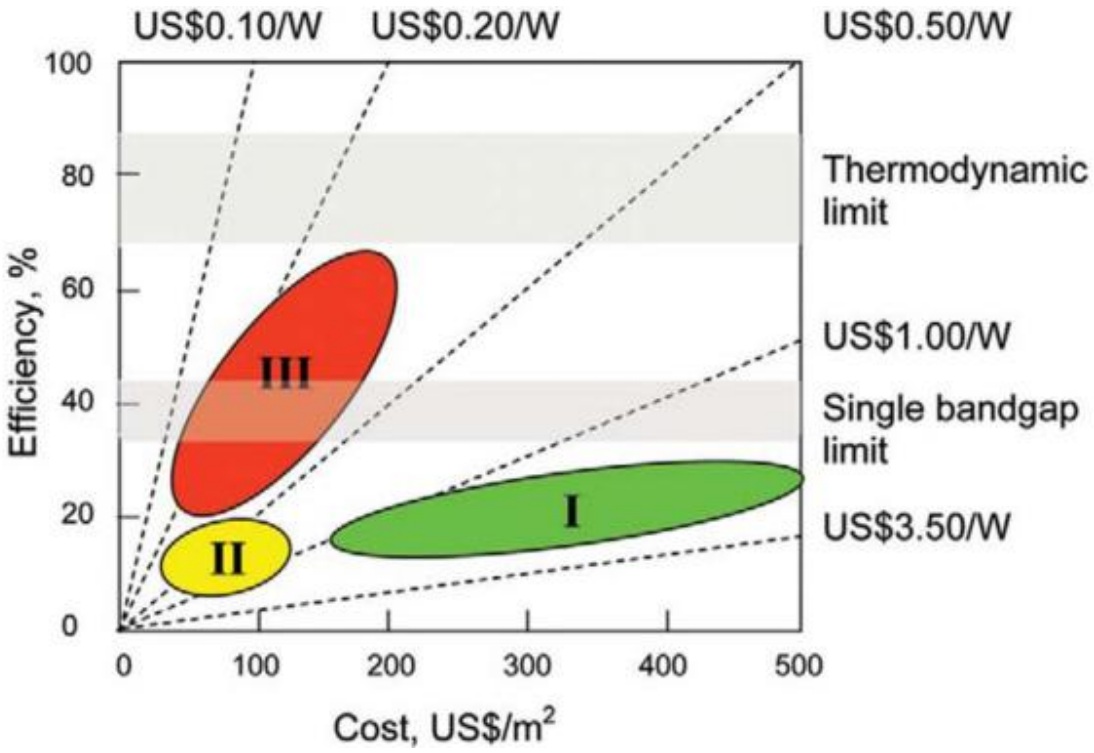

Figure 1.6 Efficiency Vs. Cost of three generations solar cell. [6]

The low efficiency of the current solar cells is mainly due to two mechanisms that are related to the cell material band gap energy. The first is the loss of photons having energies lower than the band gap that cannot excite electrons and form electron-hole pairs recombination (Figure 1.7(2)). The second is the loss of energy of higher energy photons in the form of heat as the semiconductor material takes only a discrete energy value. In this case, the hole and electron relax to the edges of the valance and the conduction bands (1 in Figure 1.7). Those two mechanisms are responsible for losing about 50 % of the incoming solar energy.

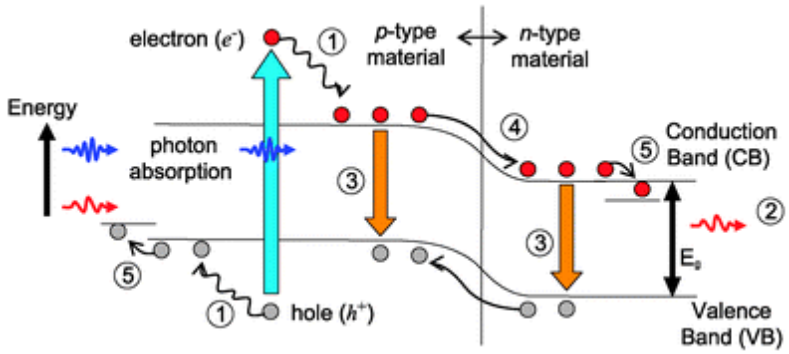

Figure 1.7 Summary of the loss processes in solar cell: (1) thermalization loss; (2) inability of absorbing photons with lower energy bandgap, (3) recombination loss, (4) and (5) junction and contact voltage losses. [7]

Third generation solar cells have been used to overcome the Shockley-Queisser limit (Figure 1.8). The fabrication of third generation of solar cell depends on fabricating multilayers of gallium arsenide or amorphous silicon for improving frequency conversion, multiple carrier ejection and hot-carrier effects.

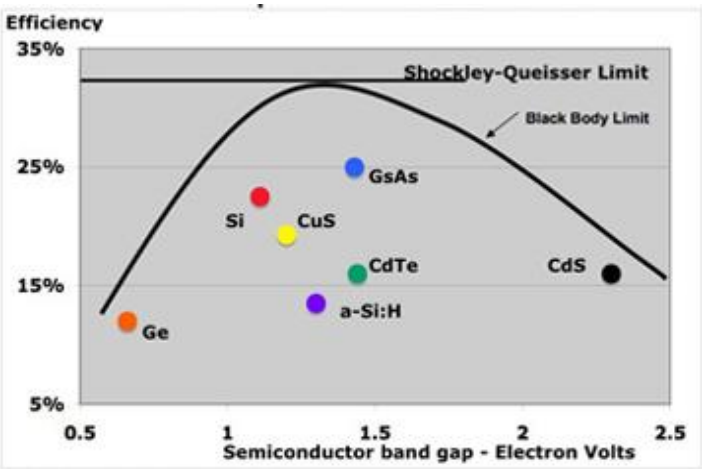

Figure 1.8 Relationship between bandgap of semiconductor and efficiency. [8]

Multiple junction solar cells enhance the efficiency through a composite of bandgap energies to absorb wider wavelength range of the light spectrum. [9] Actually, the increase of stack layers in solar cell increases the number of energy levels as suggested by Jackson in 1995.

The efficiency increased from 29% to 47.5% for tandem solar cells. For example, the efficiency of solar cells based on bulk silicon is 29%. [9] However, using bulk silicon in tandem solar cells increases the efficiency to 42.5% due to adding solar cells with bandgap 1.8 eV. Moreover, the efficiency of 47% can be achieved by adding two stack layers of other semiconductor materials with bandgaps of 1.5 and 2 eV to bulk silicon in tandem solar cells.

1.4 Scope and goals of thesis: -

The main goal of this thesis is studying, analyzing, fabricating and characterizations of Si nanowires (SiNWs) for energy harvesting application. The dimensions of the SiNWs have been optimized in order to maximize the absorption and provide high conversion efficiency. Metal assisted chemical etching (MACE) method has been used for fabricating SiNWs because it is the simplest and cheapest method. It is the first time for controlling the dimensions of SiNWs by MACE. The I-V characterizations of the

fabricated SiNWs with different diameters have been measured also by using photochemical cell. The photocurrent increases with decreasing of the diameter of SiNWs. The thesis is organized as follows:

Chapter 2 gives a wide general physical background for transport properties of semiconductor that used for solar cell applications and also summarizes the most important benefits gives for using SiNWs for photovoltaics.

Chapter 3 reviews three parts. Firstly, it reviews different methods that are used for fabrication SiNWs including bottom-up and top-down approaches. Secondly, it reviews the relevant literature on results of SiNWs simulations that have different lengths and its effect on changing the values of optical absorption. Thirdly, it reviews the relevant reports on using SiNWs for solar cell application including photochemical cell and p-n junction.

Chapter 4 demonstrates the experimental steps for fabrication SiNWs using MACE method and describes all used techniques for characterizing the fabricated SiNWs.

Chapter 5 represents morphology of the fabricated SiNWs with different dimensions. The optical, Raman spectroscopy and I-V characterizations of the SiNWs are also showed.

Chapter 6 shows the simulation results when the dimensions of SiNW array have been changed. The matching between experimental and simulated results are also presented.

Chapter 7 highlights the whole conclusion of thesis and discusses the future work.

References

[1] https://www.ecotricity.co.uk/our-green-energy/energy-independence/the-end-of-fossil-fuels Retrieved on the 9th of May 2014.
[2] Yousef, Tarik M. "Development, growth and policy reform in the Middle East and North Africa since 1950." Journal of Economic Perspectives (2004): 91-115.
[3] http://www.abb-conversations.com/2013/12/7-impressive-solar-energy-facts-charts/. Retrieved on the 13th of April 2014.
[4] http://www.ise.fraunhofer.de. Retrieved on the 13th of April 2014.
[5] Shockley, William, and Hans J. Queisser. "Detailed balance limit of efficiency of p- n junction solar cells." Journal of applied physics 32.3 (2004): 510-519.
[6] Beard, Matthew C., and Randy J. Ellingson. "Multiple exciton generation in semiconductor nanocrystals: Toward efficient solar energy conversion." Laser & Photonics Reviews 2.5 (2008): 377-399.
[7] Van der Ende, Bryan M., Linda Aarts, and Andries Meijerink. "Lanthanide ions as spectral converters for solar cells." Physical Chemistry Chemical Physics 11.47 (2009): 11081-11095.
[8] http://solarcellcentral.com/limits_page.html . Retrieved on the 13th of April 2014.
[9] Birmann, Katrin, et al. "Optical characterization of random pyramid texturization." Small 100 (2011): 11-2.

Chapter 2
Physical Background

2.1 Introduction

The basic function of solar cell is converting the light into the electricity. In most cases, semiconductor material is used for solar cell. The energy conversion process consists of two steps. When the semiconductor absorbs photons from sunlight, the electron-hole pairs are produced and charge carrier separation has occurred. The p-n junction, in most cases, is responsible of charge carrier separation. Consequently, the properties of the semiconductor should be discussed to recognize the principle of p-n junction. [1]

2.2 Basic properties of semiconductor: [2-6]

2.2.1 Energy band and Concentration of carrier

Usually, every atom has electrons that are existed in separated energy levels. When atoms start in forming crystal, electrons approach to each other. Thus, a closed space exists between energy levels due to atomic interaction. There are two bands those electrons move between them, the lower band (valence band (Vb)) and the upper band (conduction band (Cb)). The energy gap that exists between theses two bands is called band gap, E_g. At temperature of 0K, all electrons are in the valence band, while the conduction band is empty. At room temperature by thermal vibrations, some bonds can be broken. Consequently, the electrons move to the conduction band. Figure 2.1 shows the energy bands for semiconductor where E_v and E_c are the energies of the top of the valance band and bottom of the conduction band, respectively. As the holes have opposite charge to electrons, the kinetic energies of holes and electrons are measured downward from E_v and upward from E_c, respectively.

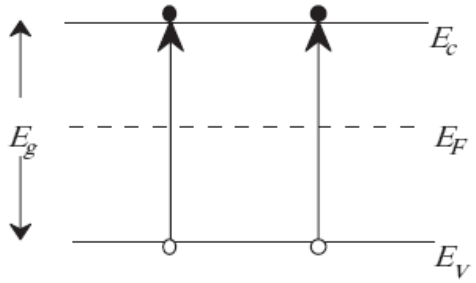

Figure 2.1 Representation of energy bands in intrinsic semiconductor. [7]

2.2.2 Mobility

The electrons in atom can be excited thermally. After thermal excitation, the motion of the electrons is in all directions. This motion causes collision between excited electrons and surrounded atoms (e.g. lattice atoms or impurity atom). The electrons loose their

energies gained from the electric field. By applying electric field E, the electron has a force $-qE$ where the q is an electric charge of electron $(1.6 \times 10^{-19} C)$. This force accelerates in the opposite direction of E. The produced velocity by E is called the drift velocity, v_n.

2.2.3 Drift current

When applying electric field E to an n-type semiconductor with concentration n and cross-sectional area A as shown in Figure 2.2, the total drift current is the summation of the hole current density J_p and the electron current density J_n and is given by:

$$J = J_n + J_p = (nq\mu_n + pq\mu_p)E = \sigma E \quad (1)$$

where σ is the conductivity, μ_n and μ_p are the electron and hole mobility respectively.

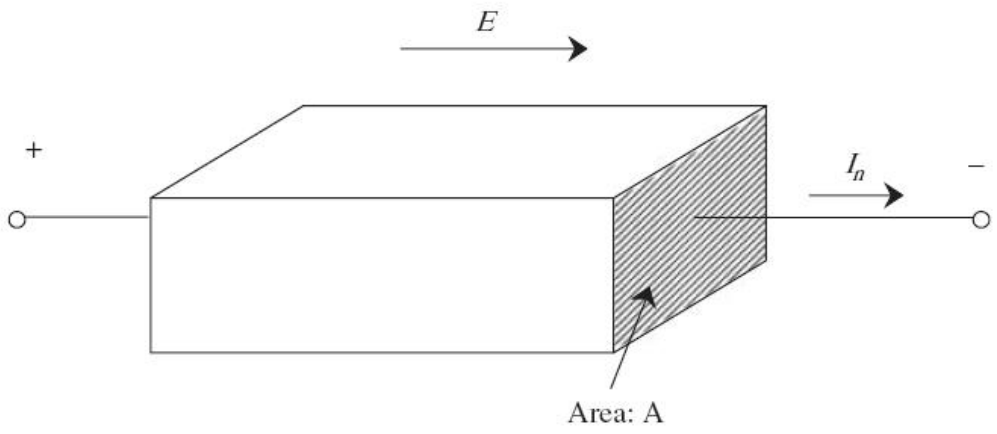

Figure 2.2 Sample of semiconductor to show electron current density. [7]

As shown in Figure 2.3, by applying E to the semiconductor, the gradients of two bands take place where the holes and the electrons flow to decrease the potential energy. The electrons and holes move toward in opposite direction. The direction of the current density of holes and electrons is the same.

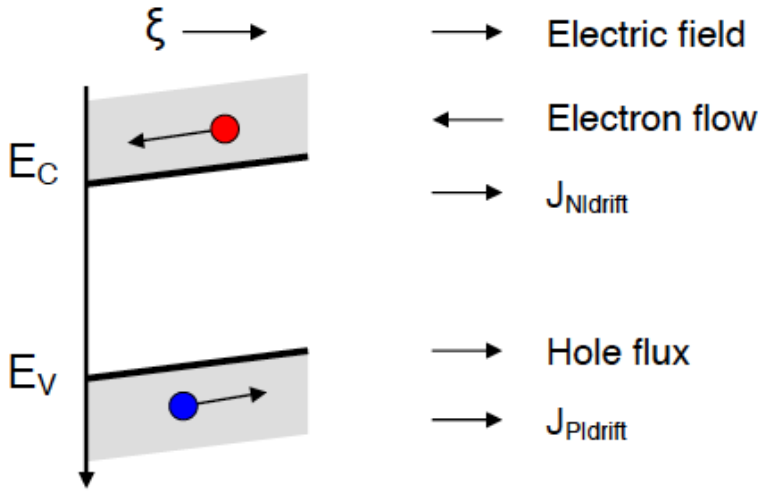

Figure 2.3 Drift of holes and electrons in a semiconductor [7]

2.2.4 Diffusion Current:

In semiconductor, when there is a difference in concentration of electrons, the electrons transfer from the area of high concentration to the area of low concentration. The resulting current, in this case, is called the diffusion current. The diffusion current could be demonstrated considering the concentration of electrons with 1D gradient in x-direction as shown in Figure 2.4a.

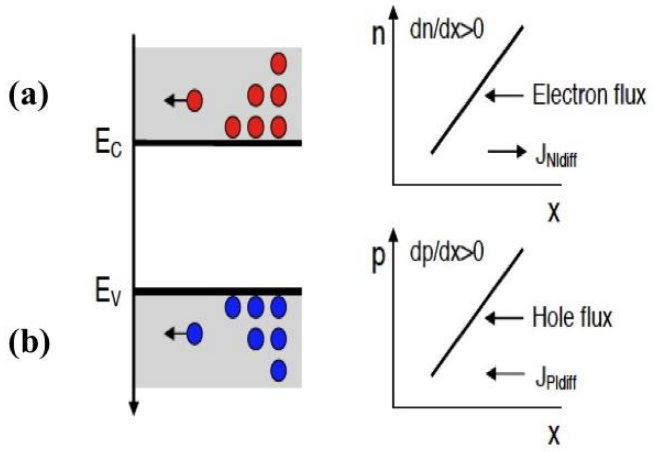

Figure 2.4 Diffusion of electrons and (b) holes.[7]

If the concentration of electrons increases, the current flows in the x-direction. Similarly for holes, if the concentration of holes increases, the holes diffuse in the opposite direction of positive x.

The relationship between the drift and diffusion current, is given by:

$$D_n = \frac{kT}{q}\,\mu_n \tag{2}$$

where D_n is the diffusion coefficient of the electron.

2.2.5 Optical Absorption:

There is a relationship between energy of photon $h\upsilon$ and the wavelength λ of light that is expressed by:

$$\lambda\,(\mu m) = \frac{c}{\upsilon} = \frac{hc}{h\upsilon} = \frac{1.2398}{h\upsilon\,(eV)} \tag{3}$$

where h is the plank's constant, υ is the frequency of light, c is the speed of light in vacuum, and λ is the wavelength of solar light that is in region between 0.3 and 3 μm. When the semiconductor is under illumination, there are two cases. First, if the energy of photon is lower than the semiconductor' band gap, the semiconductor is transparent to the incident light. Second, if the energy of photon is larger than the semiconductor' band gap, an electron-hole pair is created due to absorption of photon. Thus, the electron transfers from Vb to Cb (Figure 2.5).

When $h\upsilon$ is bigger than the energy of band gap, the electron-hole pair is generated. The excess energy gives additional kinetic energy to the electron or hole that is dissipated in the form of heat in semiconductor.

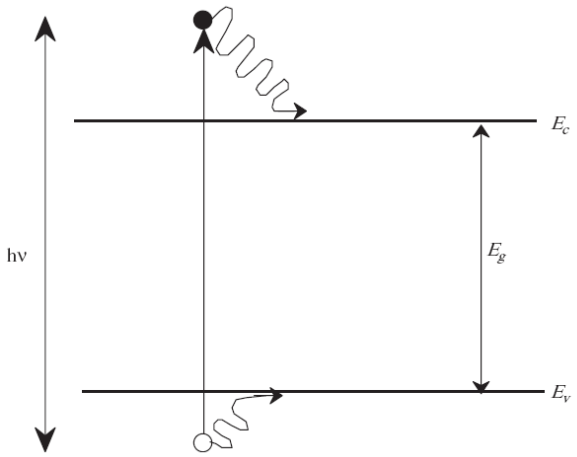

Figure 2.5 Absorption process in semiconductor [7]

2.2.6 Recombination in Semiconductor

After turning off the light source from semiconductor, the excess charge carriers are dissipated. This process is called recombination process. This process can be direct Figure 6a or indirect in bulk material by localizing the energy states in the forbidden energy gap Figure 6b and Auger recombination Figure 6c. First, direct recombination, which is inverse of absorption, usually occurs in semiconductor with direct band gap. When an electron transfers from Vb to Cb, an electron - pair is dissipated and the photon is emitted. In the thermal equilibrium case, the rate of recombination is equal to the rate of generation that is $\beta n_{n0} p_{n0}$ for n-type semiconductor where β is the proportionality constant n_{n0} and p_{n0} are the concentration of electron and hole, respectively. The generation rate is the rate of generating electron-hole pair per unit volume per unit time. The recombination rate depends on the number of holes in Vb and electrons in Cb. When excess carriers in semiconductor are generated under illumination, the rate of recombination is increased to βnp. Thus, the net rate of recombination is proportional to the concentration of excess minority carrier. $\tau_p = 1/\beta n_{n0}$ is the lifetime of minority carrier (holes) in n-type semiconductor. Similarly, $\tau_n = 1/\beta p_{p0}$ is the lifetime of minority carrier (electrons) in p-type semiconductor

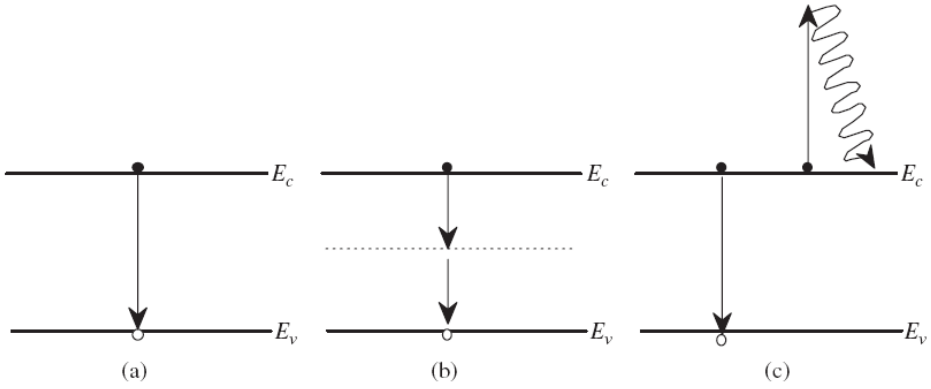

Figure 2.6 Representation of different processes of recombination in semiconductor: (a) direct recombination, (b) indirect recombination, and (c) Auger recombination. [7]

For indirect recombination it usually occurs in semiconductor with indirect band gap. The lifetime of the minority carrier does not depend on the concentration of the majority carrier.

For Auger recombination Figure 6c, the electron gives its extra energy to another electron in Cb or Vb. The excited electron transfers to a higher energy level. When the excited electron relaxes to the band edge, the excess energy will give up in the form of heat.

2.2.7 Continuity Equation

In semiconductor, the drift current, the generation, the diffusion current and the recombination processes occur altogether. For deriving the relationship between all processes in 1D, let's consider that there is small slice with area A and thickness dx as

shown in Figure 2.7. Discussing the current density of electron at x is $J_n(x)$, the increase of electron in this volume per unit time will be the total net carrier generation in the slice and net flow into the slice.

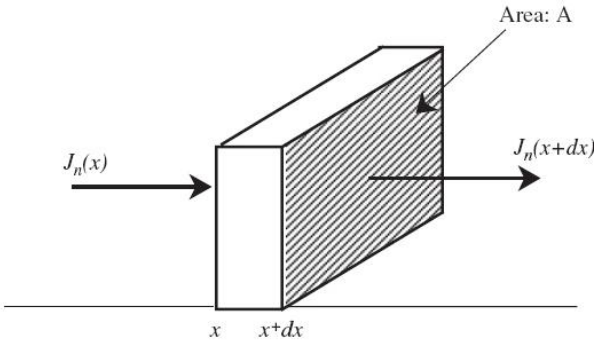

Figure 2.7 Expression of the continuity equation by a schematic of flowing electron in small volume. [7]

The concentration of the excess carrier in steady state can be calculated by discussing that the generation of excess carrier occurs at x = 0 in an n-type semiconductor and the continuity equation is

$$D_p \frac{\partial^2 p_n}{\partial x^2} - \frac{p_n - p_{n0}}{\tau_p} = 0 \tag{4}$$

Because the concentration of the excess carrier should decrease when the applied E is zero, the general solution is:

$$p_n - p_{n0} = \Delta P(0)\, e^{-x/L_p} \tag{5}$$

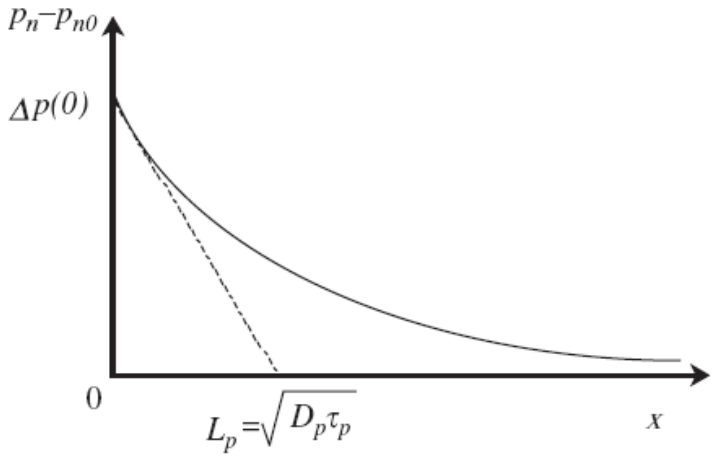

Figure 2.8 Steady state excess carrier concentration profile when the excess carrier is generated at x = 0. [7]

where $L_p = \sqrt{D_p \tau_p}$ is the diffusion length of holes and $\Delta P(0)$ is the concentration of excess carrier at x =0. Figure 2.8 shows how the concentration of excess carrier

distributes in steady state. The diffusion length of electrons also is $L_n = \sqrt{D_n \tau_n}$. The diffusion length is the average length in which carriers can move before recombination. For heavily doped semiconductor, the diffusion length is short and the rate of recombination is high. Semiconductor material with high diffusion length has long lifetime. The lifetime is important for determining the quality of semiconductor when it is used for solar cell application.

2.3 Basic principles of semiconductor solar cells

There are two methods for defining current-voltage characterization of semiconductor. The first method is the p-n junction solar cell. In this junction, the photoactive junctions are p-n junctions between two semiconductors. The n-type in junction is covered by a metal layer to act as cathode. The p- type is covered with a metal layer to act as anode. The second method is photochemical cell in which the photoactive junctions are between semiconductor and aqueous solution. It is a minority carrier device with p-type acting as a cathode and n-type acting as anode.

2.3.1 Electric properties of p-n junction solar cell

2.3.1.1 Built-in Potential

The function of p-n junction is separating charges of holes and electrons that are generated by light. Figure 2.9 shows the majority carriers for n- type and p-type semiconductor and the energy bands. When the p-n junction is created, the diffusion of carriers occurs due to the carrier concentration gradients. The diffusion from n-type to p-type occurs for electrons, and from p-type to n-type occurs for holes. When the diffusion of holes and electrons occurs, a layer without mobile charge carriers is created.

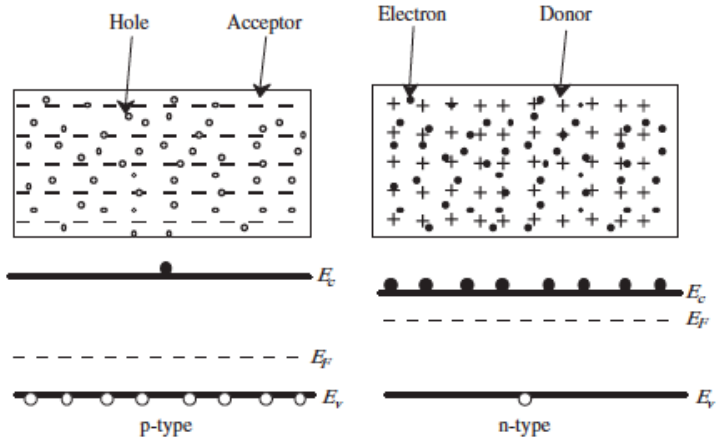

Figure 2.9 Energy band and majority carriers of n-type and p-type semiconductors. [7]

This diffusion obstructs the pass of the electric field that is created by the space charge as shown in Figure 2.10(a). Because of passing the electric field through junction, the drift

current is balanced and the thermal equilibrium is set up. At equilibrium, the Fermi levels of n- type and p-type semiconductor are equal as shown in Figure 2.10 (b).

At thermal equilibrium, the existed potential difference is called the built-in potential $V_{b,}$ which is between the p-type and n-type semiconductor and is expressed by

$$V_b = \frac{kT}{q} ln \frac{N_A N_D}{n_i^2} \quad (6)$$

where N_A and N_D are the concentrations of the acceptors and donors in p-type and n-type semiconductors, respectively.

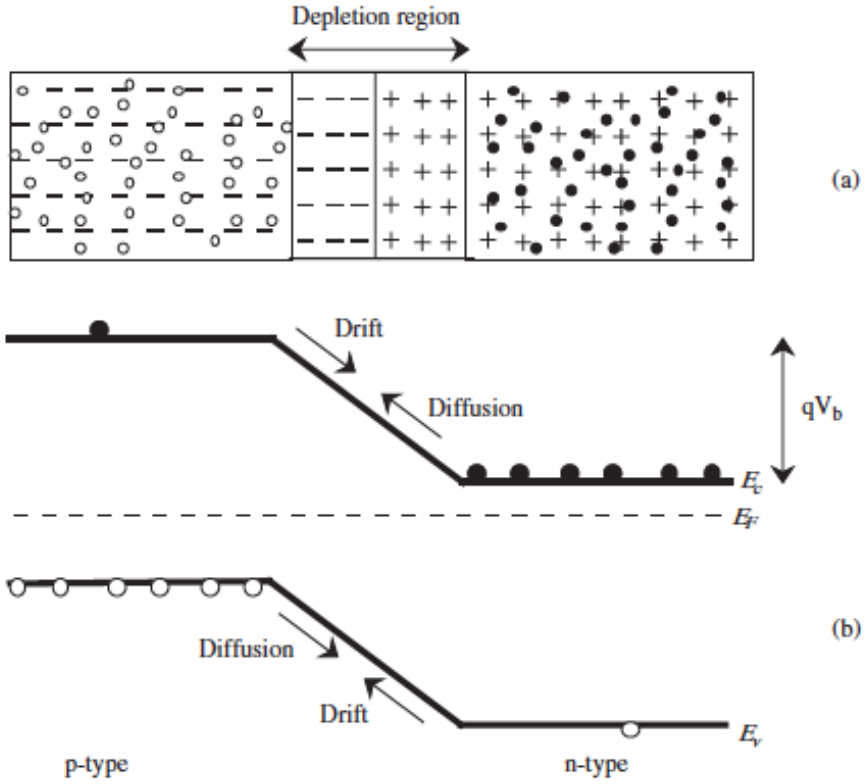

Figure 2.10 (a) Schematic structures of p-n junction and (b) its energy band diagram in thermal equilibrium. [7]

2.3.1.2 Depletion Region

The depletion region in the p- n junction is defined as the transition region that is free of mobile carriers (Figure 2.10 (a)). Although the area behind the depletion region is electrically natural, the ionized acceptor and donor ions charge the depletion region. The width of depletion layer with a layer of p-type of doping N_A for x<0 and n-type of doping N_D for x>0 is presented in Figure 2.11. By neglecting the transition region, x_p and x_n indicate the width of depletion layer of p- and n-side, respectively.

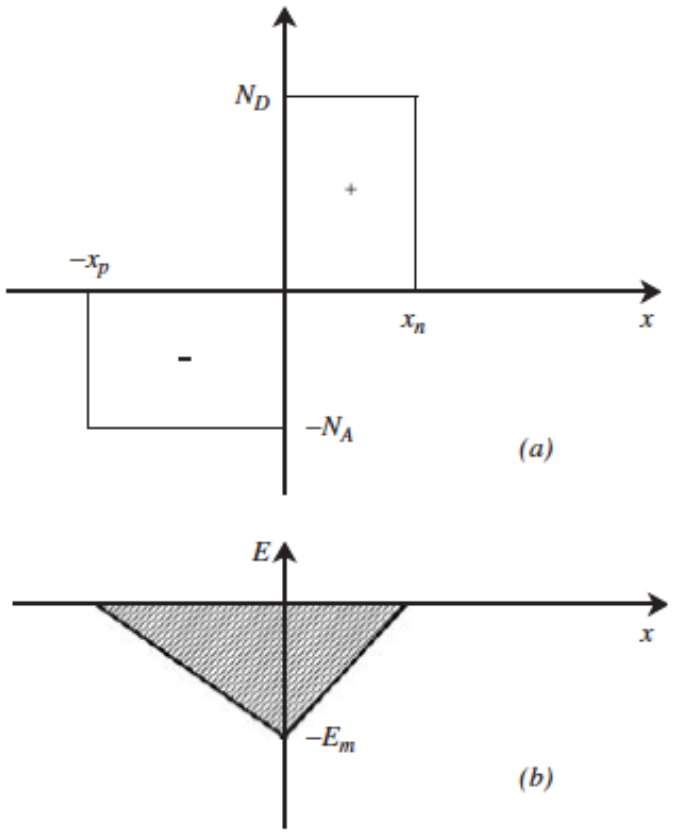

Figure 2.11 (a) the space charge and (b) the distribution of the electric field at the p-n junction. [7]

The total built-in potential will equal the area of the field triangle that is shown in Figure 2.11 (b) and is expressed by

$$V_b = = \frac{1}{2} E_m w \tag{7}$$

The total width of depletion w is expressed by

$$w = \sqrt{\frac{2\varepsilon}{q}\left[\frac{1}{N_A} + \frac{1}{N_D}\right] V_b} \tag{8}$$

The width of the depletion layer increases with the decrease of concentration of donor or acceptor.

2.3.1.3 I-V characteristics in dark

By applying a bias voltage V_F to n-side and p- side, the applied voltage decreases the potential through the depletion region as presented in Figure 2.12 (a).

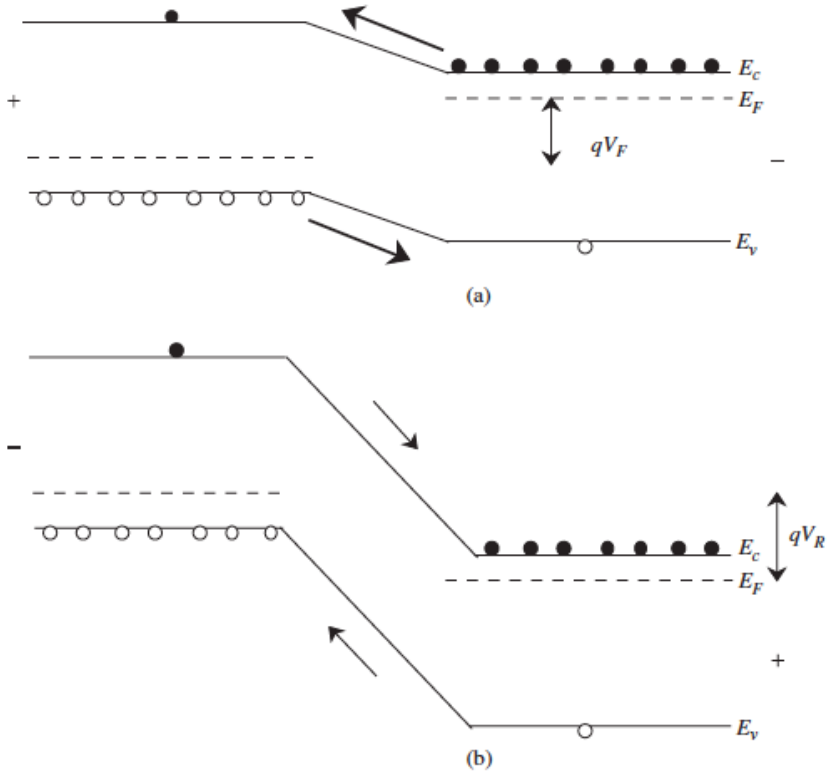

Figure 2.12 Energy band diagram under (a) forward bias and (b) reverse bias. [7]

The resulting polarity is known as the forward bias. In this situation, the drift current decreases. The diffusion of holes and electrons increases from the p-side to the n-side and from n- to p-side, respectively. Thus, the injection of the minority carrier occurs in which holes are injected into the n-side and electrons are injected into p-side.

Therefore, the total current density is given by

$$J = J_n + J_p = \left(\frac{q\,D_p p_{n0}}{L_p} + \frac{q\,D_n p_{p0}}{L_n}\right)\left(e^{qV_F/kT} - 1\right) = J_0\left(e^{qV_F/kT} - 1\right) \quad (9)$$

where J_0 is the saturation current density, and the L_n is the diffusion length of electrons in the p-layer.

If a reverse voltage V_R is applied across the junction, the voltage across the depletion region is increased as presented in Figure 2.12 (b). Thus, the current density under a reverse bias is expressed as

$$J = J_0\left(e^{-qV_R/kT} - 1\right) \quad (10)$$

2.3.1.4 Influence of recombination and generation

There is no any p-n junction with ideal current-voltage characteristic. Every p-n junction has two processes in the depletion region. These two processes are the generation and recombination of carriers. In the case of reverse bias, the generation of holes and electrons occur through the energy state in the forbidden energy gap. In the case of the forward bias, the carriers recombine in the forbidden energy gap.

The forward current density of the p-n junction is expressed as

$$J = J_0\left(e^{-qV_F/nkT} - 1\right) \tag{11}$$

where n is the ideality factor.

2.3.1.5 Current – Voltage characterizations under illumination

When a p-n junction is under illumination, electron - hole pair is generated if the energy of photons is higher than the energy of band gap. The quantity of generated electron – hole pair is relative to the light intensity. The drift of holes toward the p- and electrons toward n-side occur in the depletion region due to the electric field in the depletion region. The flow of current is the result of the charge separation from n- to p-side when an external wire is short-circuited as shown in Figure 2.13.

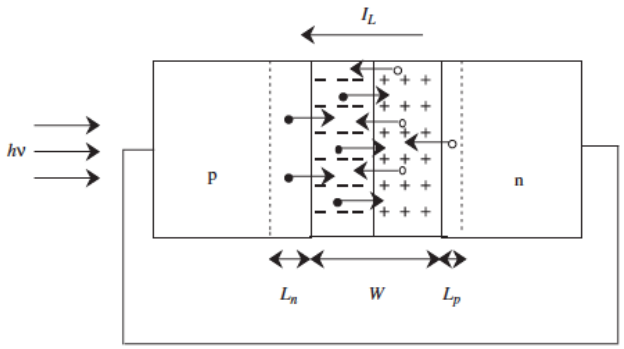

Figure 2.13 Schematic presentation of carrier flow of p–n junction under illumination in the case of short-circuited. [7]

If the p-n junction is under illumination, which is open-circuited, the voltage should be generated from charge separation. Figure 2.14 (a) and (b) show diagrams of the energy band for p-n junction in the short- and open- circuited, respectively. When the n- and p-sides are short- circuited, if the series resistance is zero, the resulting current is equal to the photogenerated current I_L , which is known as the short-circuit current I_{sc} . If the p- and n – sides are isolated, holes and electrons move toward the p- and n-side, respectively. The resulting voltage is called the open-circuit voltage V_{oc}. Figure 2.15 presented the I-V characterization under dark and illumination.

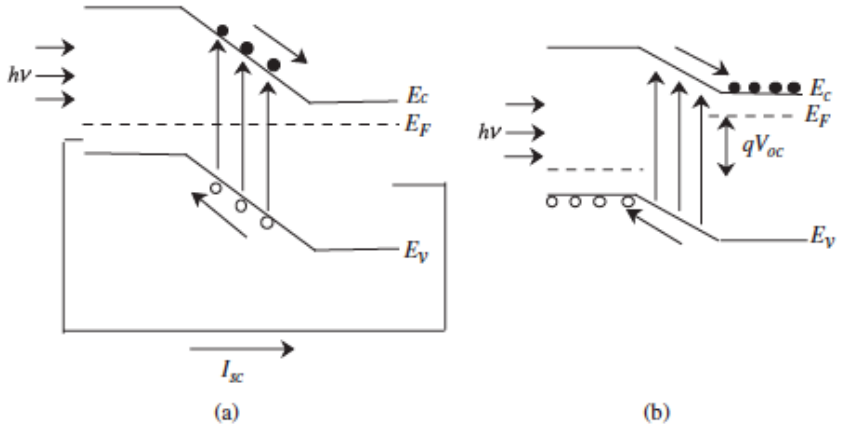

Figure 2.14 Diagrams of energy bands for p-n junction under illumination (a) the short-circuited and (b) open-circuited current. [7]

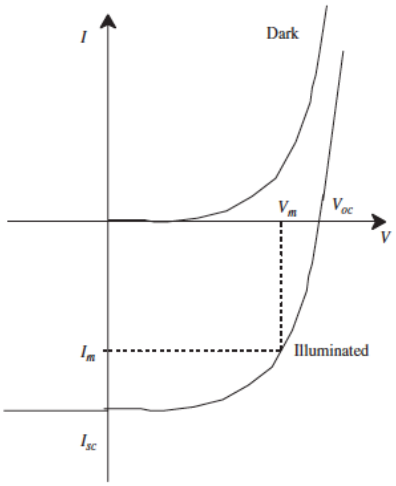

Figure 2.15 I-V curves of p-n junction under darkness and illumination. [7]

If the area of the solar cell equals unity, the I-V characteristic of p-n junction under illumination is expressed as

$$\mathrm{I} = I_0 \left(e^{qV/nkT} - 1\right) - I_{sc} \tag{12}$$

When I = 0, which is the open circuited, the voltage is expressed as

$$V_{oc} = \frac{nkT}{q} ln \left(\frac{I_{sc}}{I_0} + 1\right) \tag{13}$$

When the solar cell is operated under a condition that gives the maximum current I_m and the maximum voltage V_m at the optimal operation point as shown in Figure 2.15.

The Fill factor FF of the solar cell is defined as

$$FF = \frac{V_m I_m}{V_{oc} I_{sc}} \tag{14}$$

The conversion efficiency η is given by

$$\eta = \frac{V_m I_m}{P_{in}} = \frac{V_{oc} I_{sc}\, FF}{P_{in}} \tag{15}$$

where P_{in} is the total incident power of light.

2.3.2 Photoelectrochemical Cell:

2.3.2.1 Introduction: -

Photochemical cell is one of the chemical means for converting solar energy. It is very simple and it consists of two electrodes only, one from semiconductor and one from metallic. The two electrodes are immersed into specific electrolyte and exposed to light. The electrode of semiconductor can absorb light and affect on the separation of charges to produce current. This type of cell is very effective in energy conversion process. The efficiency of energy conversion in this cell is exceeding 15 %. [8-11] In this type of cell, the semiconductor absorbs light and the interface between the liquid and the semiconductor is the essential factor for energy conversion process.

When the semiconducting electrode is immersed in the liquid, the electric field is produced at the interface between solid/liquid. If the semiconducting electrode absorbs incident sunlight, the excited electrons have been created. These electrons are attracted or repelled by the electric field (relaying on the sign) to produce current. In photochemical cell also, free energy is responsible for separating charges for energy conversion process.

The overall process in the cell does not depend only on the semiconducting electrode, but also on metallic counter electrode. If the reaction at the semiconducting electrode is opposite of those at the metallic counter electrode, there is not any net chemical change in the cell. Consequently, the photocurrent will produce only the electrical power in the circuit.

There are three parameters that characterize the performance of the formed photochemical cell (Figure 2.16). First parameter is the current that passes through the external circuits. If there is no current in the external circuits, there is no extraction of energy. The current can be measured when trivial work demanded. This current is called the short circuit current (I_{sc}). It flows in the presence of a direct short circuit across two electrodes. The second parameter is the voltage that is measured at open circuit. The open circuit voltage (V_{oc}) measures the maximum Gibbs free energy of the cell. The third parameter is the fill factor (ff), it is the rate at which the current approaches the open circuit value. The fill factor measures the maximum power of the cell.

2.3.2.2 Charge transfer at junction of Semiconductor/Liquid

In the junction between semiconductor and liquid, the equilibrium state is produced by flowing charges. For using semiconductor/liquid junction in energy conversion process, this type of charge is a precondition. This charge can describe the process of storing energy in the photochemical cell. For getting electrical energy from solar energy, the flow of non-equilibrium current must be present through this junction.

2.3.2.3 - I-V characterization for a semiconductor/Liquid interface

The charge transfer process that at semiconductor electrode can be presented by the following chemical equation:

electron in solid	+ acceptor in solution	⇔	electron vacancy in solid	+ donor in solution	(16)

In Eq. 16, the forward and reverse reactions represent the reduction and oxidation reaction of the acceptors and donors, respectively. In the chemical system for n-type semiconductor electrode, at equilibrium, the net destruction of reactant is not occurred. At equilibrium, the flowing rate of electrons from semiconductor into solution in semiconductor/liquid junction must equal to the rate of flowing electrons from solution to semiconductor (Figure 2.16).

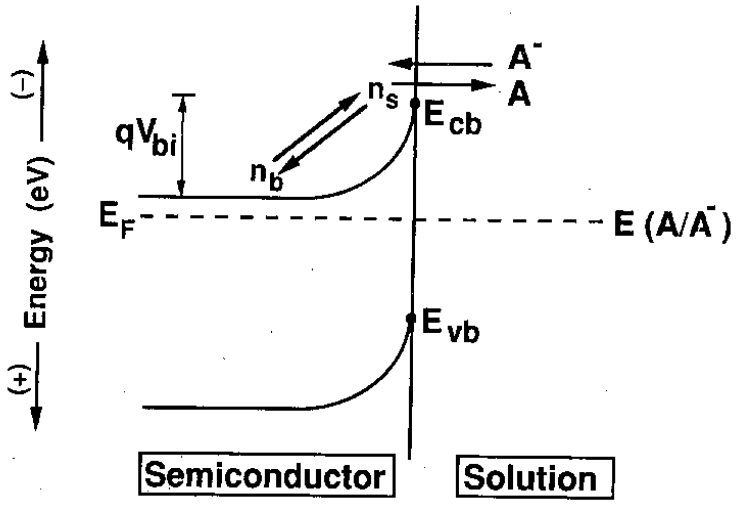

Figure 2.16 an energy diagram that shows the transfer of charge at equilibrium for the interface semiconductor/liquid. At equilibrium, the concentration of the surface electrons (n_s) depends on the concentration of surface electron in the bulk (n_b) and the built-in voltage (V_{bi}). The reduction reaction is the forward reaction (A) and the oxidation reaction is the reverse reaction (A^-). [8]

The simplest model of electron transfer across the interface between a semiconductor/liquid assumes that the bimolecular kinetics can be applied to the charge-

transfer reaction. In this model, there is a linear relationship between the current and two concentrations. The first one is the concentration of electrons that is near to the surface of semiconductor (n_s). The second is the concentration of acceptors ions that has the ability of capturing charges at the surface of semiconductor (Figure 2.16).

The solution now is containing a redox couple A/A^-. The reduction reaction is the forward reaction (A). In this reaction, the electrons transfer from semiconductor to the acceptor. The oxidation reaction is the reverse reaction (A^-). In this reaction, the electrons transfer from the donors to Cb of the semiconductor. In this case, the electron enters an empty state of solid; as a result, the concentration of this state can be taken as a constant.

At equilibrium, the forward rate must equal to the reverse rate. The concentration of electrons that are at the surface of semiconductor at equilibrium can be represented by the quantity n_{so}.

2.3.2.4 The dark Current -Voltage characterization of semiconductor/liquid junction:-

The current is the rate of electron transfer multiplied by the area of the electrode (A) and the charge on an electron. In the case of $n_s > n_{so}$, a reduction occurs at surface of the electrode in which electrode donates electrons to solution; as a result, the negative current will flow.

At equilibrium, the concentration of electrons at the semiconductor surface is expressed by

$$n_{so} = n_b \exp\left(-\frac{q V_{bi}}{KT}\right) \quad (19)$$

By applying a voltage to the semiconductor, the voltage drop in the semiconductor deplation region is $V_{bi} + V$. From equilibrium, an analogus Boltzman can be obtained

$$n_s = n_b \exp[-\frac{q (V_{bi}+V)}{KT}] \quad (20)$$

The above equation shows that the electron concentration at the surface of semiconductor could be decreased or increased depending on additional voltage, because this voltage controls the concentration of carrier at the surface.

The relationship between voltage and current in this type of junction is given by

$$I = -Cn_{so}\left[\exp(-\frac{q V}{KT}\right) - 1] \quad (21)$$

Equation (21) showed that there are two cases for studying the I-V properties of semiconductor. For V<0, the relationship between current and voltage is exponential. For V>0, the voltage has the opposite sign. As mentioned before, the net current of the semiconductor/liquid junction is the difference between the forward and reverse interface

of the rate of charge-transfer. Physically, when voltage is larger than zero, the concentration of surface electrons decreases because the electric potential drop increases in the semiconductor. Consequently, the rate of electrons that leave from the semiconductor decreases (Figure 2.17a). However, the rate of electrons that enters the semiconductor remains constant. This direction of voltage is called reverse bias and the current will be independent of the applied voltage. In reverse bias, the electrons are injected into the semiconductor from the solution.

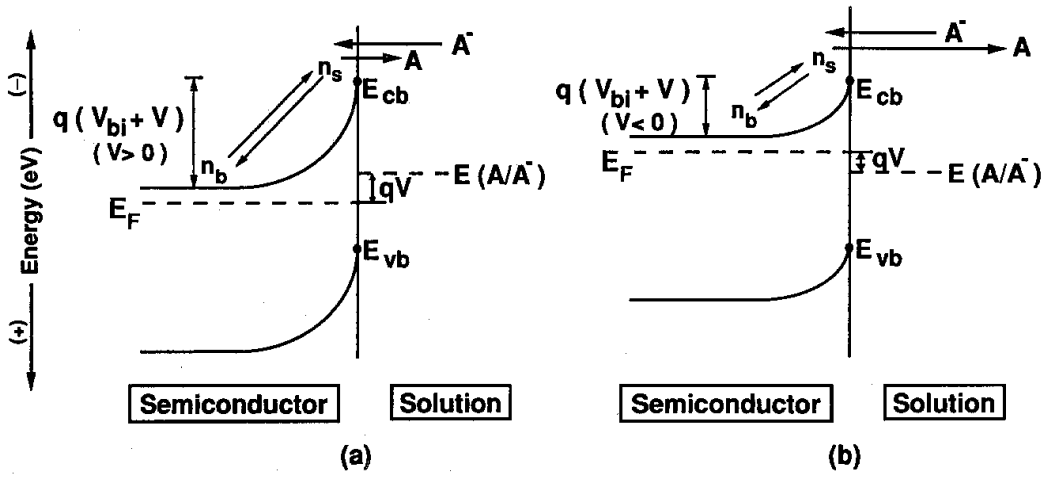

Figure 2.17 an energy diagram at equilibrium of the process of charge transfer at an n-type semiconductor/liquid interface when applying (*V*) to the semiconductor electrode. (a) the decrease of the forward reaction rate is porportinal to its equilibrium value, while the rate of the reverse reaction remains constant. (b) the forward bias condition (i.e., where V <0). [8]

For forward bias (V<0) , the concentration of the surface electrons increases. In this case, the electrons that leave semiconductor will increase; as a result, forward bias has been obtained (V<0 for n-type semiconductor). The concentration of the surface electrons increases with increasing the bias expontially. The concentration of reactant increases and the forward rate of the charge transfer increases also (Figure 2.17b). This increase does not affect on the reverse bias. Here, the net current depends on the applied voltage as equation (21). Eq.21 can also be written with one constant, as follows:

$$I = -I_o \left[\exp\left(-\frac{qV}{KT}\right) - 1\right] \tag{22}$$

where $I_o = Cn_{so}$ and I_o is called the exchange current in which current is at equilibrium. it is positive quanitiy. This parameter is responsible of transforming products and reactants and vice versa at equilibrium. I_o depends on the value of the concentration of surface electrons at equilibrium. At equilibrium, smaller exchange current should flow.

Equations 21 and 22 are called diode equations that can describe the current voltage characteristics. The interface of semiconductor/liquid can be described by diode equations when the rate of interfacial charge tranfer is used for determining step for charge movement. In this case, the applied V varies the concentration of surface electrons of semiconductor, so the relationship between current and voltage of a

semiconductor/liquid interface is affected (Figure 2.18). This behaviour of diode would not have procced for other surfaces or metal electrode because the concentration of the surface electron does not depend on the applied voltage.

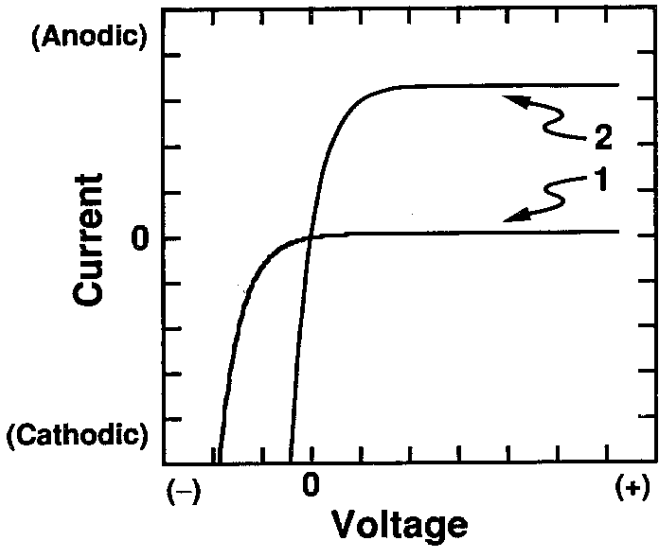

Figure 2.18 the current-voltage curves of an n-type semiconductor/liquid junction in the dark. The I_0 in curve 1 is lower than curve 2. [8]

2.3.2.5 The current-voltage characterization under illumination: -

A- Basic current-voltage equations under illumination:

Firstly, current comes from two components: majority carriers and minority carriers. Under illumination, the absorbed photons create both minority and majority carriers. For majority carriers, after absorbing sunlight, the concentration of majority carriers is small compared to that which existed by thermal ionization of dopant atoms. In other words, the behavior of majority carrier does not change under illumination. On the contrary, the concentration of the minority carriers changes under illumination. As mentioned, semiconductor can separate majority carriers from minority carriers when E is flowing through it. This electric field drives the minority carriers towards the solid/liquid interface. In the depletion region, electric field is strong enough to separate and collect the photogenerated minority carriers.

The current of the photogenerated minority carrier I_{ph} is equal the absorbed photon by semiconductor multiplied by the charge of an electron q. The diode equation represents the majority carrier current, while the minority carrier current is related to intensity of the absorbed light.

$$I = I_{ph} - I_o \left[\exp\left(-\frac{q\,V}{KT}\right) - 1\right] \tag{23}$$

Under illumination, the oxidation current is generated when holes cross the semiconductor/liquid interface, so the sign of minority carrier is opposite to the sign of the majority carrier. In the reduction current, the electrons cross the interface (Figure 2.19).

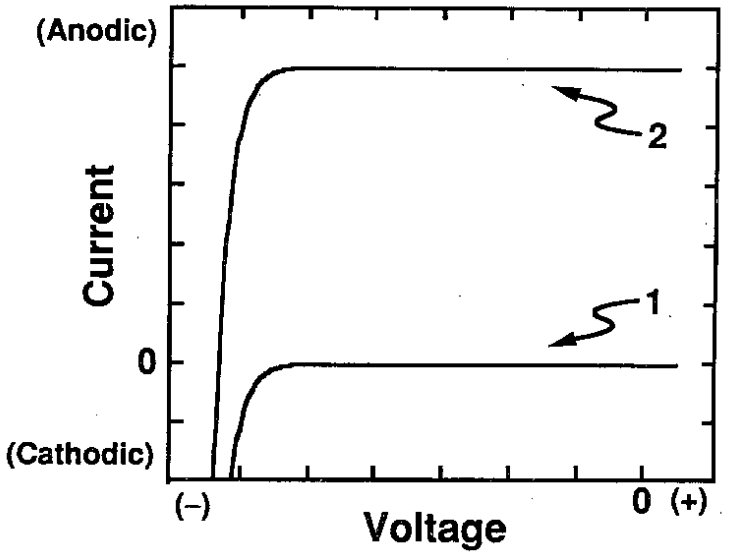

Figure 2.19 The current –voltage curves of a semiconductor/liquid junction, (1) in the dark and (2) under illumination. [8]

B- Energy conversion properties: -

As mentioned before, there are essential parameters that are related to energy conversion applications: the open circuit voltage (V_{oc}), the short circuit current (I_{sc}), and the fill factor (*FF*).

First parameter is the V_{oc}. This parameter can represent the maximum free energy that can be extracted from an illuminated semiconductor/liquid interface. In general case, $I_{ph} > I_o$ so the '' 1'' in eq. 61 can be neglected

$$I = I_{ph} - I_o \left[\exp\left(-\frac{q\,V}{KT}\right)\right] \tag{24}$$

As known, the net current *I* is zero at open circuit voltage. So the open circuit voltage is defined as $V_{oc} = |V|$ at *I = 0*, and V_{oc} is given by

$$V_{oc} = \frac{KT}{q}\, ln\left(\frac{I_{ph}}{I_o}\right) \tag{25}$$

The open circuit volatge increases with increasing the intensity of light logarithmically due to linear relationship between I_{ph} and the flux of the absorbed photons. In addition,

the V_{oc} of a system increases as I_o decreases logarithmically. Small value of I_o implyies a slower rate of interfacial equilibrium, so large photovoltage could be obtained easily. Equation 25 confirmed that the I_o controlles the value of V_{oc} in this junction.

The second parameter that is esstinal for energy conversion application is the short circuit current density (J_{sc}). The short circuit current occurs at V=0. From equation 23, The short circuit current density is equal to I_{ph}/A, where A is the area of electrode. The J_{sc} can be used to measure the efficieny of the photogenerated carrier collection process in a photochemical cell.

There are several factors that affect the value of the short circuit current density. When light enters, it has three choises. First, it may be absorbed by solution. Second, it may be reflected at different interfaces of the cell. Third, it may be absorbed by the semiconductor and then converted to photocurrent. There are two quantums that used for measureing the efficiency of the photocurrent collection in junction : the internal quantum yield and the external quantum yield. The internal quantum yield is responsible for measuring the collected charges based on the number of absorbed photons by semiconductor. It is equal to J_{sc}/q divided by the flux of absorbed photons by the semiconductor. Recombination losses of minority carriers can be neglected at short circuit for many semiconudtor/liquid junctions. Consequently, the internal quantum yield approaches unity for photons of energy grater than E_g.

The external quantum yield is J_{sc}/q divided by the flux of incident photons onto the cell. Because of the optical transmission losses and reflection losses, the number of the absorbed photons by semiconductor is a portion of the total number of the incident photons. Consequently, the internal quantum yield is greater than the extrnal quantum yield. The internal quantum yield depends on the internsic properties of the semiconductor/liquid junction. The external quantum yield depends on the design of the photochemical cell. Both types of quantum yield are very important and sometimes called quantum efficiencies.

To connect between a quantum yield and an energy conversion efficiency, the stored energy must be included into the calculation. A photochemical cell at open circuit (V = 0) or short ciruit (I = 0) does not produce power, beccause the power (P) equals IV. The maximum energy conversion efficiency of semiconductor/liquid junction can be expressed as follows:

$$\text{Efficiency \%} = \frac{(IV)_{max}}{P_{in}} \times 100 \qquad (26)$$

where P_{in} is the incident solar power on the semiconductor electrode.

The third parameter that is essential for energy conversion application is the fill factor (*ff*). It can be expreesed by the ratio of (IV)$_{max}$ divided by $I_{sc}V_{oc}$. The fill factor quantifies how the power curve fills the maximum possible rectangle for a semiconductor/liquid interface. A nother expression for the cell efficency is given by

$$\text{Efficiency } \% = \frac{(I_{sc}\, V_{oc})\, ff}{P_{in}} \times 100 \qquad (27)$$

From eq. 27, the energy conversion efficienicies depend on the three essential parameters: V_{oc}, I_{sc} , and *ff*. The short circuit current density can be increased by decreasing the loss in recombination of the absorbed carriers.

2.4 Benefits of using Silicon Nanowires for Solar Cell Applications

There are essential steps as mentioned above for converting light to electricity including absorbing photon, creating exciton, separating exciton to free carrier and collecting free carrier by the electrode. Nanowires can be used for reducing the loss in the above processes. The main advantage of using nanowires is minimizing the cost of solar cell by decreasing the purity of the semiconductor material. The basic benefit of nanowires associated with each photoconversion steps are shown in Figure 2.20.

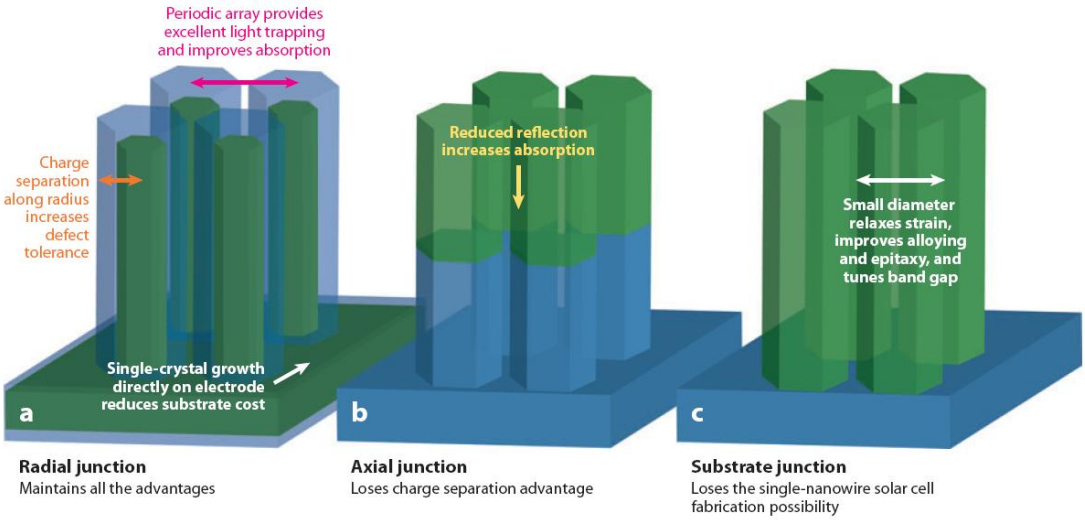

Figure 2.20 Advantage of the nanowire geometry for solar cell (a) Radial junction of periodic arrays of nanowires preserve all pros such as increasing absorption, light-trapping, and separation of charge, (b) lose in the radial charge separation benefit, and (c) Substrate junctions [12]

2.4.1 Absorption:

The loss in absorption is divided into two sections: reflection and transmission. Antireflection coating and light-trapping schemes have been used to minimize the two losses.

Reflection comes from the difference between two refractive indices of two media at an interface. [13] When there is no antireflection coating, semiconductor reflects between 10-50 % of the incident light of wavelength range 400-2000 nm. The reflection loss in Si solar cell that is without antireflection coating is more than 30%. [14] For overcoming this loss, one or two layers of antireflection coating can be added. These layers have an

intermediate refractive index n between two media. [15] This coating layer causes destructive interference between incident and reflected light, and removes reflection at two interfaces. This way is available for a single wavelength at normal incidence.

Although most reports study the antireflection properties of nanowires, but these reports neglect studying the effect of light-trapping schemes on decreasing the loss in optical absorption. Light-trapping schemes have been investigated in the market for thin film solar cell. [13,16] Yablonovitch et al. used geometrical optics and statistical mechanics approaches to study light-trapping schemes. They found that both approaches could demonstrate the enhancement of the intensity of light within the medium of $2n^2$ compared with the incident light. This matches with a path length of $4n^2$. The assumption here is that the light was not absorbed by the medium and it enters randomly the structure. Consequently, random arrays of nanowires may still have $4n^2$ limit, but periodic arrays exceed it. These random arrays work as centers for strong scattering, which have optical mean free path. [17] The optical mean free path is the length in which light travels in the array between scattering events of nanowires. This length decreases with the increase of the energy of photon. There is also another effect called resonance effect that depends strongly on the diameter of the nanowires. Cao et al [18-21] studied the leaky-mode resonance in detail by measuring the photocurrent and spectrum of scattering of single nanowire. They studied the effect of increasing diameter on resonance and found that there is a redshift in the efficiency peaks of scattering and absorption with the increase in the diameter and correspond to scattering calculations of Lorentz-Mie and finite difference time domain simulations. Moreover, a single nanowire offers an enhanced optical cross section over the geometrical cross section to improve the absorption with less material. In addition, periodic arrays can also profit from collective resonance, diffraction effect and changes in the optical density of states. These periodic structures may not be leaped by the randomized scattering limit.

Garnett & Yang [22] measured the light-trapping by utilizing arrays with the various lengths and found that the path length enhancement factor increases with increasing the length of nanowire (Figure 2.21). The path length enhancement factor is the division of the optical thickness of structure by its real thickness. The roughness factor in Figure 2.21 is the ratio between the surface area of the nanowire array and the planer control. The increase of the path length enhancement is proportional to the roughness because the increase of the length decreases the available amount of silicon for absorption. The best array of nanowire presented path length enhancement factors of up to 73 that exceed the randomized scattering limit ($2n^2 \sim 25$ due to absence of back reflector). The efficiency of optical absorption depends on the length of nanowire array because this dependence comes from very poor coupling to photonic crystal and waveguiding modes for short nanowires.

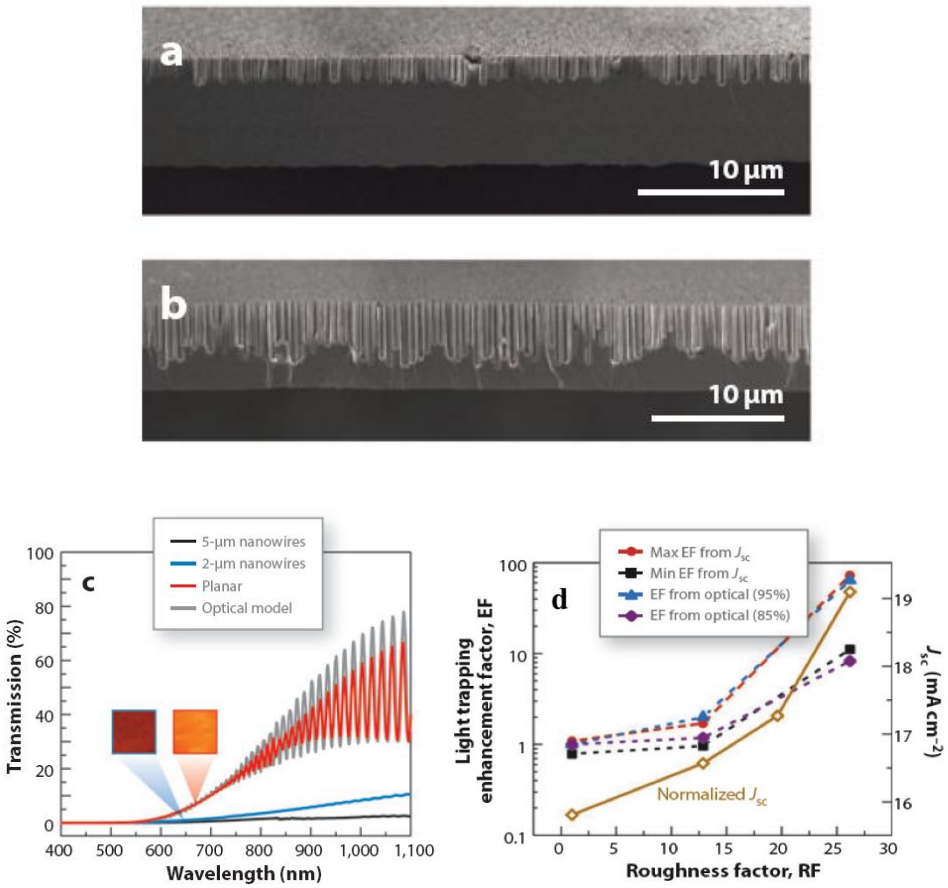

Figure 2.21 Measurements of optical transmission, of thin silicon window with and without nanowires, light trapping effect as function of roughness factor (RF) (a) nanowire arrays with length 2 µm, (b) nanowire arrays with length 5 µm, (c) Optical transmission of thin silicon window before etching (red) and after etching to form 5 µm (black) and 2 µm (blue) nanowire arrays and optical model of thickness 7.5 µm (gray) and (d) Light-trapping path length enhancement factor via RF and the current density *Jsc* for ordered SiNWs with the same RF but different absorber thicknesses (red and black) and from the optical transmission measurements in panel.[22]

Finally, nanowires show decrease in the loss of optical absorption due to higher surface area compared with planer sample (Figure 2.22). Peters et al. [23] studied theoretically the absorption of nanowire with length 7µm and diameter 50 nm. They found that the absorption can reach 84% by nanowires of the above band gap radiation when dyes are added, while the nanowire without dye can absorb only 56%. All these calculations neglect the effect of the light-trapping. Using nanowire with optical resonance due to increase of electric field at the surface can increase the transfer of energy.

Utilizing nanowire with optical resonances located at dye absorption peak may enlarge the transfer of energy due to increase of electric field at the surface.

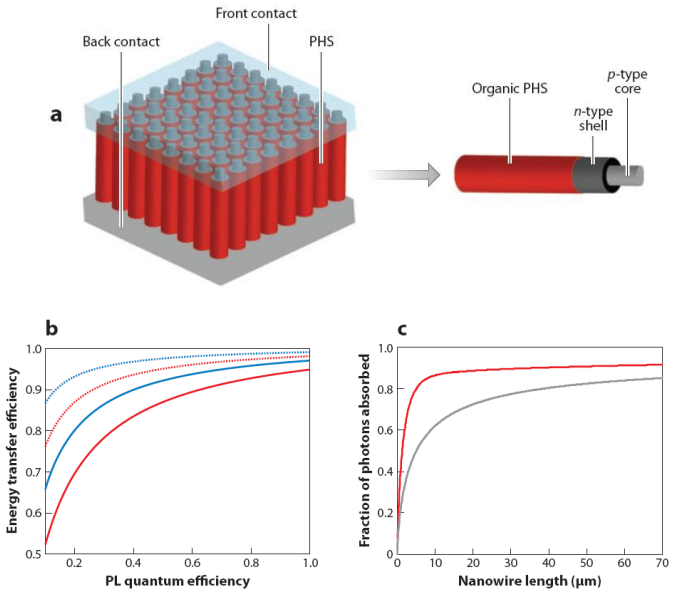

Figure 2.22 "The effect of using photon harvesting shells (PHS) on increasing the absorption in nanowires through resonant energy transfer. (a) Schematic of a nanowire solar cell with a PHS, (b) the relationship between energy transfer efficiency (ETE) and dye photoluminescence (PL) efficiency for dye A (blue) and dye B (red). The solid lines are for x values of 2,7 nm and dashed lines are for x values of 1.7 nm, where x is the dye separation distance from the surface of nanowire, and (c) Fractions of photons above the band gap of silicon that are absorbed with bare silicon nanowires (gray) and with dyes A and B attached to the nanowires (red) as a function of nanowire length." [23]

2.4.2 Exciton Formation

The next loss after absorbing light is carrier relaxation. If the binding energy of exciton is weak compared with bulk silicon at room temperature, the excited carrier will dangle to the edge of band as free carrier. If the binding energy of exciton is strong, the carrier can compose a bound exciton state. Coupling of carrier-phonon can occur this carrier relaxation, so the energy is lost in the form of heat. This loss acts between 30-40 % of the incident solar energy in every photovoltaic. [24] For decreasing this loss, material with an optimal band gap or different materials with optimal complementary band gap can be used. The common method used for adapting material band gaps is alloying different materials together. Nanowires solve the miscibility of gaps by improving the strain relaxation due to broadening the range of absorption energies. [25] Moreover, the increase of band gap can also obtained by reducing the diameter of the nanowires to be near the Bohr radius of the material. [26] This method is useful for some materials such as germanium that have large Bohr radii and small band gap. Another method for reducing the heat loss is introducing nonlinear carrier generation schemes such as multiple exciton generation (MEG). [24] This method decreases the coupling of carrier-phonon, relaxes the conversion of momentum and supports Auger processes in quantum-confined systems.

2.4.3 Charge Separation:

Wu et al. [26] studied the charge separation of nanowires by using density functional theory. They found that the nanowires, which have various degrees of quantum confinement, can separate holes and electrons without any dopant. The same author presented in another work that charge separation could also be obtained by changing strain along the nanowire length leading to changing in band gap. [27] This mechanism facilitates fabrication of solar cell from undoped materials with extremely low rate of Auger recombination, which is the mean factor in limiting the efficiency of solar cell. [14,16,28]

2.4.4 Carrier Collection:

After separation of carriers, they must diffuse to the contact. The geometry of nanowire is very useful for this step because it enables rapid radial charge separation and efficient carrier collection during band conduction. [29] Kayes et al. [29] showed that radial p-n junction of Si nano-or microwires shows very low efficiency degradation with reducing lifetime until the diffusion length of minority carriers approaches to the radius of nanowire. However, planer p-n junction cell shows several degradations once the diffusion length is lower than the thickness of thin film. Figure 2.23 presents this effect strongly where there is high incoherence between the diffusion length of minority carrier and the absorption, which is commonly happening in indirect band gap semiconductor such as silicon. When the defects are concentrated in the region of quasi-neutral of the device (the upper surface in the Figure 2.12), the radial junction shows a high efficiency. While large defect densities in the depletion region decrease the performance of radial and planer junctions (the lower surfaces in Figure 2.23).

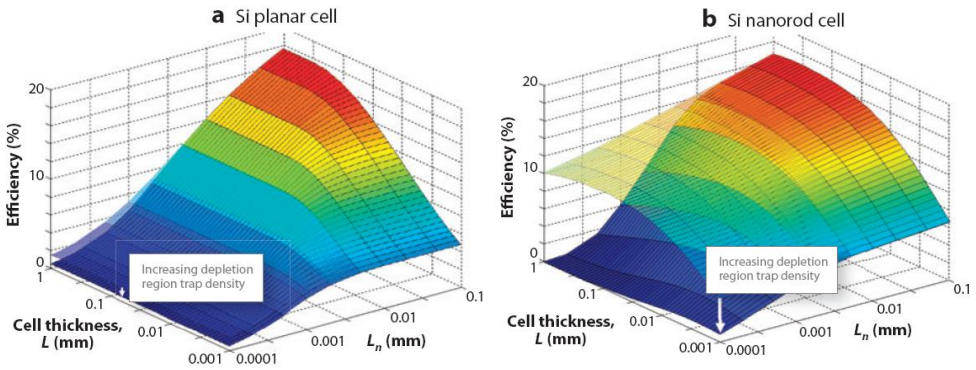

Figure 2.23 the relationship between efficiency and thickness of cell L and the diffusion length of minority electron L_n for (a) planer p-n junction silicon cell, and (b) a radial p-n junction nanorods silicon cell. [29]

References

[1] Lewis, Nathan S., and Daniel G. Nocera. "Powering the planet: Chemical challenges in solar energy utilization." Proceedings of the National Academy of Sciences 103.43 (2006): 15729-15735.
[2] Sze, Simon M., and Kwok K. Ng. Physics of semiconductor devices. John Wiley & Sons, 2006.
[3] Sze, Simon Min. Semiconductor devices: physics and technology. John Wiley & Sons, 2008.
[4] Green, Martin A. "Solar cells: operating principles, technology, and system applications." Englewood Cliffs, NJ, Prentice-Hall, Inc., 1982. 288 p. 1 (1982).
[5] Neamen, Donald A., and Boris Pevzner. Semiconductor physics and devices: basic principles. Vol. 3. New York: McGraw-Hill, 2003.
[6] Ferry, David K., and Jonathan P. Bird. Electronic materials and devices. Academic Press, 2001.
[7] Soga, Tetsuo, ed. Nanostructured materials for solar energy conversion. Elsevier, 2006.
[8] Tan, Ming X., et al. "Principles and applications of semiconductor photoelectrochemistry." Progress in Inorganic Chemistry, Volume 41 (1994): 21-144.
[10] Tufts, Bruce J., et al. "Chemical modification of n-GaAs electrodes with Os3+ gives a 15% efficient solar cell." (1987): 861-863.
[11] Licht, Stuart, and Dharmasena Peramunage. "Efficient photoelectrochemical solar cells from electrolyte modification." (1990): 330-333.
[12] Garnett, Erik C., et al. "Nanowire solar cells." Annual Review of Materials Research 41 (2011): 269-295.
[13] Hecht E. 2002. Optics. San Francisco: Pearson. 698 pp.
[14] Green, Martin A. "Solar cells: operating principles, technology, and system applications." Englewood Cliffs, NJ, Prentice-Hall, Inc., 1982. 288 p. 1 (1982).
[15] Zhao, Jianhua, and Martin A. Green. "Optimized antireflection coatings for high-efficiency silicon solar cells." Electron Devices, IEEE Transactions on 38.8 (1991): 1925-1934.
[16] Green, Martin A. "Silicon solar cells." Sort 20.130 (1995): 701-00.
[17] Muskens, Otto L., et al. "Large photonic strength of highly tunable resonant nanowire materials." Nano letters 9.3 (2009): 930-934.
[18] Cao, Linyou, et al. "Resonant germanium nanoantenna photodetectors." Nano letters 10.4 (2010): 1229-1233.
[19] Cao, Linyou, et al. "Engineering light absorption in semiconductor nanowire devices." Nature materials 8.8 (2009): 643-647.
[20] Cao, Linyou, et al. "Semiconductor nanowire optical antenna solar absorbers." Nano letters 10.2 (2010): 439-445.
[21] Cao, Linyou, et al. "Tuning the color of silicon nanostructures." Nano letters 10.7 (2010): 2649-2654.
[22] Garnett, Erik, and Peidong Yang. "Light trapping in silicon nanowire solar cells." Nano letters 10.3 (2010): 1082-1087.
[23] Peters, C. H., et al. "Energy transfer in nanowire solar cells with photon-harvesting shells." Journal of Applied Physics 105.12 (2009): 124509.

[24] Colombo, C., et al. "Gallium arsenide pin radial structures for photovoltaic applications." Applied Physics Letters 94.17 (2009): 173108-173108.
[25] Briseno, Alejandro L., et al. "Oligo-and polythiophene/ZnO hybrid nanowire solar cells." Nano letters 10.1 (2009): 334-340.
[26] Greene, Lori E., et al. "ZnO-TiO2 core-shell nanorod/P3HT solar cells." The Journal of Physical Chemistry C 111.50 (2007): 18451-18456.
[27] Wu, Zhigang, J. B. Neaton, and Jeffrey C. Grossman. "Charge separation via strain in silicon nanowires." Nano letters 9.6 (2009): 2418-2422.
[28] Tiedje, Tom, et al. "Limiting efficiency of silicon solar cells." Electron Devices, IEEE Transactions on 31.5 (1984): 711-716.
[29] Kayes, Brendan M., Harry A. Atwater, and Nathan S. Lewis. "Comparison of the device physics principles of planar and radial pn junction nanorod solar cells." Journal of applied physics 97.11 (2005): 114302.

Chapter 3

Silicon nanowires for solar cells applications

3.1Introduction

Great efforts from the last decades have been done to improve different types of PV devices. [1-3] As the manufacturing cost of photovoltaic materials has decreased to a level where electricity that comes by solar energy becomes competitive with other types of energy. Solar cells that depend on crystalline silicon have been used since 50 years ago due to different properties of silicon (Si). Firstly, Si is the second abundant material on the earth. Secondly, it is nontoxic material that made it used in pure form with high mobility of electrons and holes. Thirdly, Si can be doped with different types of impurities to increase the concentration of holes (p-type) or electrons (n-type). The doping process decreases the resistance of the contacts of devices. Finally, single junction Si solar cell has high efficiency because of low carrier recombination rates. The band gap of Si is 1.1 eV that matches with the visible light spectrum. However, it is not economically to use large-scale applications because of the high cost of silicon wafer, which acquires high purity of Si to get high performance. [4, 5] Therefore, decreasing the quantity and quality of silicon will help in using large scale of silicon photovoltaics. There are extensive efforts to decrease the cost of thin film solar cell, [6-8] such as copper indium gallium selenide (CIGS), cadmium telluride (CdTe), polycrystalline Si, and amorphous Si (a-Si) PVs.The optical absorption can be improved by reducing light scattering and trapping. [9] For decreasing the cost, the design of PV depends on nanostructured materials such as nanoparticles, [17-19] quantum dots, [10-12] nanorods, [13-16] nanotubes, [20,21] and nanowires [22-24] due to their large surface areas. Semiconductor nanowires with one dimension (1D) are a promising candidate because they have direct paths for charge transport.

In particular, Si nanostructures such as Si nanowires (SiNWs) show interesting properties [25-28] including high density electronic states, enhanced excitation binding energies, enhanced thermoelectric properties, high surface scattering for phonons and electrons and high surface- to- volume ratio. [29] All aforementioned properties provide high potential for different applications such as energy harvesting, electronic and photonic devices, chemical and biological sensors, [30-32] thermoelectric systems, [33] and solar cells.[34] For solar cell applications, SiNWs have been studied for reduced reflection [35] and increased absorption.[36, 37] For example, the effective path length was increased by a factor of 73 for the absorption of light as compared to bulk silicon. [37] This increase of the path length contributes to the effective trapping of light within the nanowires.

3.2. Fabrication methods of Si nanowires:

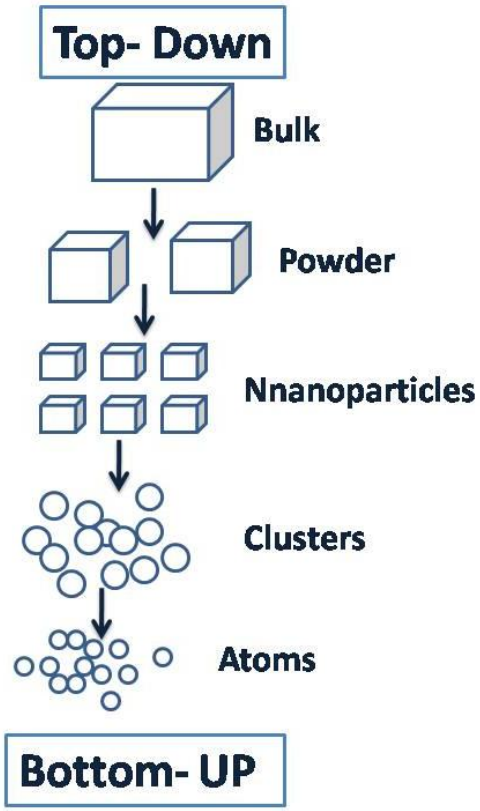

Figure 3.1Schematic shows the difference between bottom-up and top-down approaches

There are different methods for fabrication of nanostructured materials, but this chapter will focus on different methods for synthesizing SiNWs. Synthesis of SiNWs with controlled orientation, length and diameter is important for different applications such as field-effect transistors and devices for energy conversion. There are two basic approaches for fabrication process: the bottom-up and top-down. The first approach depends on building up the atoms of Si to form SiNWs. This method includes oxide-assisted growth (OAG), [38] vapor-liquid solid (VLS) growth, [39-41] solution based and supercritical-fluid based growth. [42-44] Secondly, the top-down approach that grows SiNWs by reducing dimensions of bulk material. This approach includes reaction ion etching (RIE), electron beam lithography, and metal assisted chemical etching (MACE).

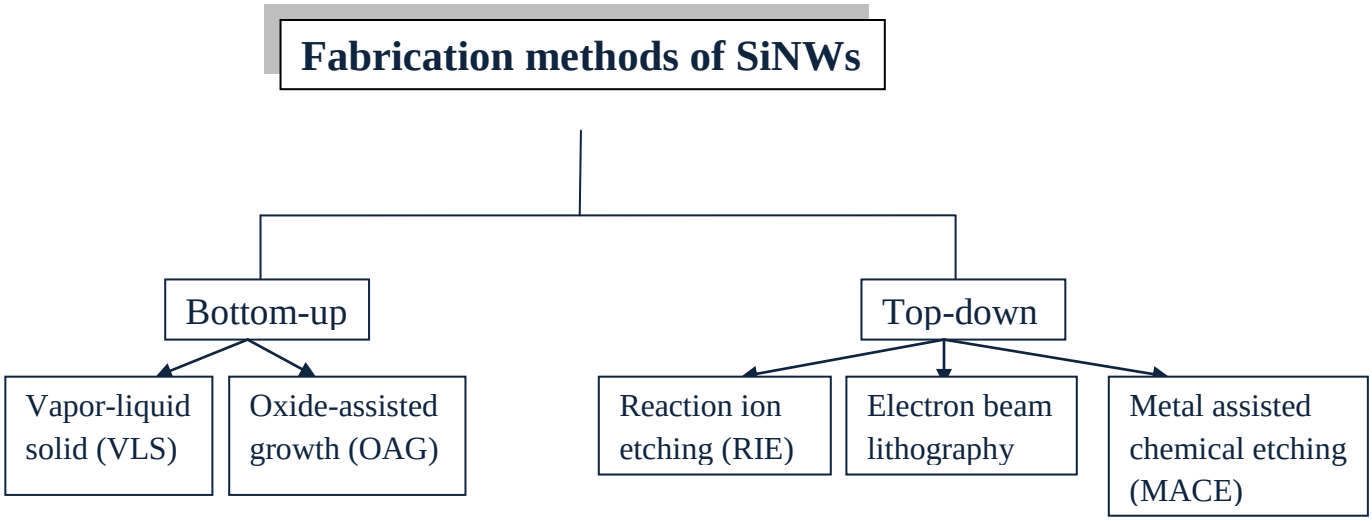

Figure 3.2 Schematic represents summery of different fabrication method of SiNWs

All pervious methods have the same aim that is controlling the different parameters of the SiNWs. The most attractive method is MACE for different reasons. First, it is simple where all steps can be done without expensive equipment. The SiNWs with controlled cross-sectional, length, diameter, doping type, orientation and shape can be fabricated with low cost. Second, VLS method can be grown only wires with circular cross-section. MACE is more flexible than VLS and gives high surface – to volume ratio. [45, 46] Third, MACE controls the orientation of SiNWs without depending on the diameter of nanowires not as VLS method. [47] For example, the growth of vertical or epitaxial of SiNWs on (100) or (110) substrates has not been achieved without utilizing template. Moreover, electrochemical etching takes place anisotropically along < 100 > directions. In contrast, MACE can fabricate vertical aligned SiNWs and controls the etching direction. [48, 49] Fourth, there is no limitation on the fabricated size of nanowires by MACE. This method can be used to fabricate well aligned SiNWs with diameters in range 5 nm to 1 µm. Fifth, by using MACE for fabrication, the quality of crystallinity of obtained SiNWs from single crystal substrate is high. In addition, the roughness of surface is very high that increases the absorption in solar cell application. Sixth, the deposition of metal catalyst in MACE process is at room temperature; as a result, the obtained SiNWs do not have any contamination that comes from metal diffusion at high temperature.

3.3 Backgrounds and Mechanism of MACE Process:

The first use of MACE of silicon was reported in 1997, when it was used as electroless etching technique for producing porous Si by Li et. al.[50] They studied the effect of depositing a thin layer of noble metal on the substrate. They found that adding this layer helps in fasting the etching rate of Si.

In MACE, a noble metal covers partly the substrate of Si. The substrate is immersed in etchant that contains from HF and an oxidant agent (e.g., Mg $(NO_3)_2$, H_2O_2, Fe $(NO_3)_3$, $KMNO_4$). MACE uses noble metal to make oxidation and reduction reactions without any closed circuit. When metal is deposited on the surface of the substrate, it works as a cathode to produce holes (h^+). The holes are injected into the valence band of the semiconductor for oxidization. The ionic form is formed that can be soluble in acidic solution; as a result, the semiconductor material removed without any consuming of the metal.

3.3.1 Reactions

The overall reaction of MACE of Si substrate is presented in this section.

For cathode reaction: H_2O_2 is reduced at the metal

$$H_2O_2 + 2H^+ \rightarrow 2H_2O + 2h^+ \quad (1)$$

Li et al. suggested there is another reaction in cathode that comes from reduction of protons into hydrogen:

$$2H^+ \rightarrow H_2 \uparrow + 2h^+ \quad (2)$$

On the contrary, the basic of reaction agent of Chartier et al. [51] at cathodic sites was H_2O_2 instead of H^+; as a result, there is no possibility of existing gas from a decay of H_2O_2 because there is no gas evolution on Ag-particles in solution with high concentration of H_2O_2 in the absence of HF.

At the anode, the oxidization and dissolution processes occur on Si substrate. There are three groups for discussing the direct dissolution process of Si. First one occurs in a tetravalent state [50, 52]

$$Si + 4h^+ + 4HF \rightarrow SiF_4 + 4H^+ \quad (3)$$
$$SiF_4 + 2HF \rightarrow H_2SiF_6 \quad (4)$$

Second (RII) occurs in divalent state [52]

$$Si + 4HF^-_2 \rightarrow SiF_6^{2-} + 2HF + H_2 \uparrow + 2e^- \quad (5)$$

(RIII) Si oxide formation followed by dissolution of oxide [53]

$$Si + 2H_2O \rightarrow SiO_2 + 4H^+ + 4e^- \quad (6)$$
$$SiO_2 + 6HF \rightarrow H_2SiF_6 + 2H_2O \quad (7)$$

The difference between the last two models is in the formation of Si oxide, where it is formed at the surface of substrate before occurring the dissolution process. The H_2 is generated through the dissolution process. Because of the generation of hydrogen in etching, the model RII has been occurred. Then Chartier et al. suggested another mixed reaction that is between the two states (divalent and tetravalent) dissolution for MACE: [53]

$$Si + 6HF + nh^+ \rightarrow H_2SiF_6 + nH^+ \frac{4-n}{2} \quad H_2 \uparrow \quad (8)$$

The overall reaction is:

$$Si + \frac{n}{2}H_2O_2 + 6HF \rightarrow nH_2O + H_2SiF_6 + \frac{4-n}{2} H_2 \uparrow \quad (9)$$

3.3.2 The overall of etching process

Figure 3.3 shows the process of MACE and it can be described in the following steps: (1) the oxidant at the surface of the noble metal is decreased because of the activity of catalyst of the noble metal. (2) Because of the diffusion of the oxidant, the holes are generated and injected into Si substrate that is in contact with the noble metal. (3) The injected holes oxidized the Si and then HF dissolves the Si at the Si/metal interface that the diffusion process of the reactant (HF) occurs in. (4) At the Si/metal interface, the concentration of holes reaches its maximum. Therefore, the etching occurs for the Si that is in contact with metal by HF. (5) The diffusion process of holes occurs from the Si that is covered by metal to free metal areas or to the well of the pore when the consuming rate of holes is smaller than the injection rate at the Si/metal interface. As a result, the etching process may occur at the free metal areas or sidewalls of the pore to form microporous silicon.

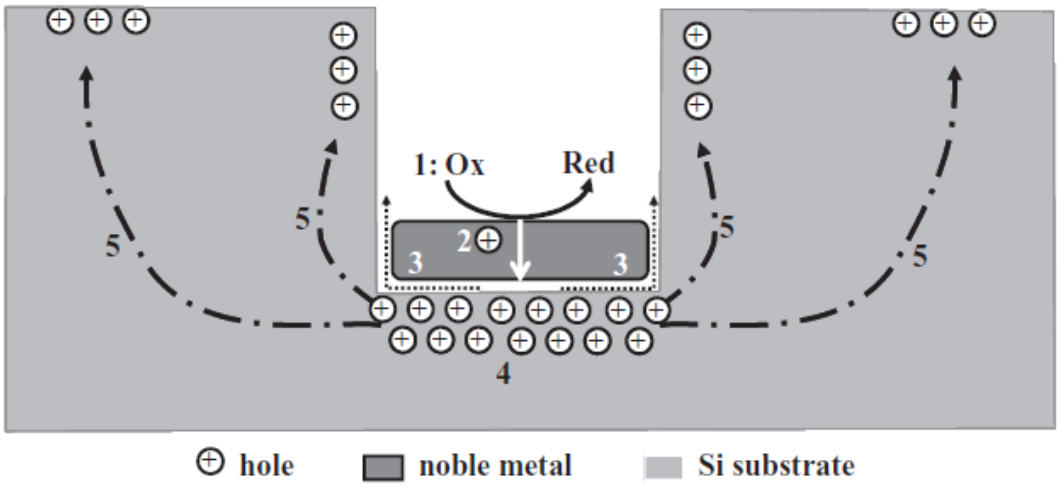

Figure 3.3 Schematic represents the steps of the process of metal assisted chemical etching method [53]

3.4 Effect of different types of noble metals on the etching:

Noble metals affect strongly the morphologies of the etched structures. For producing straight pores, isolated particles are used such as Ag or Au in etching process (Figure 3.4a, b). [54, 55] In contrast the behavior of Pt particles. When Pt particles are used to assist in the etching process, the straight or helical pores are formed as reported by Tsujino et al. (Figure 3.4 c). [54, 56] On the contrary, Pt particles move randomly when they are deposited by sputtering [57] or electroless plating [58] and produce curvy pores without a uniform etching direction (Figure 3.4 d), although the etching rate by using Pt is faster than that used Au. [50] In addition, the resulting wires by using Pt were surrounded by a porous layer, [54,55] but in the case of using Ag or Au in etching, there is no observable a porous layer.

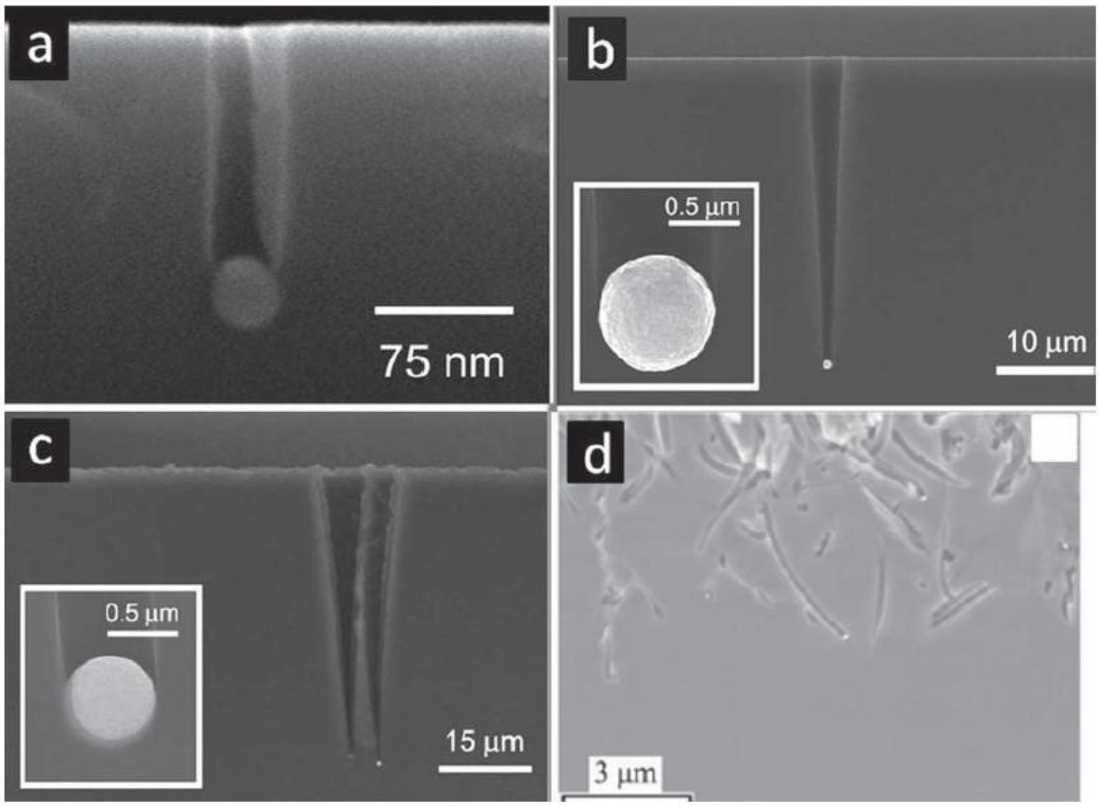

Figure 3.4 Different behaviors of metal in etching process (a) Ag- particle, [55] (b) Au- particle, [54] and (c, d) Pt- particle. [58]

3.5 Influence of change temperature of Etchant:

It has been reported that there is a linear relationship between the length of the fabricated SiNWs by MACE and the time of etching process. Cheng et al. investigated the relation

between the length of SiNWs and time of etching at temperature range 0: 50 ^{o}C. The length of the fabricated SiNWs increases with increasing the etching time at all temperatures (Figure 3.5a). The rate of etching increases with increasing temperature of etchant. Cheng et al. obtained the activation energy of the fabricated Si nanowires on a (100) substrate, which is 0.36 eV, from changing the etching rate via the Arrhenius plot as shown in Figure 3.5b. [59]

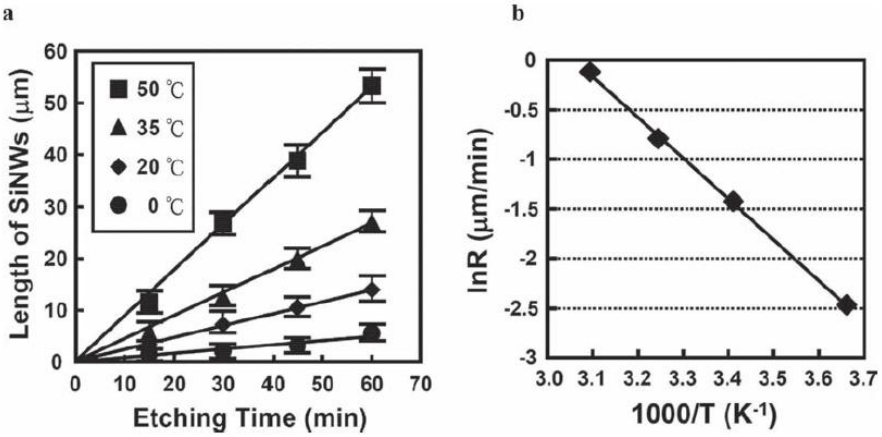

Figure 3.5 (a) The relation between length of SiNWs and time of etching at different temperature, and (b) Arrhenius plot of the formation rate versus reciprocal absolute temperature.[59]

Metal assisted chemical etching of Si substrate with orientation (100) p-type or n- type that has the same resistivity (1-10 Ω cm) have been conducted in two conditions (dark and light). At the same etching time, there is difference in the etching depth between dark and room light. For both substrates, the etching depth during light with a 20W bulb is higher than the etching depth in the dark by 1.5.

3.6 Silicon nanowires for photovoltaic applications

Nanowires are used for solar cell applications because they reduce the optical loss of absorption and improves both carrier extraction and design with low cost. Although porous silicon is better than any surface-textured microstructures in reducing the reflectivity as much as less <4% in visible light range, micropillars or SiNWs can reduce the reflectivity further by controlling different parameters such as size, orientation, length, diameter and density. [60] Moreover, by fabricating nanowires with high aspect ratio, the trapping of light occurs that enhances the absorption process. [60-62] This is important for Si where it has indirect bandgap that requires very small dimensions of material to enhance the absorption in solar cells. Thinner structures are also wanted for carrier extraction, specifically for low pure materials. The high aspect ratio SiNWs also has another advantage for p-n junction that is decreasing the path of the minority carrier collection. [60, 63]

Fabrication of the SiNWs by metal assisted chemical etching does not need any infrastructure for crystal growth before growth of wires that reduce the cost of fabrication of solar cell. High quality of Si nanowires with controlled density, diameter, length and orientation can be obtained easily on single or polycrystalline Si substrate by using Ag or Pt as catalyst, which are more effective more than using alkaline. [64]

3.6.1 Optical properties of Silicon nanowires:

3.6.1.1 Enhanced optical absorption and light trapping in silicon nanowires:

The nanowires that are fabricated by MACE method show excellent antireflection properties as reported by Peng et al. [53, 58] Where SiNWs have been fabricated on single or poly crystalline Si substrate. They immersed the substrate in aqueous solution of HF and $AgNO_3$for 20 min at 50 ^oC. They obtained SiNWs with length ~ 10 μm. They used p-type wafer and nanowires are converted to n-type by MACE thermal diffusion so they produced p-n junction in this case and SiNWs works as antireflection coating as showed in Figure 3.6a.The Si nanowire arrays have a low reflection over a wide range of wavelength. The reflectance of poly crystal SiNWs was less than 2 % and less than 1.4 % of single crystal SiNWs that is lower than reflectance of porous and polished Si surface at wavelength range 300 – 600 nm. The low reflectance of SiNWs comes from several advantages of the geometry of wires: (1) the light trapping of the SiNWs; (2) the high surface area of SiNW arrays with high density that decrease the life time of the minority carrier and diffusion length; (3) the interactions of light scattering between SiNWs, which enhance light trapping to make light travel through long paths. As a result, SiNWs can decrease reflection in solar cells without using any antireflection coating layer.

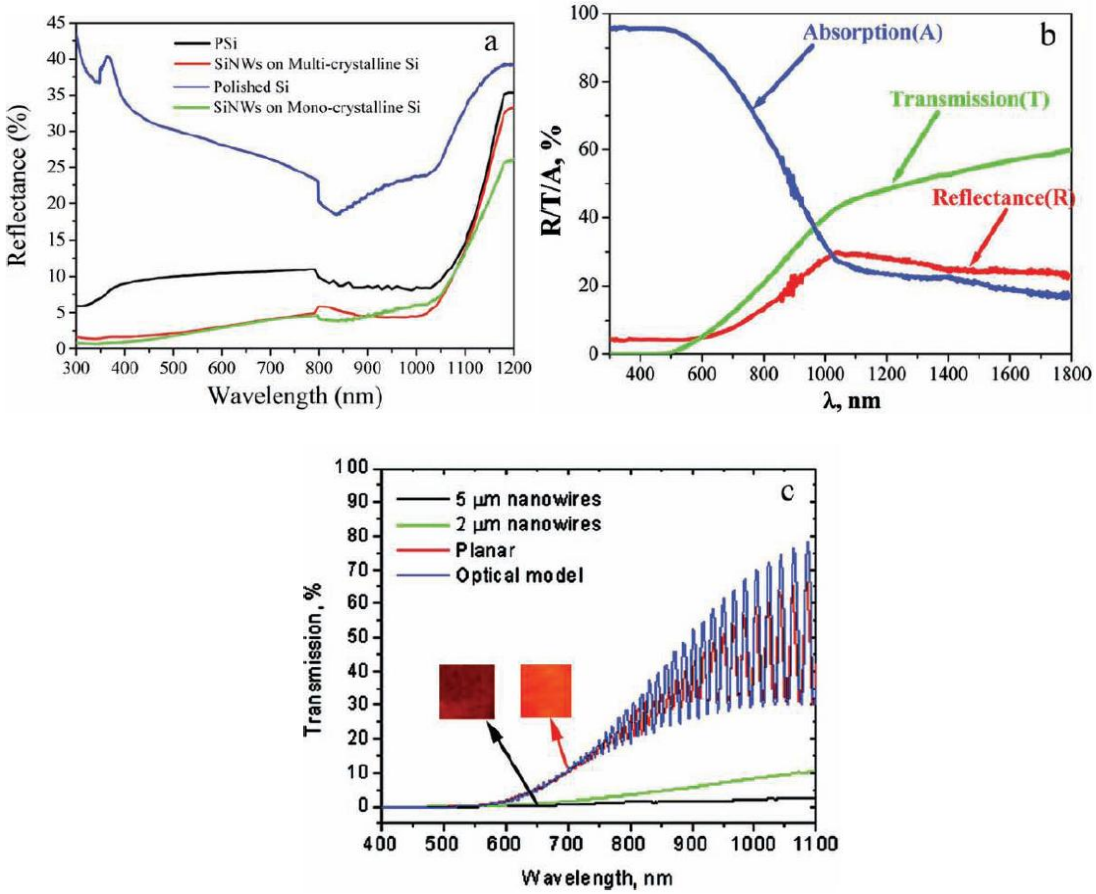

Figure 3.6. a) Reflectance measurements of porous silicon, SiNWs on multi crystalline Si, polished Si, and SiNWs on Mono-crystalline Si. [53] (b) absorption, transmission and reflection of fabricated SiNWs that prepared on glass substrate. [65] (c) transmission of SiNWs of lengths 2, 5 µm, substrate and model of SiNWs. [67]

In addition, the optical properties of SiNWs film fabricated on glass substrate by MACE method have been investigated by Sivakov et al. [65] and Tsakalakos et al.[66]There is also low reflectance at range 300-800 nm of wavelength, strong broadband absorption at 500 nm as shown in Figure 3.6b.The existed strong broadband absorption is related to the strong resonance that is between SiNWs due to the high density of the Si nanowires. Granet and Yang measured the optical transmission and photocurrent (Figure 3.6c) in the AM1.5G spectrum to show that the path length of the incident light has been increased by 73 times. [67]

3.6.1.2 Simulation of optical absorption of Si nanowires arrays

SiNW arrays have optical properties that are different from thin films or bulk Si. Recently, different researchers did simulation of SiNW arrays to study the optical properties. [68-71] Hu and Chen used the transfer matrix method (TMM) for doing numerical analysis to study the effect of changing different parameter of Si nanowire such as length, diameter, and filling ratio on the absorption. [69] The simulated Si

nanowire arrays that are under study are shown in Figure 3.7a.The calculations showed that there is an electromagnetic interaction between arrays of SiNW that cannot be neglected. The reflectance of SiNW arrays is much less than the reflectance of Si thin film in the wide range of wavelength as shown in Figure 3.7b because of low density of Si nanowires. Also, SiNWs have higher optical absorption than Si thin films in high-frequency regime due to the low reflectance of SiNWs. In low-frequency regime, SiNWs have lower absorption than Si thin films because of high transmission of the SiNWs. Although, in low-frequency regime, there is shortage in absorption due to the low energy of photons, SiNWs absorbed well due to light trapping phenomena that increases the path length. The effect of changing filling ratio of SiNWs has also studied for both absorption and transmission. The SiNW arrays in the low-frequency regime that have high filling ratios absorb more and have low reflectance, while arrays with low filling ratios have low reflectance in the high-frequency regime that have the same length of Si nanowires.

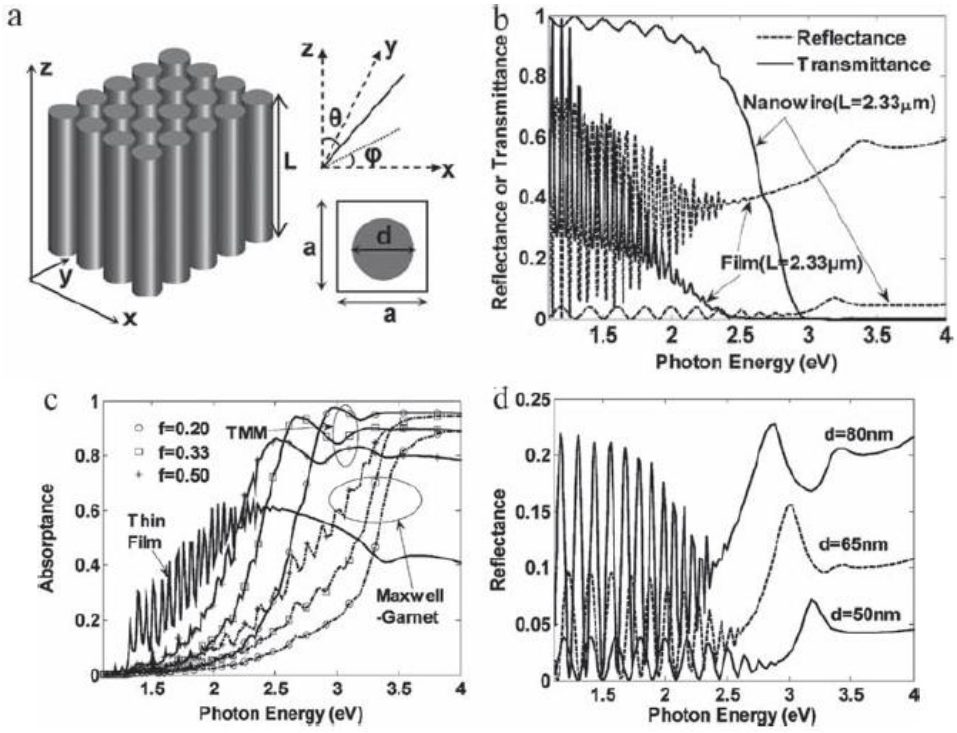

Figure 3.7. a) Schematic of SiNWs array. The parameters are diameter d, length L and the period α and angles are the zenith θ and the azimuthal angle φ. (b) Reflectance and transmittance of thin film and Si nanowires,(c) absorption of SiNWs with different filing ratios obtained by Maxwell Garnet and TMM approximation, and (d) reflection of SiNWs with different diameters. [69]

3.6.2 Radial p-n junction Si nanowire Photovoltaics:

High efforts have been done to produce Si thin film solar cell with low cost by decreasing the quantity of Si. Although the efficiencies of thin-film solar cell with thickness1-2μm were very low (8 – 10 %), scientists are very motivated to improve Si based PVs with

radial p-n junctions. [36, 66, 67, 72, 73] The advantage of radial p-n junction is in the geometry of it. An n-type silicon layer surrounds each Si nanowire of p-type. This type of junction makes travel distance of excited minority carriers short that reduces the recombination and enhances the carrier-collection efficiency. There is another advantage of this junction that is high tolerance of defects of PVs, allowing the use of low purity of Si. The above two advantages are the solution of low cost and high efficiency of p-n junction.

3.6.2.1 Single radial p-n junction Si nanowires for photovoltaic devices:

Tina et al., [72, 74] in 2007, studied the experimental characterization of single p-type/intrinsic/n-type (p-i-n) SiNW solar cells. This type of solar cell consists of a p-type of SiNWs that prepared by VLS method and gold as catalyst. Then p-type nanowires are covered with polycrystalline Si and n-type polycrystalline Si, respectively, by deposition. The fabrication process and the SEM of the p-i-n coaxial Si nanowire solar cell is shown in Figure 3.8 a, b. The maximum obtained power was 200 pW per nanowire deceive when power measured under air mass 1.5 global (AM 1.5 global). The efficiency was 3.4 % and short circuit current density (J_{sc}) was 23.9 mA cm^{-2}. The results showed that the photoexcited carriers along the length of the junction were collected regularly. The scattering that came from metal contacts did not make any contribution in the photocurrent. Moreover, Tian et al. reported that p-i-n junction of SiNWs can be used as a strong power sources for sensors by connecting SiNWs PVs in parallel or in series as shown in Figure 3.8 e, f.

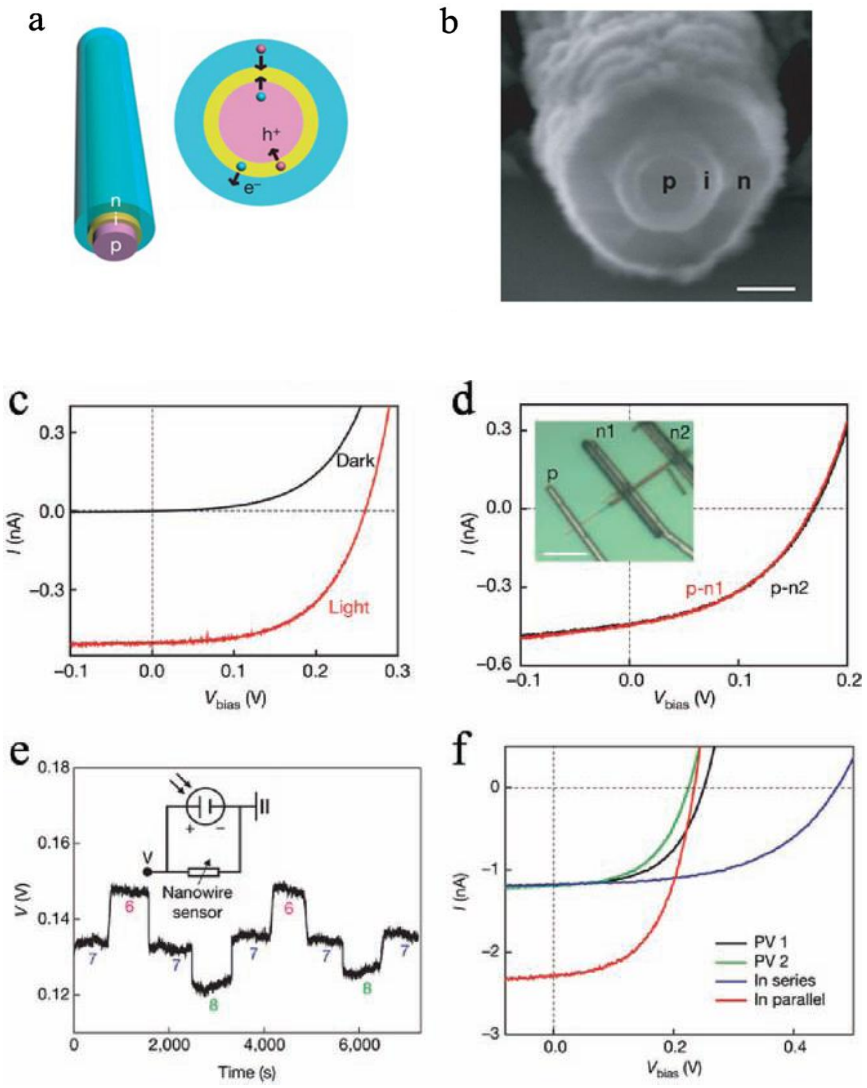

Figure 3.8. "(a),(b) the fabrication process and the SEM of the p-i-n coaxial Si nanowire solar cell, (c) current–voltage curves of fabricated p-i-n junction of SiNWs in dark and under illumination, (d) Light current-voltage curves for two different n-shell contact locations, (e) real time of voltage across SiNWs at different pH values, and (f) light I-V curves of two SiNWs PVs that are connected in parallel and in series." [72]

3.6.2.2 Radial p-n junction SiNW arrays for photovoltaic devices:

P-n junction that forms from SiNW arrays has various pros for PV applications due to the geometry of SiNWs. [36, 67, 75] First, the geometry of SiNWs has antireflection characteristics that absorb all light with energy higher than the energy of band gap of Si. Second, the p-n junction of SiNW array has efficient carrier separation and low recombination. Third, the low dimensions of SiNW decrease the quantity and quality of Si; as a result, the cost of solar cell decreased. Finally, SiNW arrays over large area can be fabricated by CVD-VLS or MACE methods on different substrates that make solar cell from SiNW very promising.

Garnett and Yang fabricated coaxial p-type a-Si/n- SiNW solar cell by combination of CVD, MACE, and rapid thermal annealing (RTP) crystallization. [36] Figure 3.9 shows the fabricated SiNW solar cell and electrical characterizations. The Si single- crystal n-SiNWs, which fabricated by MACE, have diameters between 50-100 nm. Then, n-SiNWs are coated with a layer of polycrystalline p-Si with thickness 150 nm. After making rapid thermal annealing for 10 s at 1000 ^{o}C, the contact electrodes of two sides are formed by sputtering Ti/Pd onto the p-Si and Ti/Ag onto the n-Si. The efficiencies of fabricated devices are about 0.46 % under AM1.5G illumination. This low efficiency was because of high resistance of polycrystalline shell, low local shunting resistance, and high recombination of the junction. Later, Garnett and Yang developed the SiNW array solar cells [67] by decreasing the roughness of the surface by controlling the diameter and density of fabricated SiNWs by combination of RIE and silica bead assembly. The fabricated SiNWs array are elongated the path of light by a factor of 73, leading to increased the short circuit current Jsc over planar control. The efficiency of such solar cell, , which was 5-6%, is higher than that made by VLS method.

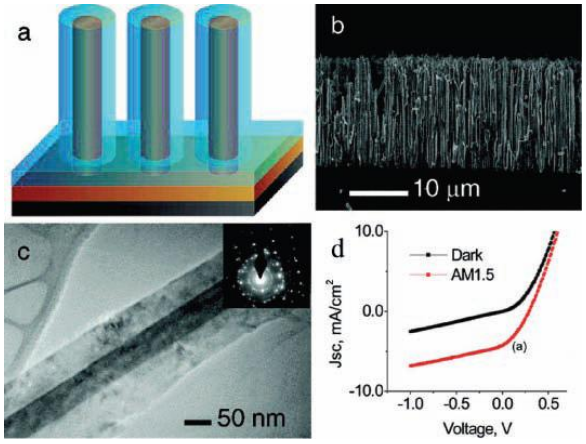

Figure 3.9. "(a) Schematic presents cell design with single crystalline n-SiNW core in brown, the polycrystalline p-Si shell in blue, and the back contact in black, (b) SEM of device showing the vertical SiNWs, (c) Transmission electron microscopy (TEM) demonstrating polycrystalline p-Si shell and the single crystalline n-Si core, and (d) Light and Dark I-V characterization under AM 1.5 G." [36]

3.6.2.3 Improving light trapping by using nanowires and microwires solar cell:

Jung et al. reported a new composition of SiNWs and microwires (SiMWs) that is fabricated by MACE for solar cell applications. [67] Figure 3.10 a and b show the process of fabrication and SEM of fabricated array respectively. The SEM of array after etching process by KOH for 60 s is showed in Figure 3.10 c. For forming high doping and n-type shells, a spin-on-doping technique was used; however the nanowires were converted to n-type because of small diameters as shown in Figure 3.11a. The co-integrated nano and CNMW solar cells have low reflection in the range wavelength 300:1000 nm if it compared with single nanowires or microwires as shown in Figure 3.11b. This type of solar cell has efficiency of 7.19% under illumination AM 1.5G and short circuit current of 20.59 mA.cm^{-2} as shown in Figure 3.11 c.

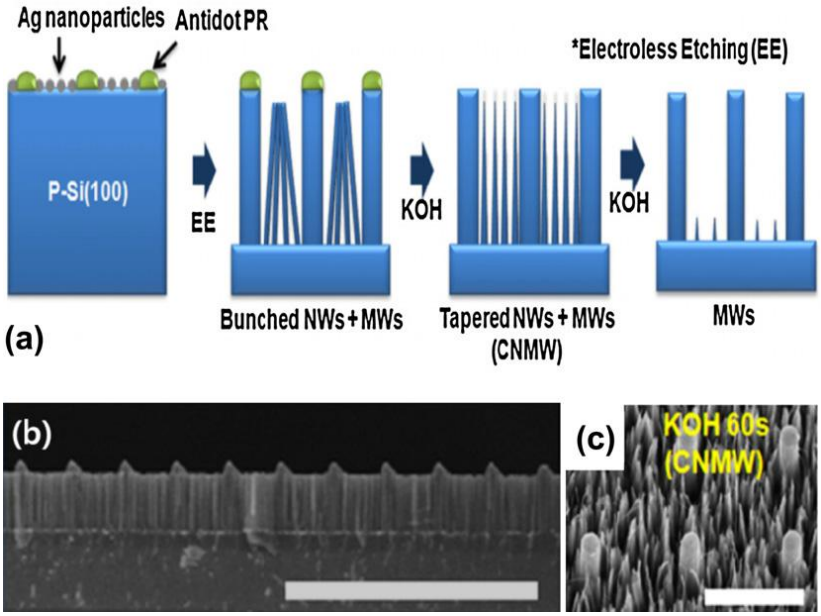

Figure 3.10. (a) Schematic presentation of the steps of fabrication process for the co-integrated wire structure (CNMW) of MWs: (1) deposition of Ag nanoparticles; (2) formation of CNMW by MACE; (3) fabrication of the CNMW structures; (4) result of KOH etching after 240 s, (b) SEM of fabricated CNMW , (c) 30-tilted view SEM of CNMW after KOH etching for 60 s. [77]

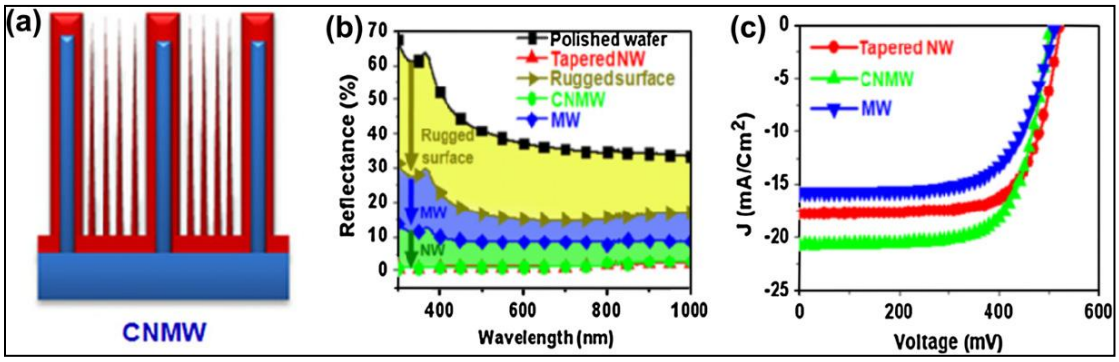

Figure 3.11. (a) Co-integrated wire structure (CNMW) solar cell structure with red (blue) color represents n-type (p-type), (b) Comparison of optical reflection and I–V characteristics of tapered NW (red), CNMW (green), and MW(blue) solar cells. [77]

3.6.3 Silicon Nanowire Photoelectrochemical Solar Cells

Although p-n junction solar cell based on SiNW array are very attractive due to low cost compared with traditional Si-based solar cells, it has low performance due to high loss of recombination and high shunting. The radial liquid-junction nanowires PEC solar cells appeared to be instead of radial p-n junction SiNW solar cells. PEC solar cells become attractive due to low cost and performance. [78-84] For physical principles such as charge – carrier transport and recombination, the photochemical solar cell is the same as radial p-n junction.

3.6.3.1 Photochemical cell of SiMW arrays grown by CVD-VLS

Researchers at Caltech [78] use CVD-VLS technique to deposit Si microwire arrays on highly doped n-Si wafer as shown in Figure 3.12 a. The deposited arrays are from single crystalline n-type that have lengths of tens of micrometers and diameters of a few micrometers. For I-V characterization of the fabricated Si microwires, the PEC cell has been used by using an organic electrolyte that consists of 200 mM of dimethylferrocene (Me_2Fc), 0.5 mM of Me_2FcBF_4 , and 1 M of $LiClO_4$ in methanol. The electrolyte performed as p^+ layer on the surface of SiMWs. The SiMW arrays are photoactive and the resulting photovoltage and photocurrent from PEC cell are higher than the control planar Si samples because of carrier collection in SiMWs (Figure 3.12 b).

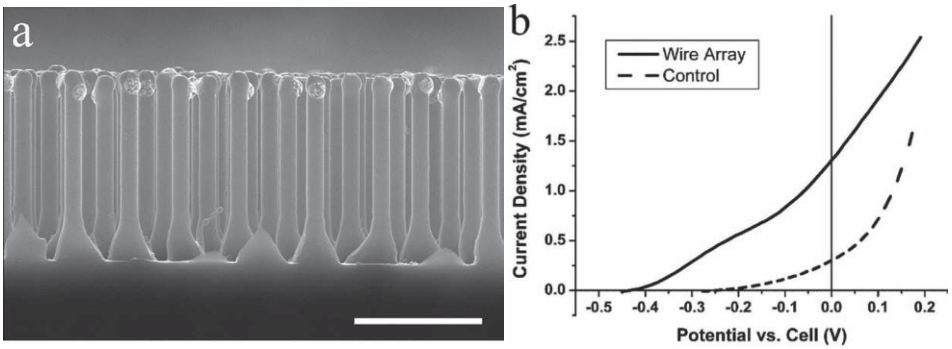

Figure 3.12 (a) SEM image of fabricated SiMW array, and (b) relationship between current density and voltage for SiMW array (solid) line and control sample (dashed) line.[78]

3.6.3.2 PEC Solar Cells Based on MACE Silicon Nanowire Arrays

MACE method for fabrication SiNW arrays has different advantages that make it better than the VLS and OAG growth. MACE is very sample, low cost, and growth at low temperature. [85, 86] PEC cell by MACE SiNW arrays has been fabricated by peng et al. The PEC cell contains an electrolyte of 40% hydrobromic acid and 3% bromine solutions that is suitable for wetting of all Si nanowires. [80, 81] The n-SiNW arrays at the PEC cell were acted as photoelectrode and Pt mesh was performed as the counter electrode. The cell was under illumination AM1.5G and the measurements of current and voltage were taken by using a Princeton electrochemical workstation. The results of I-V demonstrated that the SiNWs are photoactive and promoting for properties of photovoltaic. This cell has medium performance with low efficiency (<1%) due to roughness of the surface, poor carrier collection and extreme recombination. For improving the performance of the cell, metallic nanoparticles were coated on n-SiNW to promote the solar energy conversion (Figure 3.13). [86] Using nanoparticle – SiNW has unique advantage beside the advantages of making short carrier collection and enhancing absorption of the wavelength of the visible light. First, the fabricated SiNWs are efficient for charge carrier transport process due to the 1D pathway of SiNW. Second, metallic nanoparticles used as catalyst for electrochemical reactions that happen on the SiNWs electrode. Third, the impinging light, which is between SiNWs, has been scattered by metallic nanoparticles; as a result, the absorption of light has been increased. This type of photovoltaic as shown

in Figure 3.13 c made enhancements in the short-circuit current density (I_{sc}) from 1.74 to 12.73 mA cm^{-2}. Figure 3.13 c shows the characteristics of photochemical cell solar cells under illumination that done by different electrodes of n-Si. The fill factor (FF) of the photovoltaic increased through decoration with Pt nanoparticles. Moreover, there is relationship between the efficiency of the PEC and the amount of Pt nanoparticles. For optimal Pt nanoparticles, the efficiency reaches its maximum 8.14 % (Figure 3.13 d). If the pt deposition of Pt is lengthy on SiNW, the photocurrent and fill factor decrease due to formation of a porous Si layer that has high resistance.

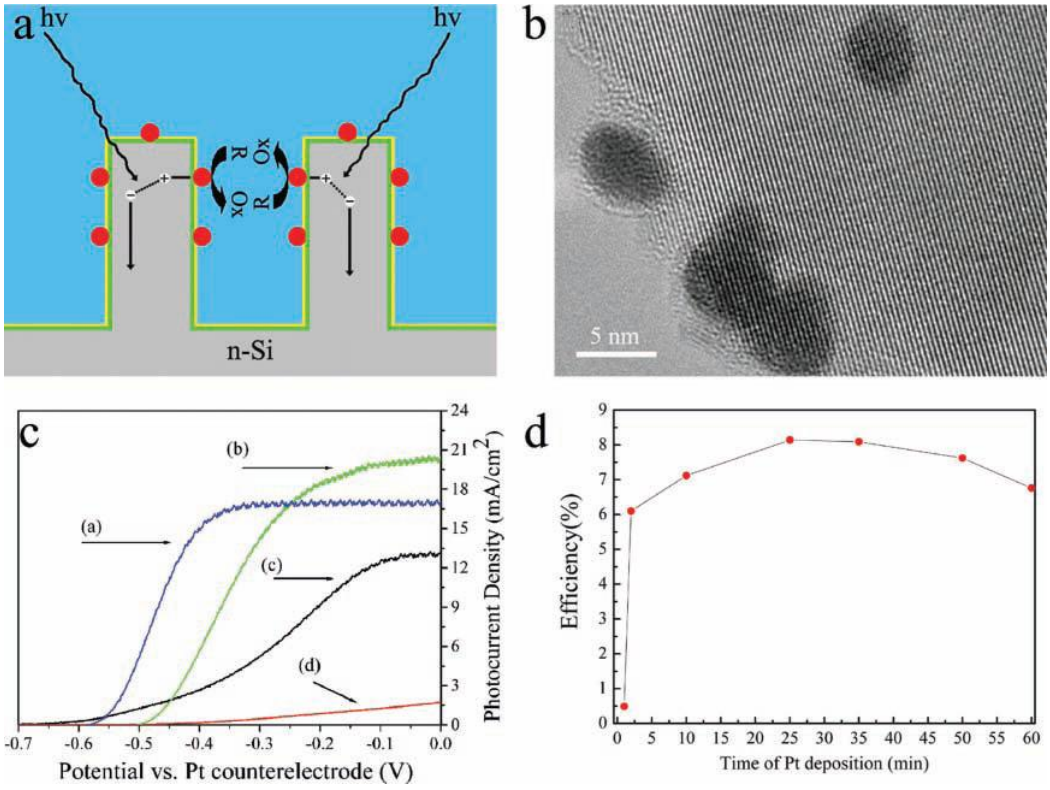

Figure. 3.13 (a) Schematic presentation of a Pt nanoparticle – decorated SiNW array, (b) TEM image of a Pt nanoparticle – decorated SiNW, (c) I-V curve of a Pt nanoparticle – decorated SiNW under illumination, a naked planar n-Si electrode, and a naked n-SiNW array electrode, and (d) the effect of the time of the pt deposition on the efficiency of the PEC. [81]

References

[1] D. M. Chapin, C. S. Fuller, G. L. Pearson, “A New Silicon p-n Junction Photocell for Converting Solar Radiation into Electrical Power” J. Appl. Phys. 25,676. 1954.
[2] Goetzberger, Adolf, Christopher Hebling, and Hans-Werner Schock. "Photovoltaic materials, history, status and outlook." Materials Science and Engineering: R: Reports 40.1 (2003): 1-46.
[3] Swanson, Richard M. "A vision for crystalline silicon photovoltaics." Progress in photovoltaics: Research and Applications 14.5 (2006): 443-453.
[4] Green, M. A. "Recent developments in photovoltaics." Solar energy 76.1 (2004): 3-8.
[5] Alsema, E. A. "Energy pay- back time and CO2 emissions of PV systems." Progress in photovoltaics: research and applications 8.1 (2000): 17-25.
[6] Carlson, D. E., and C. R. WRONSKi. "Optimization of the CVD process for low-cost non-crystalline silicon thin-film solar cells." Appl Phys Letter 28 (1976): 671.
[7] Hoppea, Harald, and Niyazi Serdar Sariciftci. "Organic solar cells: An overview." J. Mater. Res 19.7 (2004): 1925.
[8] Tang, Ching W. "Two- layer organic photovoltaic cell." Applied Physics Letters 48.2 (1986): 183-185.
[9] Kayes, B. M., et al. "IEEE Photo Spec Conf 55–58 Kayes BM." Atwater HA, Lewis NSJ (2005) Appl Phys 97.114302 (2005): 1-11.
[10] O’regan, Brian, and M. Grfitzeli. "A low-cost, high-efficiency solar cell based on dye-sensitized." nature 353 (1991): 737-740.
[11] Bach, U., et al. "Solid-state dye-sensitized mesoporous TiO2 solar cells with high photon-to-electron conversion efficiencies." Nature 395.6702 (1998): 583-585.
[12] Lancelle- Beltran, Emmanuelle, et al. "All- Solid- State Dye- Sensitized Nanoporous TiO2 Hybrid Solar Cells with High Energy- Conversion Efficiency." Advanced Materials 18.19 (2006): 2579-2582.
[13] Huynh, Wendy U., Janke J. Dittmer, and A. Paul Alivisatos. "Hybrid nanorod-polymer solar cells." science 295.5564 (2002): 2425-2427.
[14] Greene, Lori E., et al. "ZnO-TiO2 core-shell nanorod/P3HT solar cells." The Journal of Physical Chemistry C 111.50 (2007): 18451-18456.
[15] Schierhorn, Martin, et al. "Fabrication and electrochemical photovoltaic response of CdSe nanorod arrays." The Journal of Physical Chemistry C 112.23 (2008): 8516-8520.
[16] Takanezawa, Kazuko, Keisuke Tajima, and Kazuhito Hashimoto. "Efficiency enhancement of polymer photovoltaic devices hybridized with ZnO nanorod arrays by the introduction of a vanadium oxide buffer layer." Applied Physics Letters 93.6 (2008): 063308.
[17] Klimov, V. L. "Detailed-balance power conversion limits of nanocrystal-quantum-dot solar cells in the presence of carrier multiplication." Applied Physics Letters 89.12 (2006): 123118-123118.
[18] Guo, Chun Xian, et al. "Layered graphene/quantum dots for photovoltaic devices." Angewandte Chemie International Edition 49.17 (2010): 3014-3017.
[19] Luque, Antonio, Antonio Martí, and Arthur J. Nozik. "Solar cells based on quantum dots: multiple exciton generation and intermediate bands." MRS bulletin 32.03 (2007): 236-241.
[20] Zhou, Hang, et al. "Arrays of Parallel Connected Coaxial

Multiwall- Carbon- Nanotube–Amorphous- Silicon Solar Cells." Advanced Materials 21.38- 39 (2009): 3919-3923.
[21] Gabor, Nathaniel M., et al. "Extremely efficient multiple electron-hole pair generation in carbon nanotube photodiodes." Science 325.5946 (2009): 1367-1371.
[22] Kuo, Cheng Yung, and Chie Gau. "Arrangement of band structure for organic-inorganic photovoltaics embedded with silicon nanowire arrays grown on indium tin oxide glass." Applied Physics Letters 95.5 (2009): 053302.
[23] Liu, Junpeng, et al. "Organic/inorganic hybrid solar cells with vertically oriented ZnO nanowires." Applied Physics Letters 94.17 (2009): 173107.
[24] Wang, Kai, et al. "Direct growth of highly mismatched type II ZnO/ZnSe core/shell nanowire arrays on transparent conducting oxide substrates for solar cell applications." Advanced Materials 20.17 (2008): 3248-3253.
[25] Scheel, H., S. Reich, and C. Thomsen. "Electronic band structure of high- index silicon nanowires." physica status solidi (b) 242.12 (2005): 2474-2479.
[26] Xie, Guofeng, et al. "Phonon surface scattering controlled length dependence of thermal conductivity of silicon nanowires." Phys. Chem. Chem. Phys. (2013),15(35):14647-14652.
[27] Adachi, M. M., M. P. Anantram, and K. S. Karim. "Optical properties of crystalline− amorphous core− shell silicon nanowires." Nano letters 10.10 (2010): 4093-4098.
[28] Haraguchi, M. "Electrical Characterization of Nanopolyaniline/Porous Silicon Heterojunction at High Temperatures." Journal of Nanomaterials 2013 (2013).
[29] Martin, Pierre, et al. "Impact of phonon-surface roughness scattering on thermal conductivity of thin Si nanowires." Physical review letters 102.12 (2009): 125503.
[30] Zhang, Baohua, et al. "Large- Area Silver- Coated Silicon Nanowire Arrays for Molecular Sensing Using Surface- Enhanced Raman Spectroscopy." Advanced Functional Materials 18.16 (2008): 2348-2355.
[31] He, Yao, Chunhai Fan, and Shuit-Tong Lee. "Silicon nanostructures for bioapplications." Nano Today 5.4 (2010): 282-295.
[32] Patolsky, Fernando, Gengfeng Zheng, and Charles M. Lieber. "Nanowire-based biosensors." Analytical Chemistry 78.13 (2006): 4260-4269.
[33] Chern, Winston, et al. "Nonlithographic patterning and metal-assisted chemical etching for manufacturing of tunable light-emitting silicon nanowire arrays." Nano letters 10.5 (2010): 1582-1588.
[34] Fang, Hui, et al. "Fabrication of slantingly-aligned silicon nanowire arrays for solar cell applications." Nanotechnology 19.25 (2008): 255703. [35] Jung, Jin-Young, et al. "A strong antireflective solar cell prepared by tapering silicon nanowires." Optics express 18.103 (2010): A286-A292.
[36] Garnett, Erik C., and Peidong Yang. "Silicon nanowire radial p− n junction solar cells." Journal of the American Chemical Society 130.29 (2008): 9224-9225.
[37] Khorasaninejad, M., et al. "Silicon nanowire arrays with enhanced optical properties." Optics letters 37.20 (2012): 4194-4196.
[38] Lee, S. T., et al. "Oxide-assisted semiconductor nanowire growth." MRS bulletin 24.08 (1999): 36-42.
[39] Cui, Yi, et al. "Diameter-controlled synthesis of single-crystal silicon nanowires." Applied Physics Letters 78.15 (2001): 2214-2216.
[40] Kayes, Brendan M., et al. "Growth of vertically aligned Si wire arrays over large

areas (> 1cm2) with Au and Cu catalysts." Applied Physics Letters 91.10 (2007): 103110.
[41] Renard, Vincent T., et al. "Catalyst preparation for CMOS-compatible silicon nanowire synthesis." Nature nanotechnology 4.10 (2009): 654-657. [42] Holmes, Justin D., et al. "Orientation of solution-grown silicon nanowires." Science 287 (2000): 1471.
[43] Lu, Xianmao, et al. "Growth of single crystal silicon nanowires in supercritical solution from tethered gold particles on a silicon substrate." Nano Letters 3.1 (2003): 93-99.
[44] Hanrath, Tobias, and Brian A. Korgel. "Supercritical fluid–liquid–solid (SFLS) synthesis of Si and Ge nanowires seeded by colloidal metal nanocrystals." Advanced Materials 15.5 (2003): 437-440.
[45]W. K. Choi , T. H. Liew , M. K. Dawood , Nano Lett. 2008 , 8 , 3799 .
[46] de Boor, Johannes, et al. "Sub-100 nm silicon nanowires by laser interference lithography and metal-assisted etching." Nanotechnology 21.9 (2010): 095302.
[47] Schmidt, Volker, Stephan Senz, and Ulrich Gösele. "Diameter-dependent growth direction of epitaxial silicon nanowires." Nano letters 5.5 (2005): 931-935.
[48] Huang, Zhipeng, et al. "Oxidation rate effect on the direction of metal-assisted chemical and electrochemical etching of silicon." The Journal of Physical Chemistry C 114.24 (2010): 10683-10690.
[49] Huang, Zhipeng, et al. "Ordered arrays of vertically aligned [110] silicon nanowires by suppressing the crystallographically preferred< 100> etching directions." Nano letters 9.7 (2009): 2519-2525.
[50] Li, X., and P. W. Bohn. "Metal-assisted chemical etching in HF/H 2 O 2 produces porous silicon." Applied Physics Letters 77.16 (2000): 2572-2574.
[51] Chartier, C., S. Bastide, and C. Lévy-Clément. "Metal-assisted chemical etching of silicon in HF–H< sub> 2</sub> O< sub> 2</sub>." Electrochimica Acta 53.17 (2008): 5509-5516.
[52] Li, Hong-Fang, et al. "Biological functionalization and patterning of porous silicon prepared by Pt-assisted chemical etching." Applied Surface Science 256.12 (2010): 4048-4051.
[53] Peng, Kuiqing, et al. "Metal- Particle- Induced, Highly Localized Site- Specific Etching of Si and Formation of Single- Crystalline Si Nanowires in Aqueous Fluoride Solution." Chemistry-A European Journal 12.30 (2006): 7942-7947.
[54] Lee, Chia-Lung, et al. "Pore formation in silicon by wet etching using micrometre-sized metal particles as catalysts." Journal of Materials Chemistry 18.9 (2008): 1015-1020.
[55] Tsujino, Kazuya, and Michio Matsumura. "Morphology of nanoholes formed in silicon by wet etching in solutions containing HF and H< sub> 2</sub> O< sub> 2</sub> at different concentrations using silver nanoparticles as catalysts." Electrochimica Acta 53.1 (2007): 28-34.
[56] Tsujino, Kazuya, and Michio Matsumura. "Boring deep cylindrical nanoholes in silicon using silver nanoparticles as a catalyst." Advanced Materials 17.8 (2005): 1045-1047.
[57] Cruz, Sonaly, Arne Hönig-d'Orville, and Jörg Müller. "Fabrication and optimization of porous silicon substrates for diffusion membrane applications." Journal of the Electrochemical Society 152.6 (2005): C418-C424.
[58] Peng, K. Q., et al. "Fabrication of Single- Crystalline Silicon Nanowires by

Scratching a Silicon Surface with Catalytic Metal Particles." Advanced Functional Materials 16.3 (2006): 387-394.
[59] Cheng, S. L., C. H. Chung, and H. C. Lee. "A study of the synthesis, characterization, and kinetics of vertical silicon nanowire arrays on (001) Si substrates." Journal of The Electrochemical Society 155.11 (2008): D711-D714.
[60] Kelzenberg, Michael D., et al. "Enhanced absorption and carrier collection in Si wire arrays for photovoltaic applications." Nature materials 9.3 (2010): 239-244.
[61] Yoon, Jongseung, et al. "Ultrathin silicon solar microcells for semitransparent, mechanically flexible and microconcentrator module designs." Nature materials 7.11 (2008): 907-915.
[62] Shir, Dan, et al. "Performance of ultrathin silicon solar microcells with nanostructures of relief formed by soft imprint lithography for broad band absorption enhancement." Nano letters 10.8 (2010): 3041-3046.
[63] Fan, Zhiyong, et al. "Three-dimensional nanopillar-array photovoltaics on low-cost and flexible substrates." Nature materials 8.8 (2009): 648-653.
[64] Yeo, Chan Il, et al. "Wafer-scale broadband antireflective silicon fabricated by metal-assisted chemical etching using spin-coating Ag ink." Optics express 19.105 (2011): A1109-A1116.
[65] Sivakov, V., et al. "Silicon nanowire-based solar cells on glass: synthesis, optical properties, and cell parameters." Nano letters 9.4 (2009): 1549-1554.
[66] Shih, Min-Yi, et al. "Strong broadband optical absorption in silicon nanowire films." Journal of Nanophotonics 1.1 (2007): 013552-013552.
[67] Garnett, Erik, and Peidong Yang. "Light trapping in silicon nanowire solar cells." Nano letters 10.3 (2010): 1082-1087.
[68] Li, Junshuai, et al. "Si nanopillar array optimization on Si thin films for solar energy harvesting." Applied Physics Letters 95.3 (2009): 033102.
[69] Hu, Lu, and Gang Chen. "Analysis of optical absorption in silicon nanowire arrays for photovoltaic applications." Nano letters 7.11 (2007): 3249-3252.
[70] Lin, Chenxi, and Michelle L. Povinelli. "Optical absorption enhancement in silicon nanowire arrays with a large lattice constant for photovoltaic applications." Optics express 17.22 (2009): 19371-19381.
[71] Street, Robert A., William S. Wong, and Christopher Paulson. "Analytic model for diffuse reflectivity of silicon nanowire mats." Nano letters 9.10 (2009): 3494-3497.
[72] Tian, Bozhi, et al. "Coaxial silicon nanowires as solar cells and nanoelectronic power sources." Nature 449.7164 (2007): 885-889.
[73] Gunawan, Oki, and Supratik Guha. "Characteristics of vapor–liquid–solid grown silicon nanowire solar cells." Solar Energy Materials and Solar Cells 93.8 (2009): 1388-1393.
[74] Tian, Bozhi, Thomas J. Kempa, and Charles M. Lieber. "Single nanowire photovoltaics." Chemical Society Reviews 38.1 (2009): 16-24. [75] Tsakalakos, L., et al. "Silicon nanowire solar cells." Applied Physics Letters 91.23 (2007): 233117.
[76] Jung, Jin-Young, et al. "A waferscale Si wire solar cell using radial and bulk p–n junctions." Nanotechnology 21.44 (2010): 445303.
[77] Peng, Kui-Qing, et al. "High-performance silicon nanohole solar cells." Journal of the American Chemical Society 132.20 (2010): 6872-6873.
[78] Maiolo, James R., et al. "High aspect ratio silicon wire array photoelectrochemical

cells." Journal of the American Chemical Society 129.41 (2007): 12346-12347.
[79] Goodey, Adrian P., et al. "Silicon nanowire array photoelectrochemical cells." Journal of the American Chemical Society 129.41 (2007): 12344-12345.
[80] Peng, Kuiqing, Xin Wang, and Shuit-Tong Lee. "Silicon nanowire array photoelectrochemical solar cells." Applied Physics Letters 92.16 (2008): 163103.
[81] Peng, Kui-Qing, et al. "Platinum nanoparticle decorated silicon nanowires for efficient solar energy conversion." Nano letters 9.11 (2009): 3704-3709.
[82] Dalchiele, Enrique A., et al. "Single-crystalline silicon nanowire array-based photoelectrochemical cells." Journal of The Electrochemical Society 156.5 (2009): K77-K81.
[83] Yuan, Guangbi, et al. "Synthesis and photoelectrochemical study of vertically aligned silicon nanowire arrays." Angewandte Chemie 121.51 (2009): 9860-9864.
[84] Shu, Qinke, et al. "Hybrid heterojunction and photoelectrochemistry solar cell based on silicon nanowires and double-walled carbon nanotubes." Nano letters 9.12 (2009): 4338-4342.
[85] Peng, Kui-Qing, et al. "Synthesis of large-area silicon nanowire arrays via self-assembling nanoelectrochemistry." Advanced Materials 14.16 (2002): 1164.
[86] Peng, Kuiqing, et al. "Uniform, Axial- Orientation Alignment of One- Dimensional Single- Crystal Silicon Nanostructure Arrays." Angewandte Chemie International Edition 44.18 (2005): 2737-2742.

Chapter 4

4. Experimental Setup

In this chapter, the fabrication steps of Si nanowires using metal-assisted chemical etching method is presented in details.

4.1 Growth SiNWs Using MACE Method:

4.1.1 Sample Preparation:

Before growth, the samples have to be cleaned starting from organic and ionic contaminations using sequence of chemical treatments. All used chemicals do not react with Si. The sequence of steps is as the follows:

General Cleaning: it is simple cleaning by using acetone and ethanol for 10 and 5 min, respectively. The wafer is then steeped in sulfuric acid and hydrogen peroxide solution [H_2SO_4 (97%): H_2O_2 (35%) = 4:1 v: v] for 15 min at 80 ^oC, and thoroughly rinsed with deionized water. This solution removes the organic and inorganic contaminations from the substrate.

Particle Removal: The cleaned Si pieces were steeped in boiling solution containing ammonium hydroxide, hydrogen peroxide and water [NH_4OH: H_2O_2: H_2O = 1:1:5 v: v: v] for 15 min, thoroughly rinsed with deionized water. This solution also removes organic and metal contaminations from the surface of the substrate.

Oxide Removal: Finally, Si pieces were immersed in dilute HF (10%) for 1 min to remove the native oxide layer from the surface of the substrate, then cleaned with DI water.

4.1.2 Deposition of metal layer

Using noble metals such as Au, Ag, and Cu as catalysts in the etching process is very important as Si covered by a metal layer is etched faster than pare Si. **Chapter 3** lists the various types of metals and the effect of using each one on the structure of the fabricated SiNWs. In our experiment, Silver was used to make metal layer using a mixture of silver nitrate (0.005 M $AgNO_3$) and HF (4 M HF) acid solution at room temperature for 1 min.

4.1.3 Growth of SiNW with different diameters and lengths:

After metal deposition, the sample was immersed immediately in solution of 10% HF and 6% H_2O_2 at 60-80 ^oC for 13-27 min to fabricate SiNWs with different diameters and lengths. For obtaining diameter ~ 120 nm and length ~ 8 µm, the sample was immersed

in solution for 13 min at 60-80 ^{o}C. If the demanded diameter is ~ 200 and length ~ 10.5 µm, the sample should be immersed in solution for 16 min at 60-80 ^{o}C.

4.1.4 Removing the remaining silver nanoparticles

Finally, the remaining silver nanoparticles on the surface of the substrate should be removed. The dilute nitric acid solution is used for removing all silver nanoparticles by immersing the sample in HNO_3 (30%) solution for 20 seconds.

Table 4.1 Summary of the fabrication processes of SiNWs:

Step	Name	Chemicals	Immersion time	Temperature	Properties
1	Sample preparation	H_2SO_4 +H_2O_2	15 min	80 ^{o}C	Removal of the organic and inorganic contaminations
		NH_4OH+ H_2O_2+ H_2O	15 min	80 ^{o}C	Removal of the organic and metal contaminations
		Dilute HF (10%) Sol.	1 min	Room temperature	Removal of the native oxide layer
2	Deposition of metal layer	$AgNO_3$ (0.005 M) + HF (4 M)	1 min	Room temperature	Depositing of silver layer
3	Growth of SiNWs	10% HF and 6% H_2O_2	13:27 min	60-80 ^{o}C	Growing SiNWs with different d and L.
4	Removing silver nanoparticles	HNO_3 (30%)	20 sec	Room temperature	Removal of Ag nanoparticles

Table 4.2 Summery of the obtained length and diameter of the fabricated SiNWs at different etching time

Etching Time	Diameter of SiNWs	Length of SiNWs
13 min	120-170 ± 7.15 nm	8.5 ± 0.3919 µm
16 min	180-280 ± 10.75 nm	10.5 ± 0.44623 µm
19 min	300-380 ± 16.25 nm	12.5 ± 0.588 µm
22 min	400-450 ± 21.25 nm	15.5 ± 0.773 µm
25 min	500-650 ± 28.75 nm	18.5 ± 0.913 µm

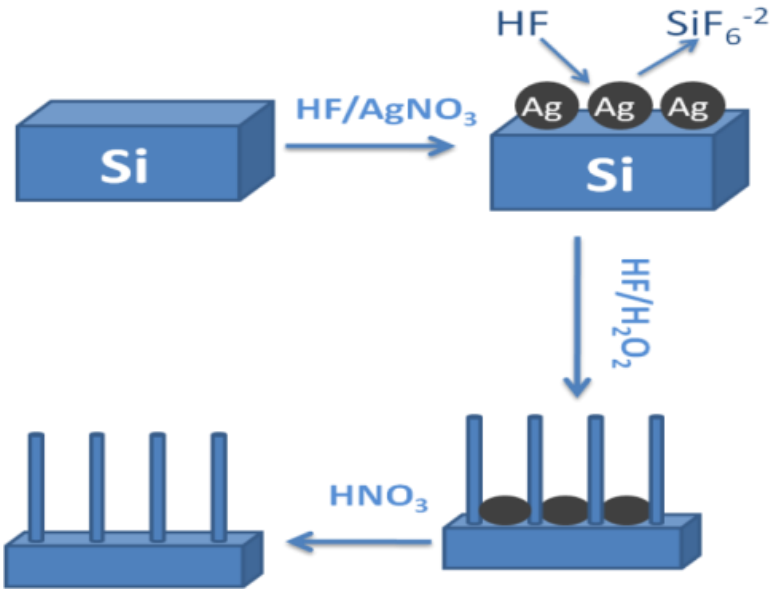

Figure 4.1: A schematic of the fabrication process of SiNWs by MACE

4.2 Characterization Techniques:

4.2.1 Morphological and Structural characterization

The morphology of the fabricated SiNWs was investigated using a Zeiss Ultra60 field emission scanning electron microscope (FESEM) and FESEM- Zeiss 1550 VP equipped with EDS (Energy dispersive X-ray spectroscopy) detector. High-resolution transmission

electron microscope (HRTEM) JEM- 2100 with selected area electron diffraction capability (SAED) has been used for investigating the crystallinity of the fabricated SiNWs. Moreover, X-ray diffraction (XRD) using Cu Kα1 radiation source (λ = 1.5406 Å) was used to investigate the crystal structure of the SiNWs.

4.2.2 Optical Characterizations

The UV−vis absorption spectra were performed using a Perkin-Elmer Lambda UV−vis−NIR spectrophotometer with solid-sample holder for reflectance measurements and an integrating sphere. The measurements of photoluminescence were performed with RF-5301 Pc (Spectrofluorophotometer) using xenon Lamp and excitation wavelength of 325 nm at room temperature. While Raman measurements were performed by using Raman microscope (ProRaman-L Analyzer with an excitation laser beam wavelength of 532 nm.

4.2.3 I-V characterizations

The setup used for the photoelectrochemical characterization of the fabricated SiNWs is shown in Figure 4.2. The SiNWs sample was drawn by copper contact with conduction silver epoxy. The sample acts as the anode in a three-electrode electrochemical cell. The reference electrode in our cell was saturated Ag/AgCl and counter electrode was platinum foil. The electrolyte was HF 10% (pH ~ 4.5) or a mixture of hydrobromic acid (40%) and bromine (3%). A scanning potentiostat (CH Instruments, model CHI 600B) was used to measure current in dark and under illumination at a scan rate of 10 mV/s. A 300W xenon lamp (Spectra physics) was used as the light source, with AM 1.5 filter (Oriel) used to prevent the incident light with wavelength range 320-400 nm. The incident power was 100 mW cm^{-2}, which was determined by using a power detector (Spectra Physics, CA, USA).

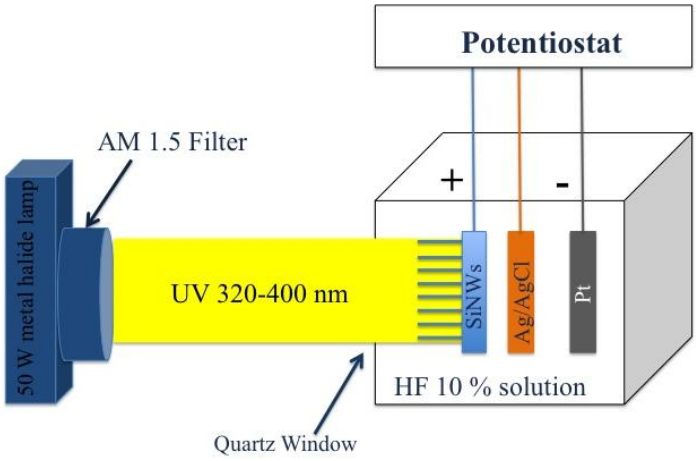

Figure 4.2 a schematic for setup of photochemical cell

References

[1] Sara Abdel Razek, Mohamed A. Swillam and Nageh K. Allam " Vertically-aligned crystalline silicon nanowires with controlled diameters for energy conversion applications: Experimental and theoretical insights" Journal of Applied Physics 115, 2014.

Chapter 5

Results and Discussion

5.1 Fabrication of SiNWs:

5.1.1 Effect of H_2O_2:

The effect of H_2O_2 concentration on the fabricated SiNWs via metal-assisted chemical etching was investigated. The etching solution consisted of HF/H_2O_2 mixture. The concentration of H_2O_2 has been changed from 0.2 to 0.4 M at room temperature.

Figures 5.1, 5.2, and 5.3 show the FESEM images of the fabricated SiNWs using different concentrations of H_2O_2. Increasing the H_2O_2 concentration of H_2O_2 resulted in better nanostructured Si morphologies. High density SiNWs were resulted upon the use of 0.2 M H_2O_2, which decreases with increasing the H_2O_2 concentration to 0.3M. The space between the nanowires also increases with increasing H_2O_2 concentration. Further increase in the concentration of H_2O_2 to 0.4 M (Figure 5.3) resulted in the formation of the porous structures with increasing the etching rate in the horizontal direction. This increase in the etching rate was more than that in the vertical direction, leading to the formation of a chaotic porous structure instead of SiNWs on the substrate.

After immersing Si substrate in $AgNO_3$ solution, Ag ions capture electrons and are deposited on the surface of the Si substrate in the form of metallic silver nuclei. At the same time of deposition, the Si is oxidized to SiO_2. As mentioned in Chapter 3, the presence of silver nanoparticles made etching rate faster in the vertical direction where nanoparticles form pits and then sink in these pits due to gravity. With increasing the concentration of H_2O_2, the oxidant speed increases; as a result, the etching speed in the horizontal direction increases. When the concentration of H_2O_2 is 0.2 M in solution, more Si will be converted into SiO_2 and then dissolved in HF. Consequently, the density of the fabricated SiNWs decreases and the space between nanowires increases. For further increase of concentration of H_2O_2 (0.4 M), the etching speed in the horizontal direction increases and overcomes the nanoparticles of silver gravity to shift its position; as a result, a chaotic porous structure fabricated instead of SiNWs on the Si substrate.

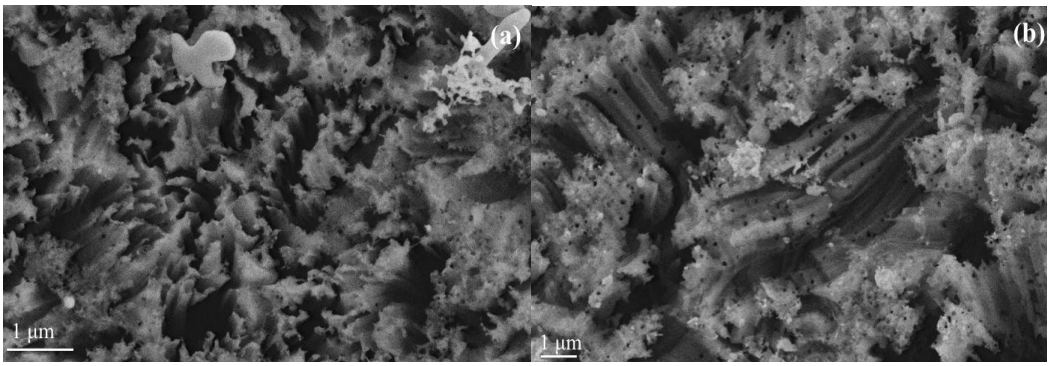

Figure 5.1: (a) top and (b) cross sectional FESEM views of the fabricated SiNWs in the presence of 0.2 M H_2O_2.

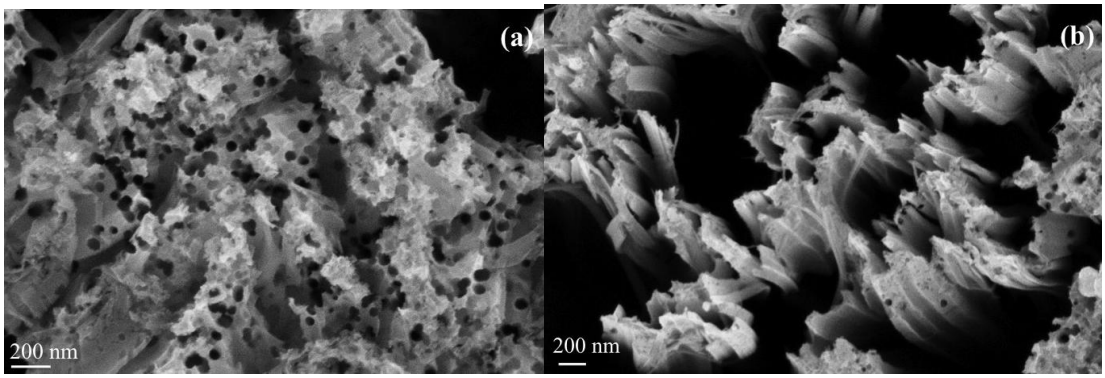

Figure 5.2: (a) top and (b) cross sectional FESEM views of the fabricated SiNWs in the presence of 0.3 M H_2O_2.

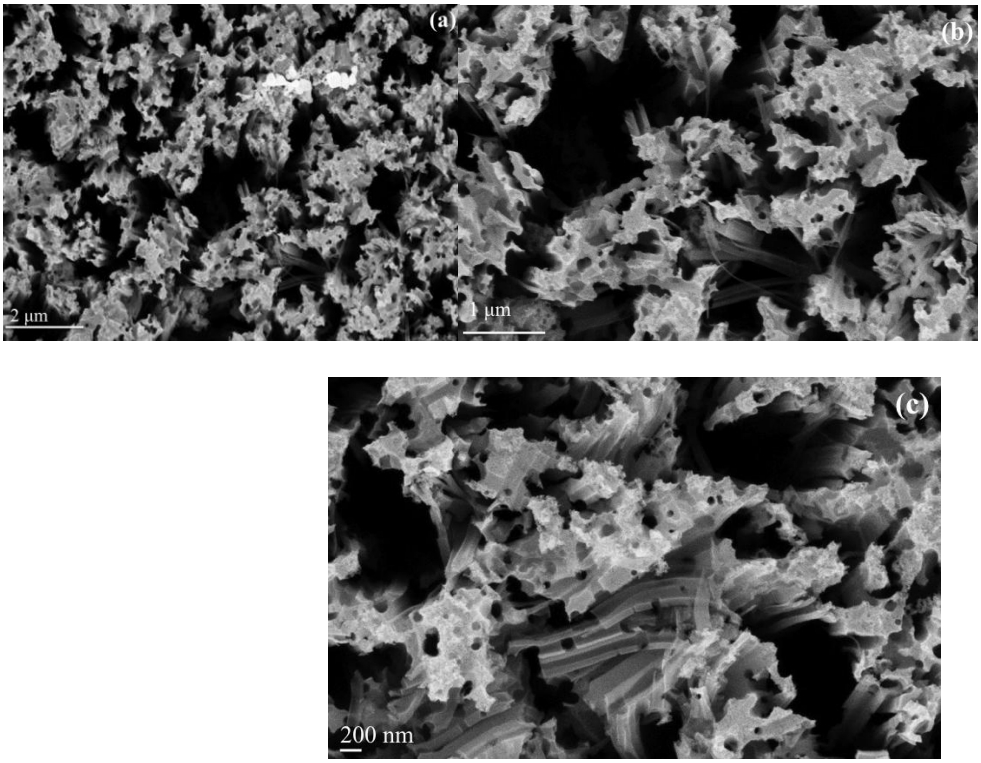

Figure 5.3: (a,b) Top and (c) cross sectional FESEM views with different magnifications of the fabricated SiNWs in the presence of 0.2 M H_2O_2.

5.1.2 Effect of $AgNO_3$ concentrations and different methods of removing the remaining Ag nanoparticles:

The morphologies of the resulting Si nanostructures were found to depend on the concentration of $AgNO_3$ used in the HF/$AgNO_3$ solution. When the concentration of $AgNO_3$ is lower than 0.005M, no SiNWs were observed because the silver nanoparticles form unconnected islands (Figure 5.4). However, when the concentration of $AgNO_3$ is increased to 0.005 M, the islands start to connect together and form non-circular clusters. When the concentration of $AgNO_3$ reaches 0.01 and 0.015 M, the nanoparticles of silver form dendrites. With increasing the $AgNO_3$ concentration, the rate of the deposition of silver increases. For further increase of concentration, the nanoparticles will grow up and form a stacked layer of dendrites.

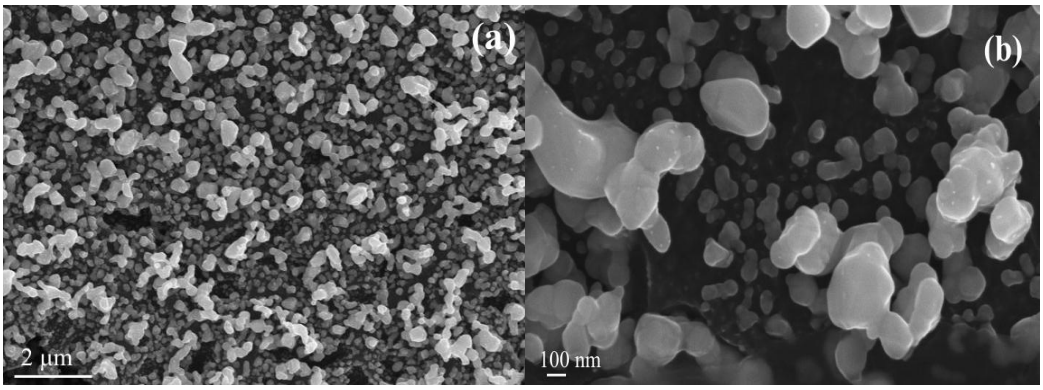

Figure 5.4 (a) and (b) FESEM of silver nanoparticles when the concentration of $AgNO_3$ was lower than 0.005 M.

When Si is etched by HF/$AgNO_3$, the Ag nanoparticles enter the holes as they are shaping. If the size of these nanoparticles is small, their lift-off action may occur through the dissolution of Si, and disordered Si structures resulted. In contrast, stable Ag nanoparticles would help in the formation of one-dimensional Si nanostructures.

When the concentration of $AgNO_3$ is between 0.005 and 0.015 M, aligned vertical Si nanowires formed. However, when the concentration of $AgNO_3$ increases, the density of the SiNWs decreases. When the concentration of $AgNO_3$ increases, the size of the clusters also increases and the areas without silver decreases. As mentioned in Chapter 3, the areas of Si substrate covered with silver are etched faster. If the area with silver increases, the Si nanowires density must be decreased.

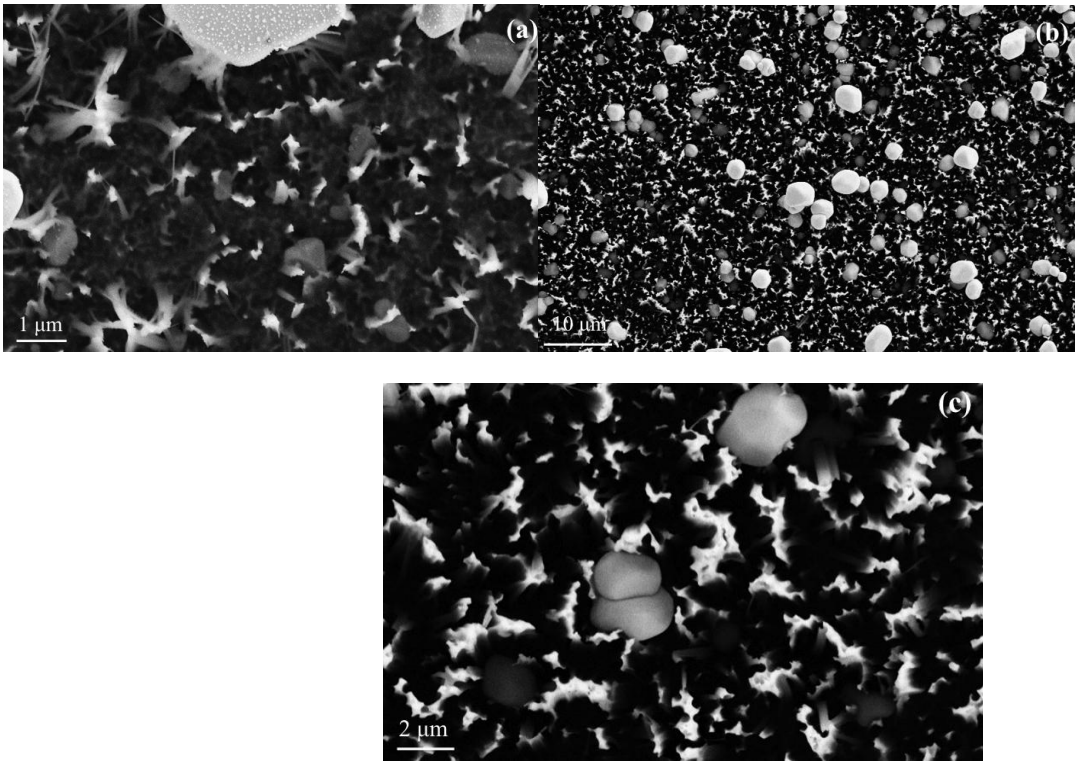

Figure 5.5 (a) , (b) FESEM of SiNWs when the concentration of $AgNO_3$ was 0.01 M at room temp., (c) FESEM of SiNWs when the concentration of $AgNO_3$ was lower than 0.015 M at 50^{o}C for 20 min.

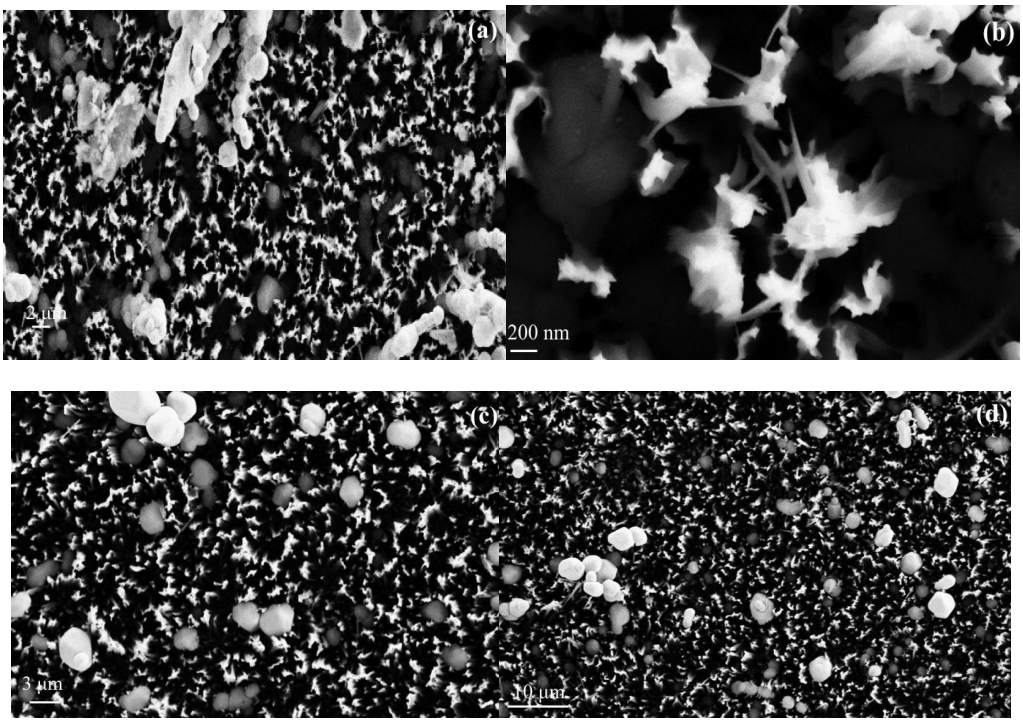

Figure 5.6 (a) , (b) FESEM of SiNWs when the concentration of $AgNO_3$ was 0.015 M at room temp., (c) and (d) FESEM of SiNWs when the concentration of $AgNO_3$ was lower than 0.015 M at 50^{o}C for 20 min.

5.2 Morphologies of the fabricated SiNWs:

Figures 5.7, 8, 9,10,11 and 12 show the FESEM images of the obtained Si nanowire arrays at different etching times. Note the pronouncing effect of the etching time on the diameter and length of the grown nanowires. The average diameter and length of the nanowires increases with increasing the etching time at temperature 60-80 ^{o}C. For example, the nanowire arrays prepared at 13 min. (Figure 5.8) possessed an average diameter of 143 nm and an average length of 8 μm, while those prepared at 25 min have an average diameter of ~ 600 nm and an average length of ~ 18 μm as shown in Figure 5.12. This indicates the rapidity of the etching process. The concentration of Ag+ ions decreases because Ag+ ions sink in the bottom of the nanowires. This decrease slows the etching rate. Since the reduction – oxidation reactions take place between the bottom of the SiNWs and the top of the substrate.

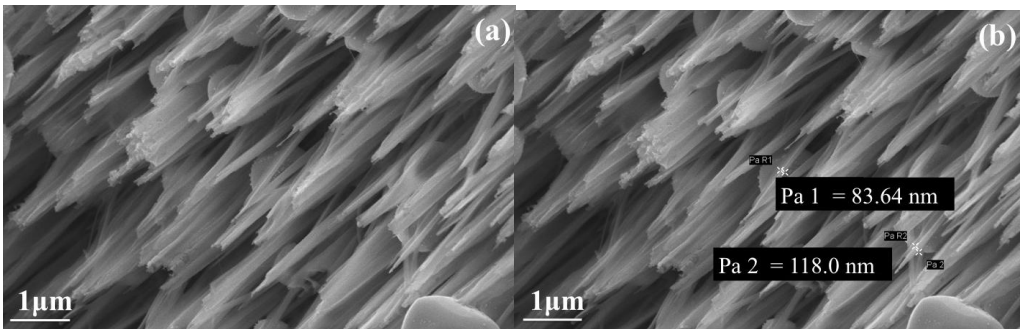

Figure 5.7 (a) and (b) FESEM of the fabricated SiNWs at room temperature when the etching time was 25 min.

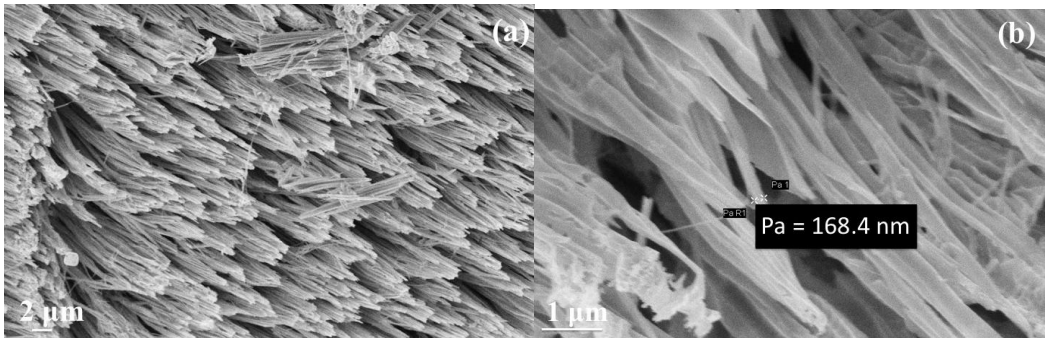

Figure 5.8(a) and (b) FESEM of the fabricated SiNWs with different magnification when temperature was 50^{o}C and etching time was 13 min.

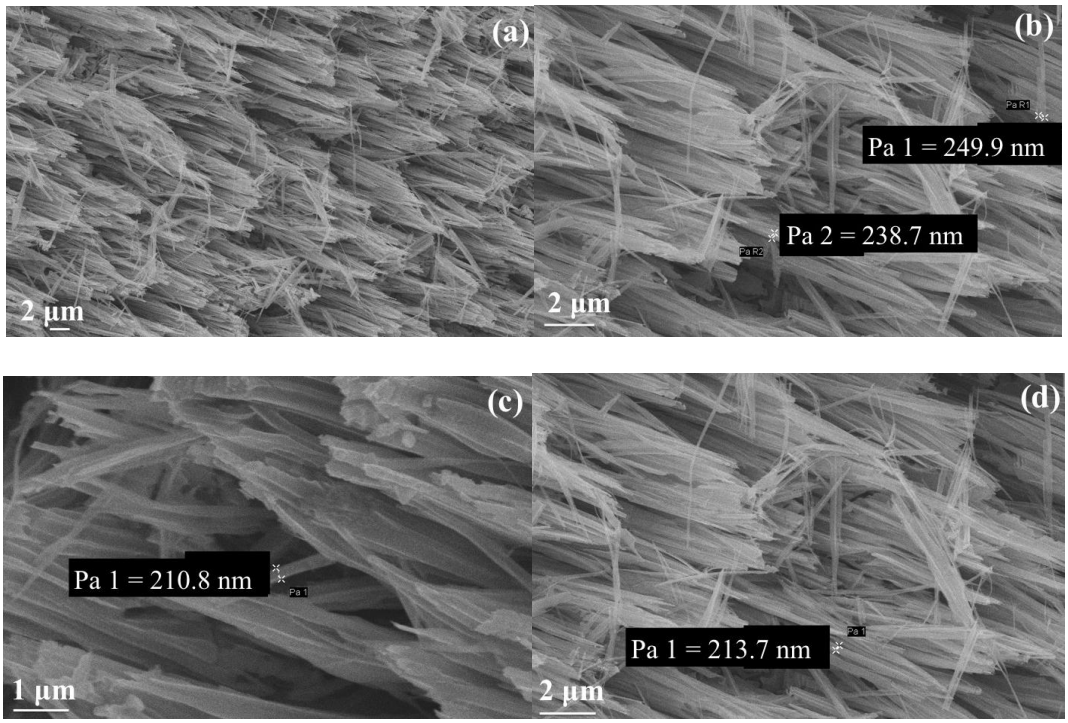

Figure 5.9 (a), (b), (c) and (d) FESEM of the fabricated SiNWs with different magnification and different range of diameters when temperature was 50^{o}C and etching time was 16 min.

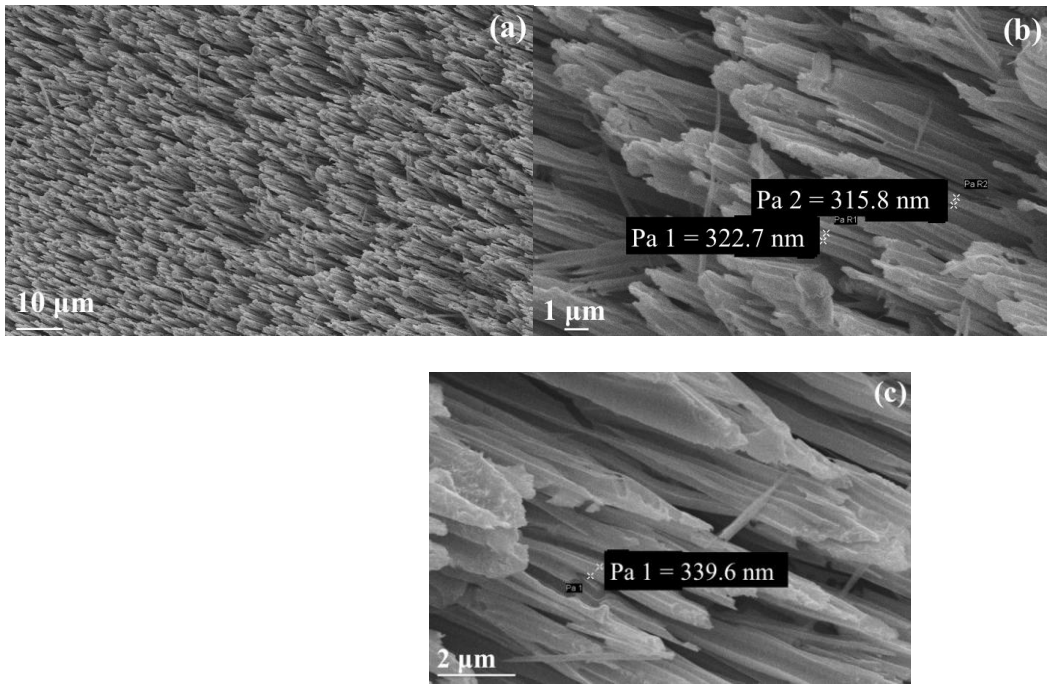

Figure 5.10 (a), (b), and (c) FESEM of the fabricated SiNWs with different magnification and different range of diameters when temperature was 50^{o}C and etching time was 19 min.

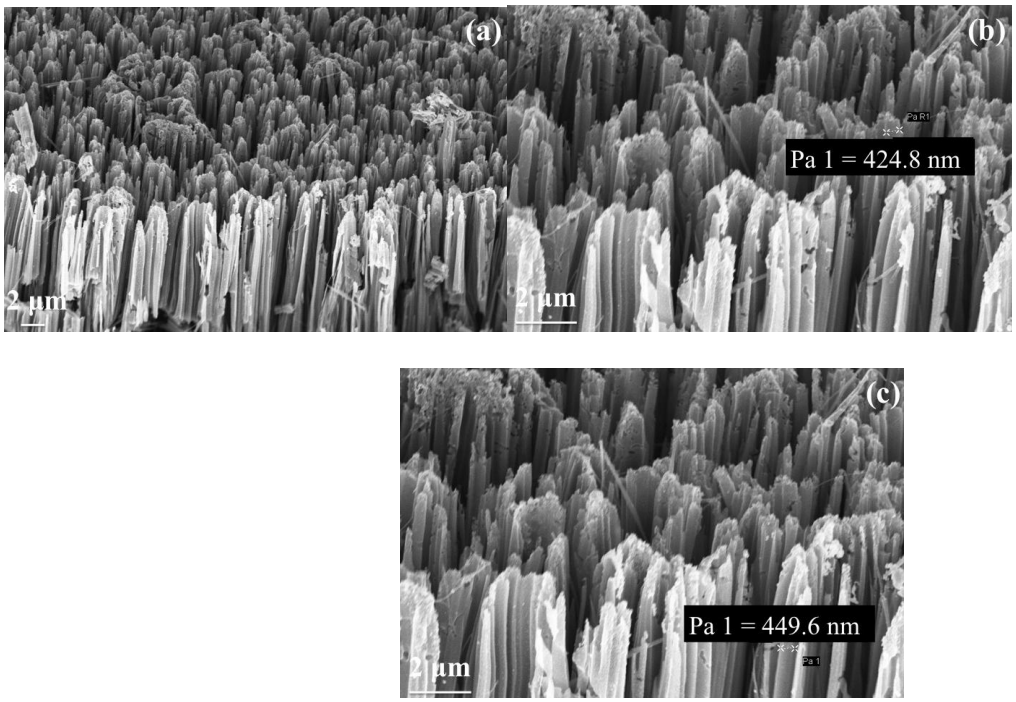

Figure 5.11 (a), (b), and (c) FESEM of the fabricated SiNWs with different magnification and different range of diameters when temperature was 50^{o}C and etching time was 22 min.

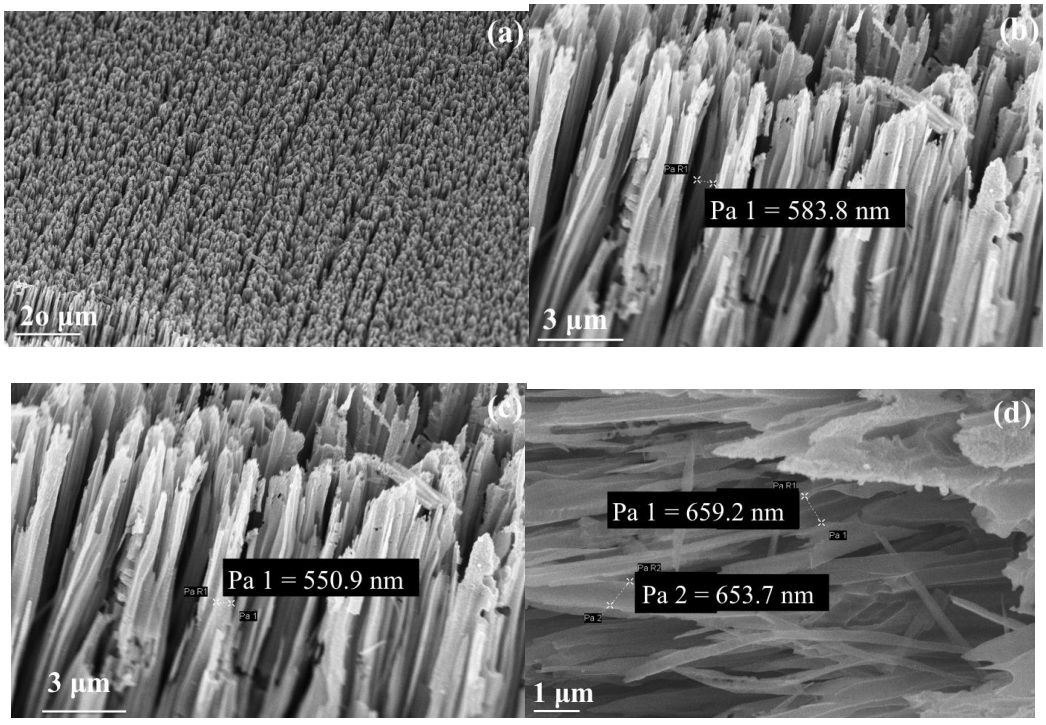

Figure 5.12 (a), (b), (c) and (d) FESEM of the fabricated SiNWs with different magnification and different range of diameters when temperature was 50^{o}C and etching time was 25 min.

The results of the variation in the nanowire' diameters and lengths are summarized in Figure 5.12, which shows the linear increases in length and diameter with increasing the etching time. Note that the length increases from 8 ~ 18 μm and the diameter from 117 nm to 600 nm upon increasing the etching time from 13 to 25 min, corresponding to etching rates of ~ 600 nm/min for the length and ~ 16 nm/min for the diameter. The increase in the diameter of the SiNWs with increasing the etching time may be related to the aggregation of the nanowires.

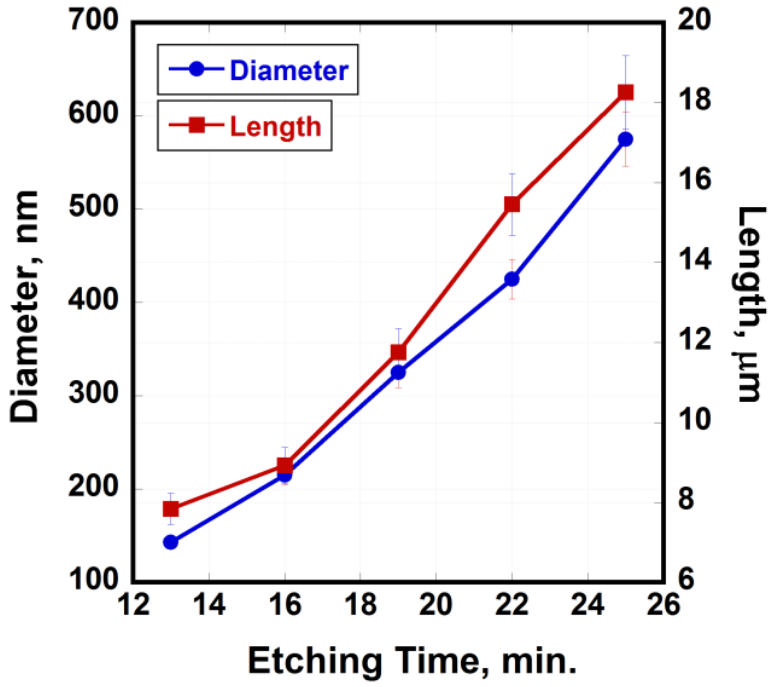

Figure 5.13: Variation of the diameter and length of the Fabricated SiNWs as a function of etching time.

The EDX technique has been used to show the percentage of silicon after removing all remaining Ag nanoparticles. Figure 5.14 shows the EDX spectra of the SiNWs samples that synthesized at different etching times, shown the absence of Ag metal that have been used to assist the etching process.

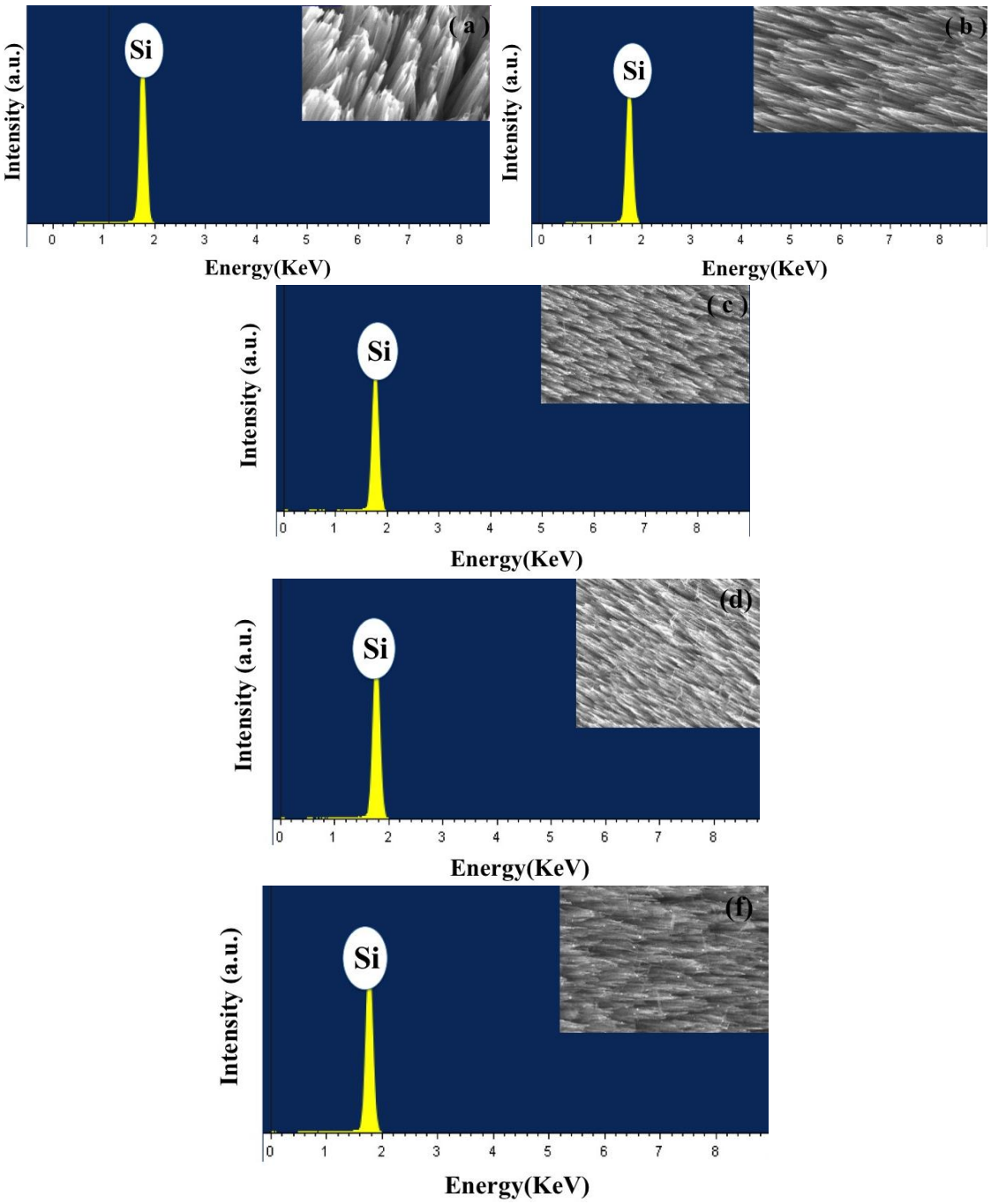

Figure 5.14: EDX of different range of diameters: (a) d ~ 117 : 170 nm, (b) d ~ 180 :270 nm, (c) d~ 300: 380 nm, (d) d~ 400:450 nm and (e) d ~ 500: 650 nm.

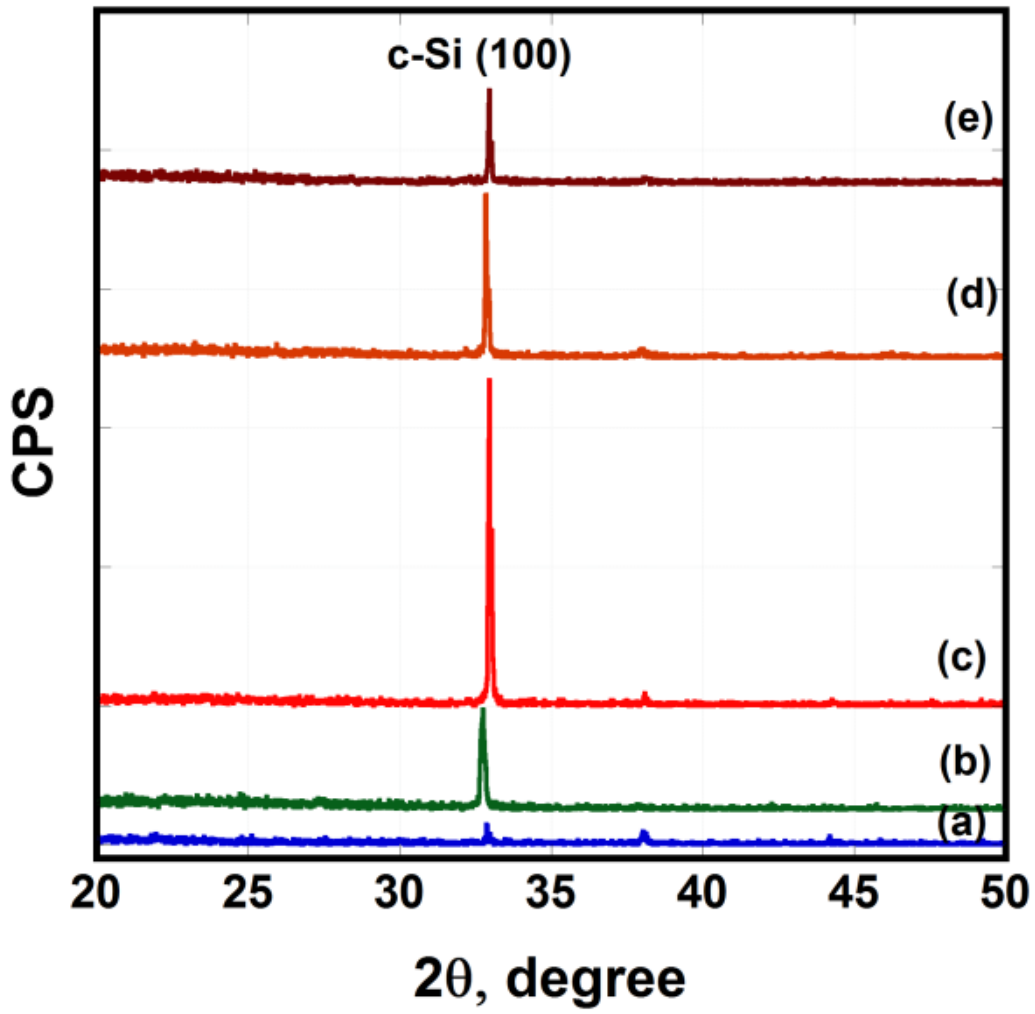

Figure 5.15: XRD patterns of the grown SiNWs at (a) 13 min, (b) 16 min, (c) 19 min, (d) 22 min and (e) 25 min, respectively.

X-ray diffraction (XRD) using Cu Kα1 radiation source (λ = 1.5406 A^o) was used to investigate the crystal structure of the SiNWs. The common diffraction peaks appeared around 33^o can be related to crystalline silicon (c-Si) (100). [1] Where c-Si is better than amorphous silicon (a-Si) for solar cell application because a-Si has high disorder and dangling bonds that makes it a bad conductor for charge carriers and reduce the life time of carrier and pin the Fermi level so that doping the material to n – or p – type is not possible. Also, drop in the efficiency of devices made of a-Si has been reported which was related to the Stabler-Wronski effect, especially when exposed to light. [2] Moreover, the two other small diffraction peaks appeared at 38^o and 44^o in panels can be related to silver oxide and silver, respectively. [3]

The above results were obtained by using normal XRD for all different diameters of SiNWs. For confirming absence of amorphous layer around fabricated Si nanowires, XRD with angle 1^o has been used and compared to the XRD of substrate. The peak of the SiNWs was similar to peak of substrate that is 33^o Figure 5.16. [1]

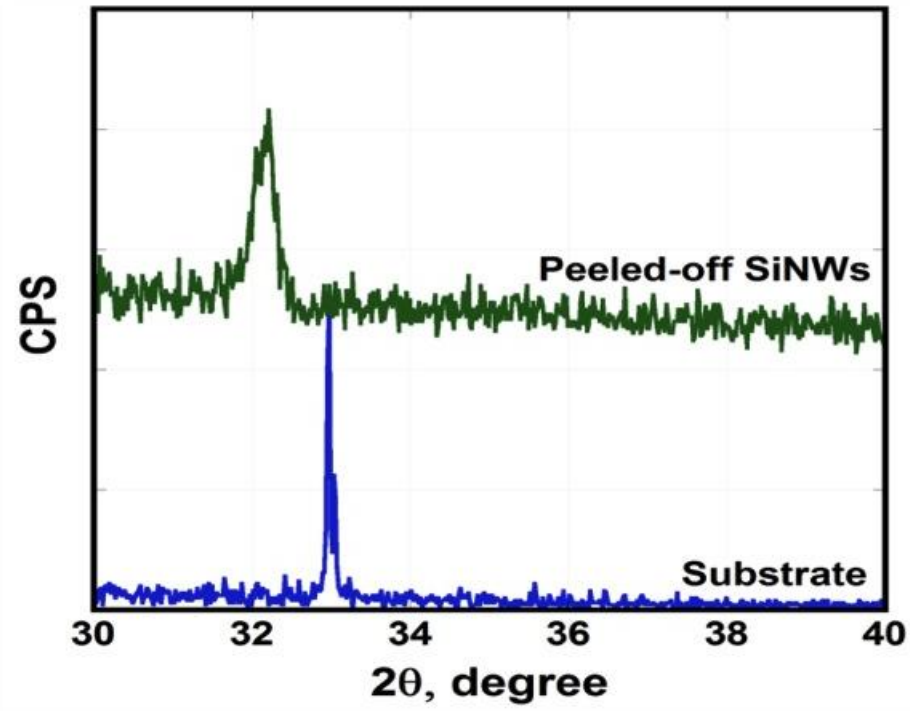

Figure 5.16 comparison of the XRD diffraction patterns of the Si substrate and the peeled-off SiNWs grown by etching for 19 min.

The high-resolution transmission electron microscope (HRTEM) has been used to confirm the crystallinity of the fabricated SiNWs. TEM used focused beam of electrons with high energy in transmitting a sample to show the morphology, crystallography, elemental composition, and particle size distribution of sample. TEM has the ability of giving chemical information and atomic – resolution lattice images. HRTEM has been used in our study because the crystal structures can be investigated because the images are formed due to difference in phase of electron waves that scattered through a thin specimen. [4] Figure 5.17 shows the HR-TEM of the fabricated SiNWs with space .32 nm to confirm the crystallinity.

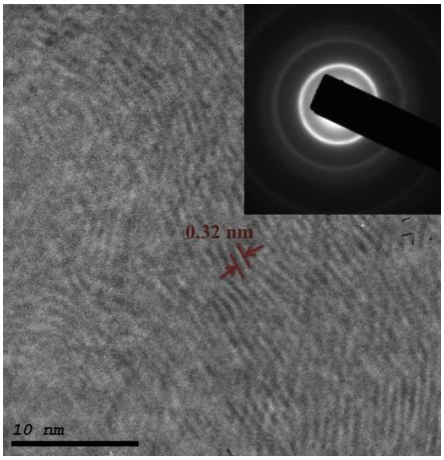

Figure 5.17 HRTEM of the fabricated SiNWs

5.3 Optical characterizations of the fabricated SiNWs:

5.3.1 Optical absorption of SiNWs with different dimensions:

Nanosemiconductors have unique optical and electrical properties that offer advantages in many applications such as solar cells, [5,6] detectors [7,8] and optical sensors. [9,10] In particular for solar cell applications, SiNWs are the most efficient approaches for attaining the third generation solar cells, [11] because SiNWs can be easily integrated in radial p-n junction solar cell devices. The enhancement in the conversion efficiency of the radial p-n junction stems from the ability of the directional separation between carrier collection and light absorption. [12] Using SiNWs for solar cell application decreases the cost of the materials used. Moreover, SiNWs showed strong broadband optical absorption because of light trapping effects. The arrays of SiNW decrease the reflection over a wide range of wavelength and different incident angles of light due to the transition of refractive indices across the air-to-substrate. [13]

The effect of changing dimensions of the SiNWs on the optical reflection has been studied. Figure 5.18 shows the optical refection spectra of the SiNWs fabricated at different etching time. SiNWs with five different averages of diameters are presented to show the influence of the change in diameter on the light scattering characteristics.

In general, the prepared SiNW arrays have low reflectance throughout the entire wavelength range, possibly due to the multiple reflection of light, which increases the optical path length of photons. [14] The SiNWs with diameters in the range 117-170 nm showed reflectance below 4% over the wavelength range 330 – 1000 nm. A minimum reflectance of 2.56% is found at 360 nm. As the diameter of the SiNWs increases to 650 nm, the reflectance increases over the spectral range of 350-860 nm, which is below 10% in the wavelength range 350-750 nm with a minimum reflectance of 4.65 % around 390 nm. However, the reflectance is over 11 % in the near infrared region. Consequently, it seems that increasing the diameter has a significant effect on increasing the reflectance of the SiNWs. This may be attributed to the increase of the effective refractive index of the medium. It was reported that the absorption could be easily calculated from reflectance spectra where the transmittance of silicon in the wavelength region 300-1000 nm is almost zero. [15] The absorption intensity is found to increase with decreasing the SiNWs diameter as shown in Figure 5.18b. This can be explained on the light confinement basis, i.e. increasing the SiNWs diameter would result in a decrease in the confinement of light, causing increased multiple light scattering between the SiNW arrays. [16] Moreover, based on wave optics, the decrease in the reflection can be related to the interaction between incident light and objects. [16] When the dimensions of the objects are mush shorter than the wavelength of the incident light, SiNWs are penetrated without interaction with the incident light. This process can account for the poor absorption of Si nanowire with d ~ 143 nm at long wavelength. If the object dimensions are comparable to the wavelength of the incident light, light scattering from the object will be enhanced, resulting in elongated optical path length and thus increased light harvesting. However if the dimension of the objects is greater than the light wavelength, reflection will become the dominant process.

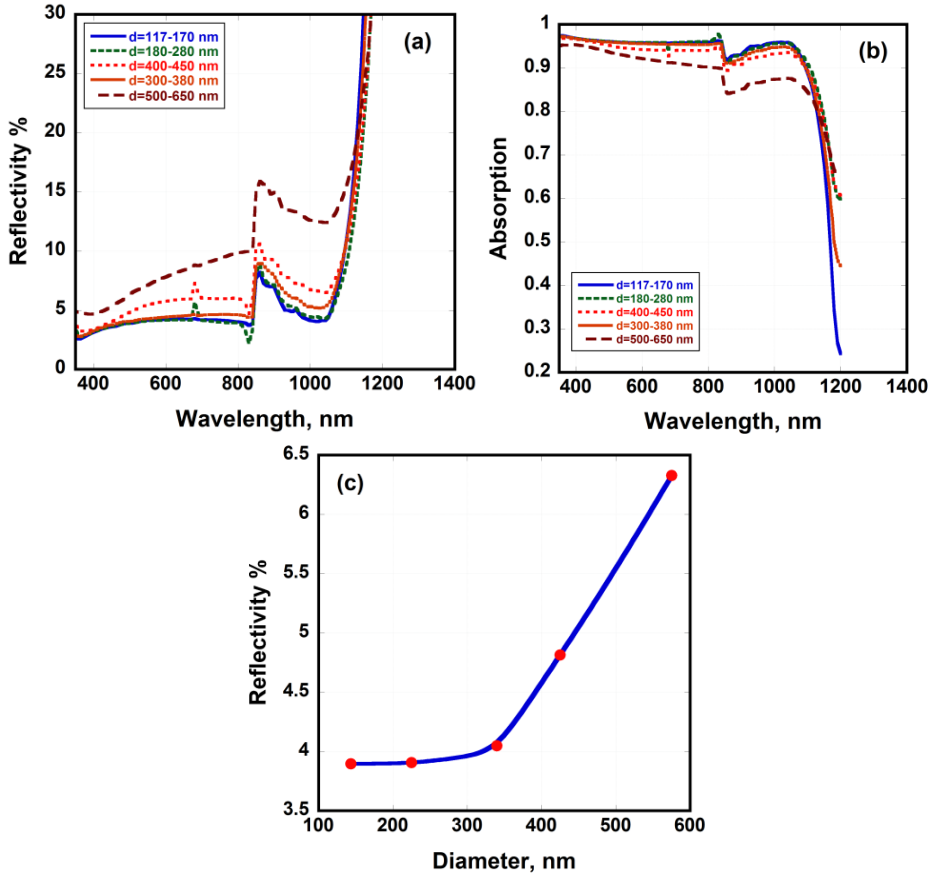

Figure 5.18: Variation of the (a) reflection, (b) absorption, and (c) reflectivity % of the fabricated SiNWs as a function of their diameter at a wavelength of 500 nm.

The length of the fabricated SiNWs has also a significant effect in changing the optical properties. Although long SiNWs absorb light more efficiently, if the length was too long, overlapping would occur between nanowires. The variation in the reflectivity as a function of the SiNWs diameter is summarized in Figure 5.18c.

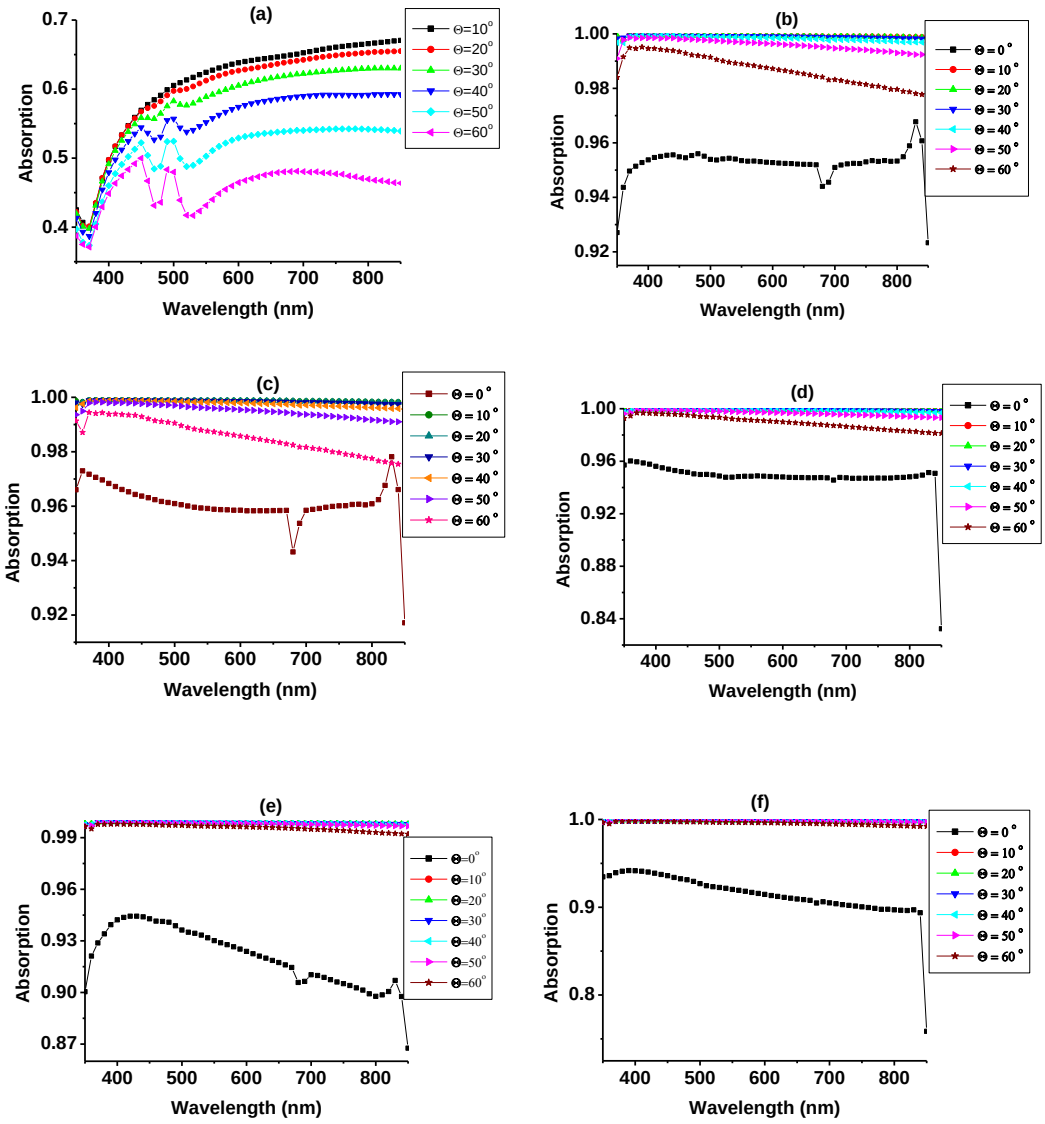

Figure 5.19: Absorption of Si substrate and SiNWs with different ranges of diameters at incident angles (a) Si substrate (b) SiNWs with diameters of 117:170 nm, (c) SiNWs with diameters of 180:270 nm, (d) SiNWs with diameters of 300:380 nm, (e) SiNWs with diameters of 400:450 nm , and (f) SiNWs with diameters of 500:650 nm.

In addition, changing the incident angle of the absorbed light affects on absorption. Figure 5.19 shows the absorption measured at different incident angles (0, 10^o, 20^o, 30^o, 40^o, 50^o, and 60^o) for SiNW arrays with different diameters over the wavelength range of 350 – 850 nm. Because of the vertical orientation of the SiNWs, all arrays of SiNWs showed lower absorption at normal incidence angle (θ = 0) than other angles The Si nanowires with all diameter ranges absorb more light at an angle 10^o as shown in Figure 5.17. King et al. [18] found that with increasing the angle of the incident light, the light

becomes more oblique and decreases the absorption. Generally, the reflection increases with increasing the incident angle of light clearly after 50^{o}.

5.3.2 Photoluminescence of the SiNWs with different diameters:

PL studies different parameters of material. PL spectroscopy can be used to provide electrical characterization of sample, and it is very sensitive to discrete electronic states. PL is a technique that is used to identify the surface, interface, impurity levels, and roughness of the interface. For intensity of the PL, it can be used to study the quality of interfaces and surfaces. Changing the intensity of PL can be used also for mapping the electric field at the surface of a sample.

The PL emission spectrum at room temperature of the fabricated SiNWs has been measured. Figure 5.20a shows significant PL emission in the wavelength range $350 < \lambda < 800$ nm for SiNW arrays with different diameters. There are two peaks observed, the first peak is between 350 and 500 nm and the second peak is between 635 and 670 nm. The intensity of the PL peaks increases with increasing the time of etching till 16 min. Then, PL intensity decreases at 19 min and again increases for 22 and 25 min.

As the etching time increases, PL emission peak shows a red shift, which can be explained by the quantum confinement luminescent center (QCLC) model. [19] According to the quantum confinement model, the emission of the PL depends on the size of the crystallinity of Si because of the transition of the PL emission from band to band; higher size of crystallinity shifts the PL emission peak to longer wavelength. As our samples exposed to air after fabrication, silicon oxide layer may be formed. The grown silicon oxide has different luminescent centers that are responsible for appearing the radiative recombination. As a result of recombination, the red PL shift occurred.

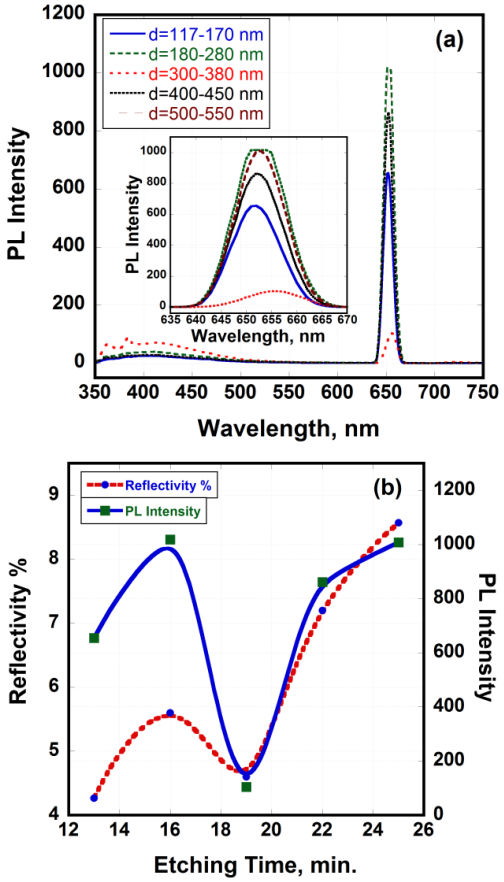

Figure 5.20 (a) PL of different SiNWs diameters, (b) plot of PL and reflectivity at different etching time for wavelength ~ 660 nm.

It is important to correlate the PL emission at ~ 660 nm with the reflectivity of the SiNWs fabricated at different time of etching. As shown in Figure5.20b, as etching time increases, reflectivity and PL intensity both decreases for 13 and 16 min at ~ 660 nm. Then the reflectivity and PL intensity decreases at 19 min and increase again at 22 and 25 min. These two sudden increases of reflectivity and PL intensity for etching time of 19 min cannot be explained on the basis of usual interference of light if SiNW arrays have a refractive index between those of Si and air. It may depend on the porosity of the fabricated SiNWs where the rate of porosity increase with etching time till attaining a certain value that slows down the rate as shown in Figure 5.21. The porosity % of the fabricated SiNWs at 13 min was 79.8 % and then increased to 83.1% at 19 min. The percent of porosity decreased when the etching time was 22 min to ~ 77.7 %.

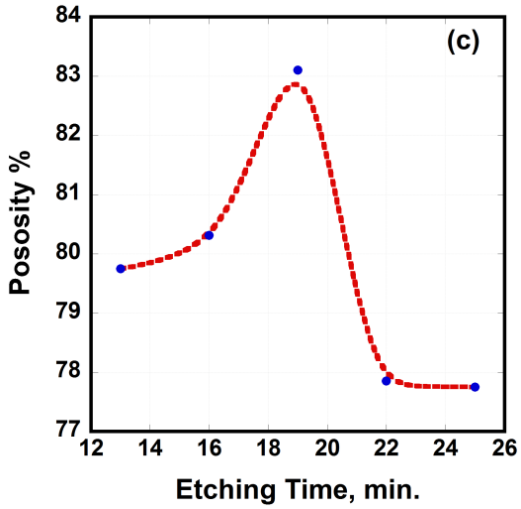

Figure 5.21: the relationship between porosity and etching time.

3.3.3 Raman Spectroscopy

Raman spectroscopy is an efficient method to study quantum confinement in SiNWs, [20] getting information about lattice defect, [21] doping concentration, [22] and crystal orientation. [23] Due to the Heisenberg uncertainty principle, the essential Raman selection rule (q ~0) is relaxed for a finite-size domain, allowing the participation of phonons away from the Brillouim- Zone center. The scattering of phonons is affected by the diameter (d) of nanowires where $\Delta q \sim 1/d$. This is expected to result in a downshift to the Si peak and an asymmetric broadening. [24] The micro-Raman spectra of the SiNWs synthesized at different etching times are shown in Figure 5.22a.

The SiNWs with different diameters show Raman peaks located a round 518 cm^{-1}, corresponding to the first order transverse optical mode (1TO) of c-Si. Compared to the 1TO peak usually seen for c-Si at ~ 520 cm^{-1}, [25] the obtained 1TO peaks for all SiNWs with different diameters are downshifted toward lower frequencies as expected. The broad peaks at 296 and ~ 940 cm^{-1} were related to the second order transverse acoustic phonon mode (2TA) and to the second order transverse optical phonon mode (2TO), respectively. [26] The 2TO peak is a convolution of three phonon scattering events giving rise to peaks at ~ 942 cm^{-1} {TO (X)}, ~ 966 cm^{-1} {TO (W)} and ~ 979 cm^{-1} {TO (L)}.

Richter et al. [27] and Campbell and Facuchet [28] (RCF) reported a model of phonon confinement to evaluate the relationship between the Raman shift and the nanoparticles' size. They found that increasing the diameter of Si nanospheres led to a shift in the 1TO peak toward a higher wave number. The Raman band location and curve shape depended on the size uniformity, crystallinity, and the variation of crystal constants. [28] The crystallinity of the SiNWs decreases with increasing he nanowire diameter, resulting in the 1TO peak towards lower frequencies. [28]

The Raman intensity in the RCF model is given by [27,28]

$$I_{NW}(w) = \mathrm{A}\int_0^{q_{max}} \frac{|C(0,q_\perp|^2}{[w-w(q_\perp)]^2+(\frac{\Gamma}{2})^2}\, 2\pi q_\perp dq_\perp \quad (1)$$

Where w (k) represents the phonon dispersion, Γ is the full width at half maximum (FWHM) of the reference bulk Si, C(0,k) is a Fourier coefficient of the confinement function, and quantities the q ≠ 0 phonons participating in the scattering. As the SiNWs are column-shaped crystals, the Fourier coefficients can be written as [27, 28]

$$|C(0,k_1,k_2|^2 \cong e^{-\frac{k_1^2L_1^2}{16\pi^2}} e^{-\frac{k_2^2L_2^2}{16\pi^2}} \left|1-\mathrm{erf}\,(\frac{ik_2L_2}{\sqrt{32\pi}})\right|^2 \quad (2)$$

where L_1 and L_2 are the diameter and the length of the SiNWs, respectively. For the cylindrical nanowire, length >> diameter, which means that the confinement effects mainly occur along the lateral (diameter) direction of the nanowires not along the vertical axis unlike quantum dots.

In order to investigate the clear confinement effect, a plot of the observed FWHM for the first-order optical phonon mode for different diameters is presented in Figure 5.22b. The Raman peaks have larger broadening as the diameter of nanowires decreases. Furthermore, the confinement effect is clearer when the diameter of the nanowires becomes smaller, where FWHM should not decrease more than 5 cm^{-1} as compared to the electronic confinement length (5nm). [29]

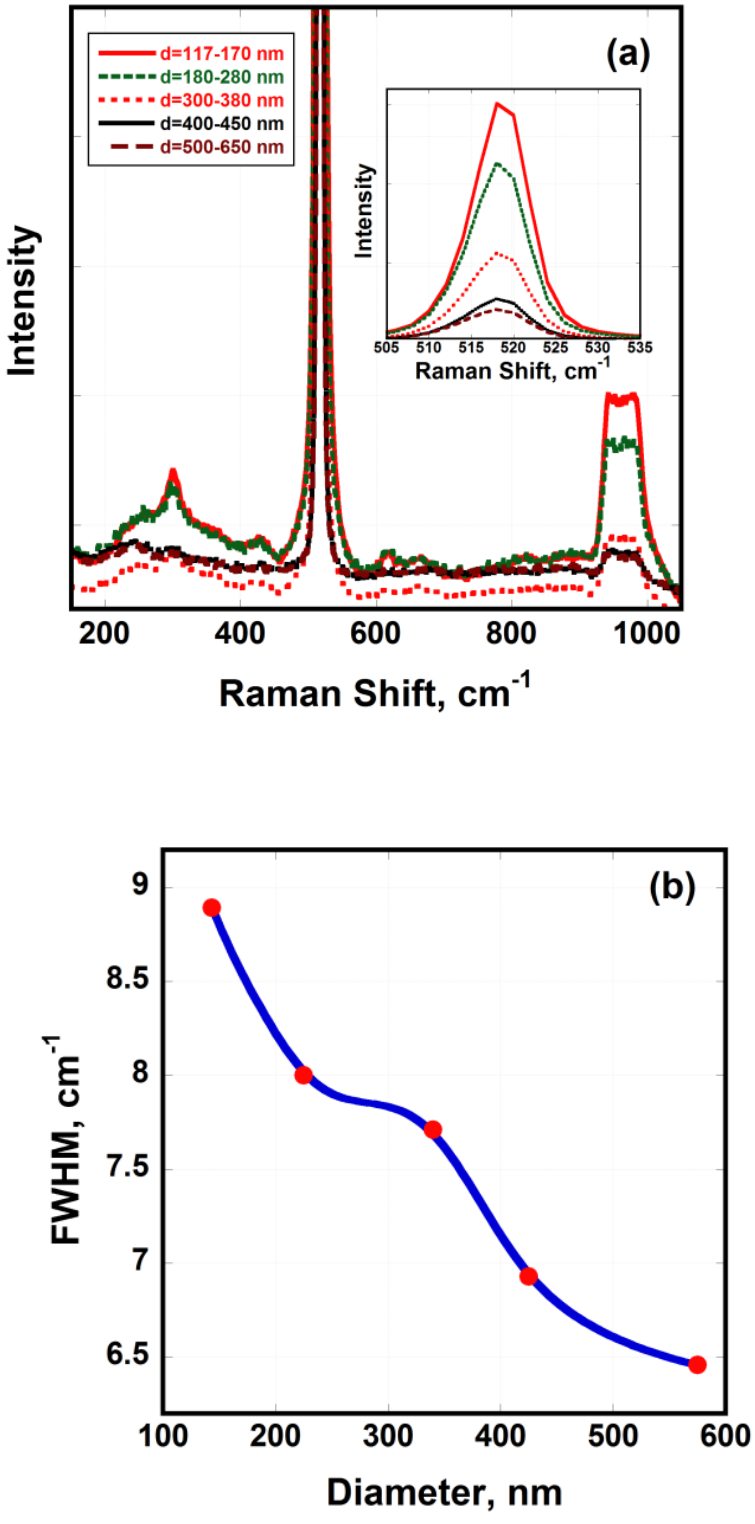

Figure 5.22: (a) Raman spectra of the fabricated SiNWs, and (b) FWHM of the first-order optical phonon mode for SiNWs with different diameters.

5.4 Current-Voltage Characteristics

5.4.1 I-V characteristics in photoelectrochemical cell

The setup of the photochemical cell that has been used for measuring I-V characteristics is shown in Chapter 4 in details. Figure 5.23 shows the I-V curves for different range of SiNW diameters. The obtained photocurrent decreases with increasing the diameter of SiNWs. For example, Figure 5.23a shows the current density of the SiNWs with diameters of 200 nm, the maximum current density was 1.256 mA/cm^2 measured under an applied voltage of 0.25 $V_{Ag/AgCl}$. The current density decreased to 1.109 mA/cm^2 upon increasing the diameter to 350 nm as shown in Figure 5.23b. For diameters in the range of 550 nm, the current density further decreased to 0.7725 mA/cm^2 as shown in Figure 5.23d.

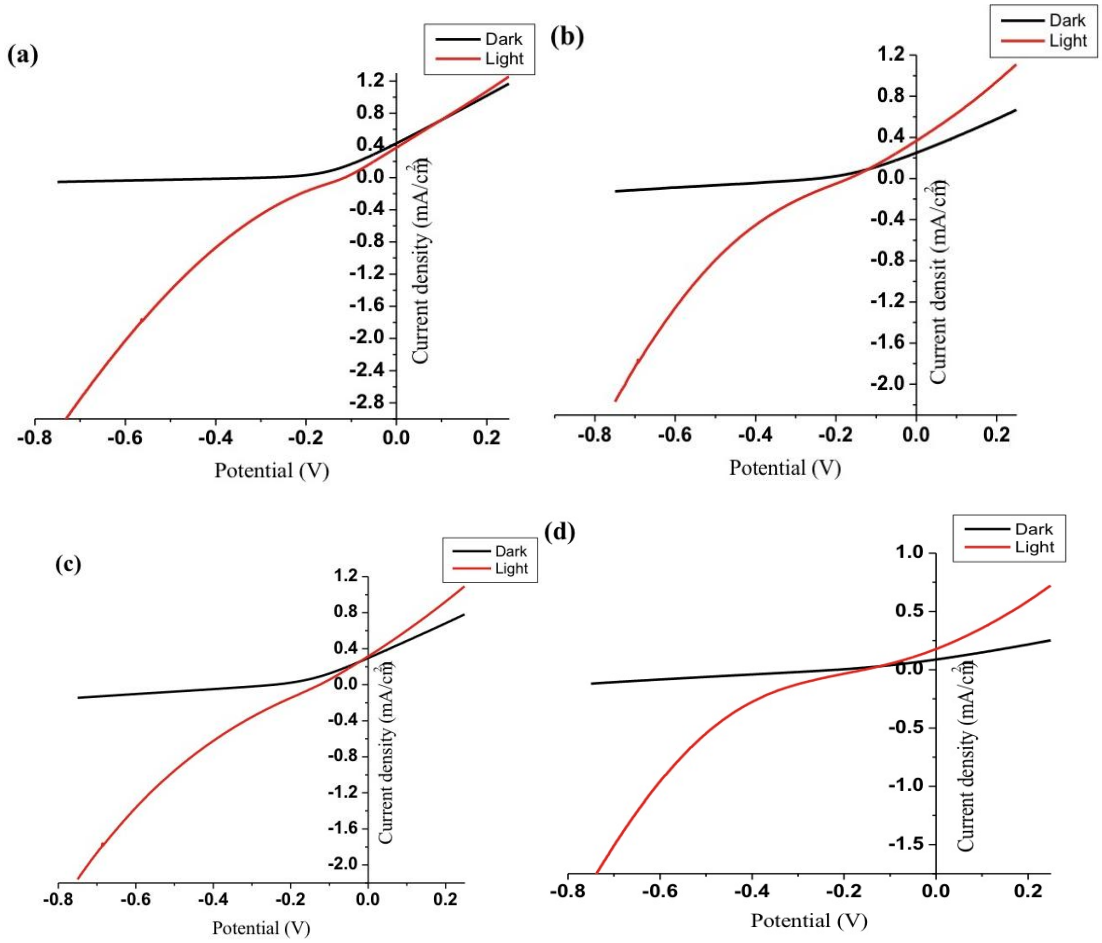

Figure 5.23 I-V curves in dark and light for SiNWs with diameter range (a) 200 nm, (b) 350 nm, (c) 450 nm, and (d) 550 nm.

The relationship between the open circuit voltage (V_{oc}) and the short-circuit current density (J_{sc}) has been studied for different diameters of SiNWs (Figure 5.24). J_{sc} decreases with increasing the diameter of SiNWs. When the diameter range was 200 nm, the J_{sc} was maximum, which is 0.3717 mA/cm^2. With increasing the SiNWs diameter to 550 nm, the J_{sc} decreased to 0.17758 mA/cm^2. Figure 5.25 shows the relationship between J_{sc} and diameter of SiNWs. There is a strong relationship between absorption and short circuit current density (J_{sc}), where the absorption in small diameters increased, increasing the amount of light absorbed and thus increases the J_{sc}. Note that the short circuit current density is proportional to the light absorbance in the wavelength range 300-1000 nm. [30-33]

The measurements of I-V characteristics were also investigated in a mixture of hydrobromic acid (40%) and bromine (3%). The I-V measurements were done for 2 samples that confirmed the effect of changing diameter on the resulted photocurrent as shown in Figure 5.26.

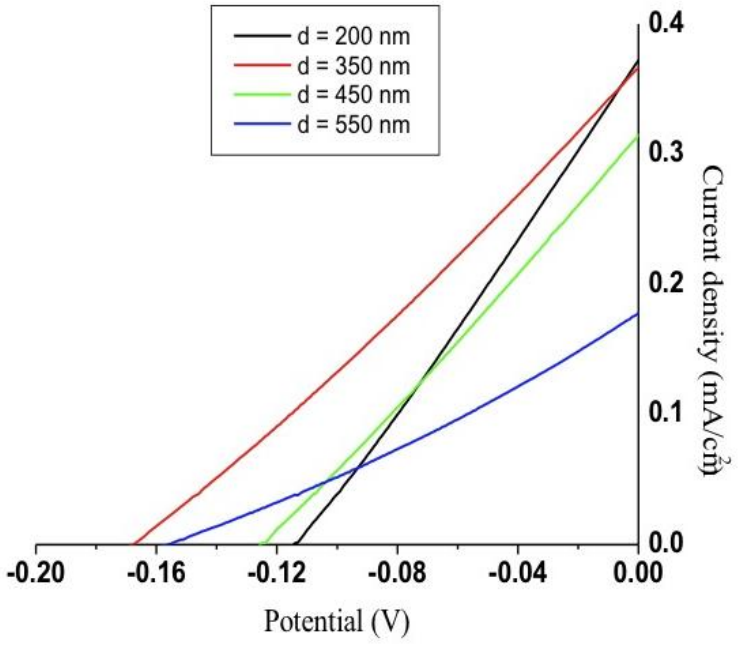

Figure 5.24 J_{sc} Vs. V_{oc} for SiNWs with different diameters

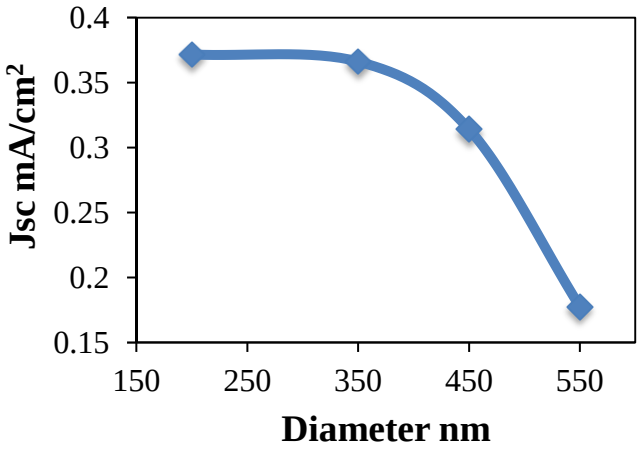

Figure 5.25 relationship between J_{sc} and SiNWs diameter

The dimension of the fabricated SiNWs strongly affects on the resulted photocurrent. The charge carrier separation takes place effectively in small diameters. The Debye length of silicon is an effective factor in determining the obtained photocurrent. The Debye length L_D depends on the doping concentration of the substrate and is given by [34]

$$L_D = \sqrt{\frac{\varepsilon\varepsilon_o kT}{2e^2 N_D}} \quad (5)$$

The Debye length of SiNWs is ~ 170 nm. [36] Consequently, with increasing the diameter of the fabricated SiNWs to more than 170 nm, the recombination rate is faster and easier.

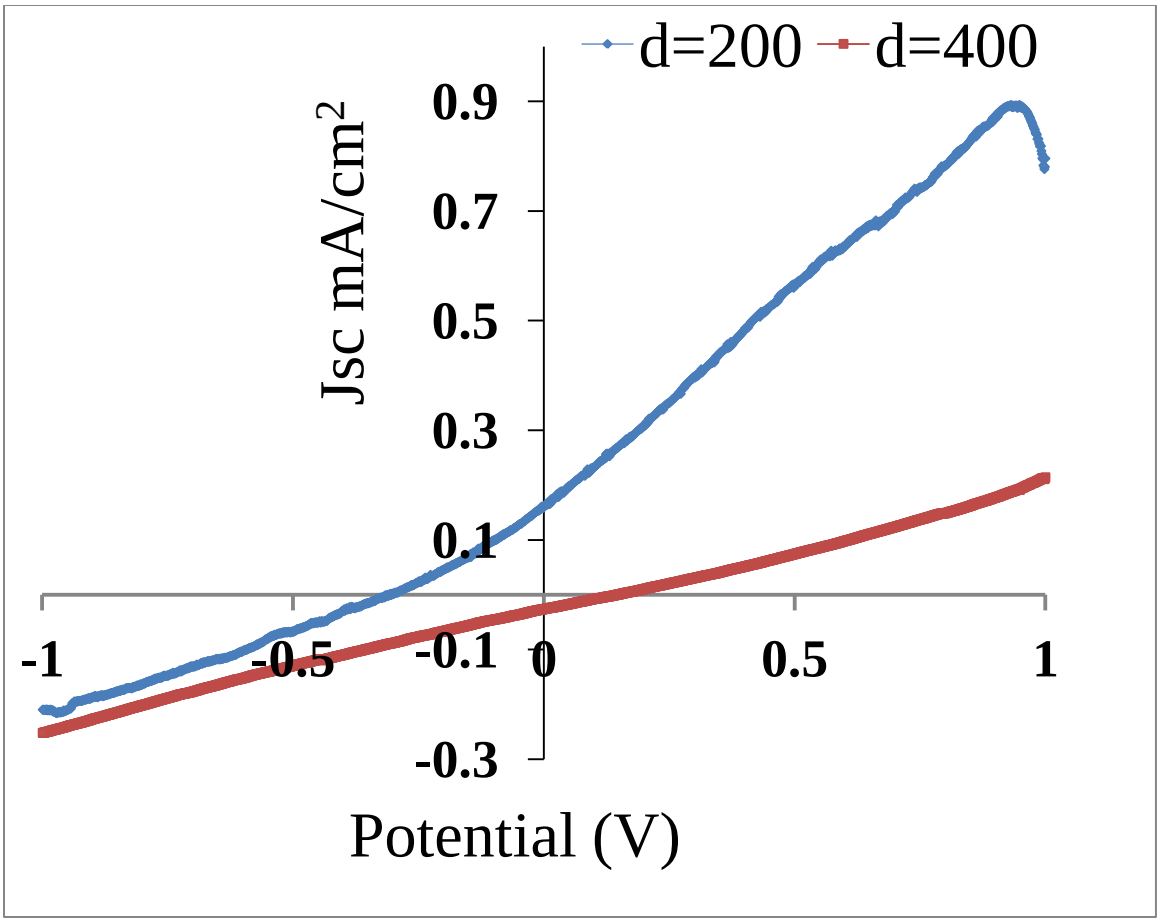

Figure 5.26 I-V curves of SiNWs with different diameters under illumination when electrolyte was a mixture of hydrobromic acid (40%) and bromine (3%).

References

[1] Saporiti, F., et al. "Yttria and ceria doped zirconia thin films grown by pulsed laser deposition." *Materials Research* AHEAD (2013): 0-0.
[2] Pearce, J. M., et al. "Optimization of open circuit voltage in amorphous silicon solar cells with mixed-phase (amorphous+ nanocrystalline) p-type contacts of low nanocrystalline content." *Journal of applied physics* 101.11 (2007): 114301.
[3] Das, R., et al. "Preparation of silver nanoparticles and their characterization." *Journal of Nanotechnology* 5 (2009): 1-6.
[4] Bendersky, Leonid A., and Frank W. Gayle. "Electron diffraction using transmission electron microscopy." *JOURNAL OF RESEARCH-NATIONAL INSTITUTE OF STANDARDS AND TECHNOLOGY* 106.6 (2001): 997-1012.
[5] Peng, Kuiqing, et al. "Aligned Single- Crystalline Si Nanowire Arrays for Photovoltaic Applications." *small* 1.11 (2005): 1062-1067.
[6] Peng, Kuiqing, Xin Wang, and Shuit-Tong Lee. "Silicon nanowire array photoelectrochemical solar cells." *Applied Physics Letters* 92.16 (2008): 163103.
[7] Kind, Hannes, et al. "Nanowire ultraviolet photodetectors and optical switches." *Advanced Materials* 14.2 (2002): 158-160.
[8] Wang, Jianfang, et al. "Highly polarized photoluminescence and photodetection from single indium phosphide nanowires." *Science* 293.5534 (2001): 1455-1457.
[9] Sablon, KimberlyAnnosha. "Polymer single-nanowire optical sensor." *Nanoscale research letters* 4.1 (2008): 94.
[10] Stephens, Richard B., and George D. Cody. "Optical reflectance and transmission of a textured surface." *Thin Solid Films* 45.1 (1977): 19-29. [11] Sivakov, V., et al. "Silicon nanowire-based solar cells on glass: synthesis, optical properties, and cell parameters." *Nano letters* 9.4 (2009): 1549-1554.
[12] Garnett, Erik C., and Peidong Yang. "Silicon nanowire radial p− n junction solar cells." *Journal of the American Chemical Society* 130.29 (2008): 9224-9225.
[13] Krupenkin, Tom N., et al. "From rolling ball to complete wetting: the dynamic tuning of liquids on nanostructured surfaces." *Langmuir* 20.10 (2004): 3824-3827.
[14] Liu, Kong, et al. "Improved photovoltaic performance of silicon nanowire/organic hybrid solar cells by incorporating silver nanoparticles." *Nanoscale research letters* 8.1 (2013): 1-6.
[15] Jeong, Sangmoo, et al. "Hybrid silicon nanocone–polymer solar cells." *Nano letters* 12.6 (2012): 2971-2976.
[16] Park, Kwang-Tae, et al. "Optical properties of Si microwires combined with nanoneedles for flexible thin film photovoltaics." *Optics express* 19.101 (2011): A41-A50.
[17] Li, Junshuai, HongYu Yu, and Yali Li. "Solar energy harnessing in hexagonally arranged Si nanowire arrays and effects of array symmetry on optical characteristics." *Nanotechnology* 23.19 (2012): 194010.
[18] King, David L., Jay A. Kratochvil, and William E. Boyson. *Field experience with a new performance characterization procedure for photovoltaic arrays*. No. SAND--98-3147C; CONF-980735--. Sandia National Labs., Albuquerque, NM (US), 1997.
[19] Xu, Hai Jun, and Xin Jian Li. "Silicon nanoporous pillar array: a silicon hierarchical structure with high light absorption and triple-band photoluminescence." *Optics express*

16.5 (2008): 2933-2941.
[20] Li, Xin Jian, and Yu Heng Zhang. "Quantum confinement in porous silicon." *Physical Review B* 61.19 (2000): 12605.
[21] Popovici, G., et al. "Raman scattering and photoluminescence of Mg-doped GaN films grown by molecular beam epitaxy." *Journal of applied physics* 82.8 (1997): 4020-4023.
[22] Ni, H. Q., et al. "Investigation of Li-doped ferroelectric and piezoelectric ZnO films by electric force microscopy and Raman spectroscopy." *Applied Physics Letters* 79.6 (2001): 812-814.
[23] Johnston, Cliff T., et al. "Single-crystal Raman spectroscopic study of dickite." *American Mineralogist* 83.1 (1998): 75-84.
[24] Piscanec, S., et al. "Raman spectroscopy of silicon nanowires." *PHYSICAL REVIEW-SERIES B-* 68.24 (2003): 241312-R.
[25] Panchal, A. K., and C. S. Solanki. "Fabrication of silicon quantum dots in SiN< i> x</i> multilayer using hot-wire CVD." *Journal of Crystal Growth* 311.9 (2009): 2659-2663.
[26] Li, Bibo, Dapeng Yu, and Shu-Lin Zhang. "Raman spectral study of silicon nanowires." *Physical Review B* 59.3 (1999): 1645.
[27] Richter, H., Z. P. Wang, and L. Ley. "The one phonon Raman spectrum in microcrystalline silicon." *Solid State Communications* 39.5 (1981): 625-629.
[28] Campbell, I. H., and Ph M. Fauchet. "The effects of microcrystal size and shape on the one phonon Raman spectra of crystalline semiconductors." *Solid State Communications* 58.10 (1986): 739-741.
[29] Takagahara, Toshihide, and Kyozaburo Takeda. "Theory of the quantum confinement effect on excitons in quantum dots of indirect-gap materials." *Physical Review B* 46.23 (1992): 15578.
[30] Banerjee, S. K., and Ben G. Streetman. "Solid State Electronic Devices." (2009).
[31] Sze, Simon M., and Kwok K. Ng. *Physics of semiconductor devices*. John Wiley & Sons, 2006.
[32] Kwon, Soonwoo, et al. "Effects of textured morphology on the short circuit current of single crystalline silicon solar cells: Evaluation of alkaline wet-texture processes." *Current Applied Physics* 9.6 (2009): 1310-1314. [33] Wallace, R. L., et al. "Thin silicon string ribbon." *Solar energy materials and solar cells* 48.1 (1997): 179-186.
[34] Martienssen, Werner, and Hans Warlimont. "Springer handbook of condensed matter and materials data." *Springer Handbook of Condensed Matter and Materials Data, Edited by W. Martienssen and H. Warlimont. 2005 XVIII, 1120 p. 1025 illus. With CD-ROM. 3-540-44376-2. Berlin: Springer, 2005.* 1 (2005).

Chapter 6

Simulation Results

6.1 Introduction:

Using of semiconductor materials for nanowires has been increased in the recent years due to their promising properties including electrical, [1] mechanical, [2] optoelectronics, [3] and chemical properties. [4] The most attractive aspect of nanowires is the interaction of sunlight of broad wavelength with the nanowires on substrate, which is improved the optical and optoelectronic applications. Si nanowires have optical anisotropy due to the high aspect ratio and sharp dielectric contrast that is with its surrounding (e.g. glass or air). [5] In addition, sub-wavelength leads to excellent optical properties such as high absorption and low reflectance.

The effect of resonance between nanowires is very effective in improving the optical properties of Si nanowires compared to solid thin film. It has been showed that high light trapping that enhances the short-circuit photocurrent can be obtained by using Si nanowires instead of solid thin film. Thus, the efficiency of solar cell increased as much as 25 %. [6]

6.2 Theory: -

The finite-difference time-domain (FDTD) method is one of the most important tools for electromagnetic simulation methods that is utilized for modeling different nanophotonics components such as light emitting diodes, [7-10] lasers, [11-14] plasmonic cavities, [14-18] waveguides, [19,20] and nanoantennas. [21] The FDTD has the ability of describing behavior of light in many micro- and nano-scale optical system, because it is not restricted by periodic, homogeneous or circular condition compared to analytic Lorentz-Mie solutions. [22,23] For example, the FDTD method can be used successfully for analysis and calculation of the optical resonance of a nanowire that is located on a substrate. [22,24,25] In addition, the FDTD analyzes different materials that have dielectric or magnetic properties. [23]

In our simulations, OptiFDTD [26] software has been used in simulating each Si nanowires array with the incident normal plane wave. The Si nanowires have been modeled by using Lorentz-Drude model.

The main optical excitation, which is limited to a metal/dielectric interface, is the Surface Plasmon Polariton (SPP), as showed by Ritchie. [27] The SPP is hailed from coupled mode that can be utilized to reserve light; as a result, the electromagnetic field is increased that is at an interface between two media. [28-31] Plasmonics in semiconductor materials plays a vital role in designing optoelectronic chips. [32] Optical plasmons are agitated utilizing the interface of metal/dielectric because of the high concentration of high charge carriers in metal, and they have many applications. [28,29] Recently, the SPPs in semiconductor/dielectric interface have attracted interests, and the optical plasmons that have supported by semiconductor/dielectric interface have been numerically studied

without inclusion of losses. [33] The dispersion of SPPs and the resonance frequency rely on the order of interface. [28,33]

For semiconductor, the theory of permittivity is complex because it depends on the doping concentration that determines the free charge carriers in the semiconductor. The plasma frequency of the semiconductor can be determined by the doping concentration and the effective carrier mass. Starting with Drude model to obtain a theoretical model for describing the dielectric function of semiconductor, which is utilized for describing dielectric function of metals. Then, by adding Lorentz model to Drude model, the dielectric function of semiconductor can be described.

For getting dispersion relation, Drude-Lorentz model has been used to describe the dielectric function by solving Maxwell's equation for the interface that is between semiconductor and dielectric. [34]

Lorentz-Drude model has been used in frequency domain. Some complex dielectric function for some surface plasmas and metals are presented by Rakic et al. [35] and can be given as follows:

$$\varepsilon_r(\omega) = \varepsilon_r^f(\omega) + \varepsilon_r^b(\omega) \tag{1}$$

The above form separates the intraband $\varepsilon_r^f(\omega)$ from interband $\varepsilon_r^b(\omega)$ effects where they referred to as free electron and bound-electron effects, respectively. The intraband part can be described by Drude model [36,37] and the interband part can be described by Lorentz model for insulators.

$$\varepsilon_r^f(\omega) = 1 + \frac{\Omega_p^2}{j\omega\Gamma_0 - \omega^2} \tag{2}$$

$$\varepsilon_r^b(\omega) = \left(\sum_{m=1}^{M} \frac{\Omega_p^2}{\omega_m^2 - \omega^2 + j\omega\Gamma_m}\right) \tag{3}$$

where ω is the plasma frequency, m is the number of oscillators with frequency ω_m and lifetime $1/\Gamma_m$, $\Omega_{p=\sqrt{G_m}\omega_p}$ is the plasma frequency as related to intraband transitions with oscillator strength G_0 and damping constant Γ_0. Γ_m is the damping factor and ω_m is the resonant frequency.

A general equation of the Lorentz-Drude model can be given as the follow:

$$\varepsilon_r(\omega) = \varepsilon_{r,\infty} + \sum_{m=1}^{M} \frac{G_m\Omega_m^2}{\omega_m^2 - \omega^2 + j\omega\Gamma_m} \tag{4}$$

where $\varepsilon_{r,\infty}$ is the relative permittivity in the infinity frequency. Ω_m is the plasma frequency. When $m\ and\ \omega_0 = 0$ in the above equation, the equation presents the Drude model as in eq.2. If $m = 1$ and $\Omega_1 = \Omega_2 = \cdots = \Omega_M$ in the above equation, the equation presents the Lorentz model as in eq.3.

4.3 Design: -

To understand how light interacts with the sub-wavelength vertically aligned nanowire arrays and the significant effect of diameter of the SiNWs on reflectivity, a model of SiNW arrays has been performed using finite difference time domain method [38,39] that shows the collective optical resonance between nanowire arrays. In our model, the simplified periodic boundary conditions (PBC) in transverse direction has been used because it can work with other boundary condition such as perfect matched layer (PML) and generates a simple plane-wave simulation. The Si nanowires have been modeled by using Lorentz-Drude model as shown in Figure 6.1.

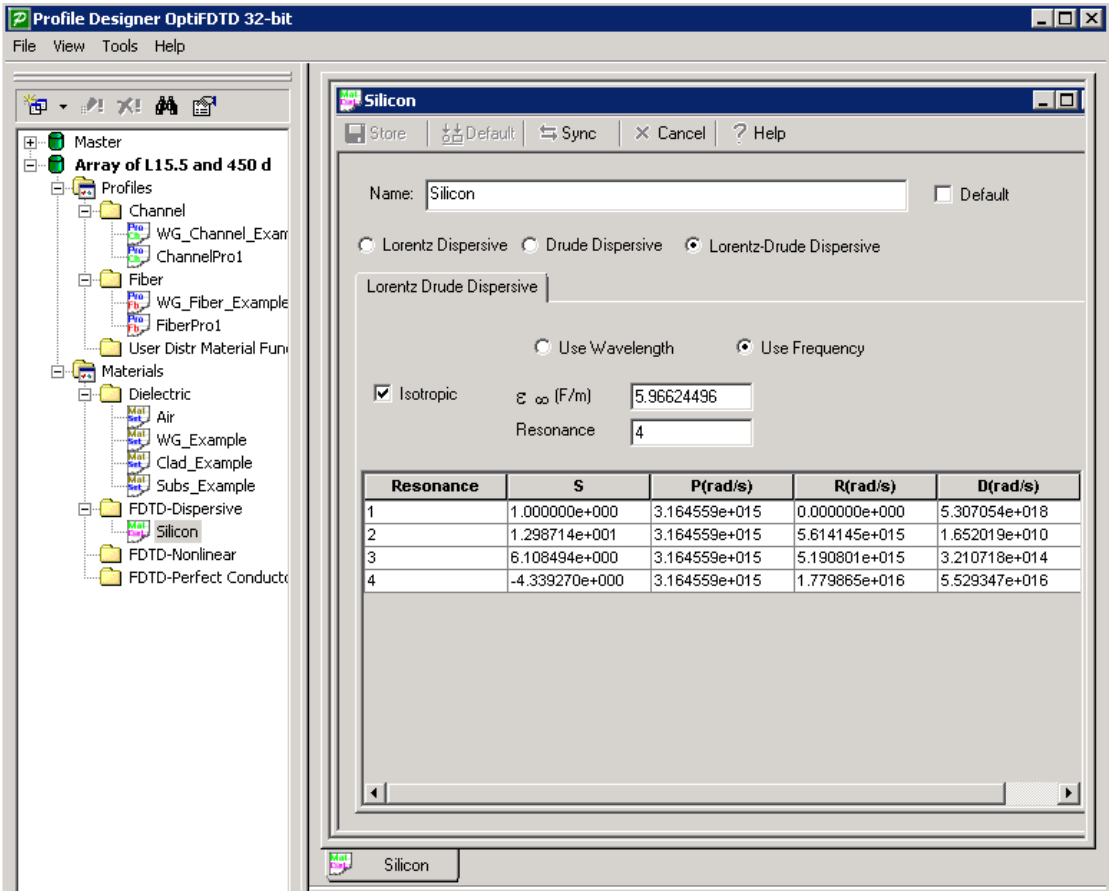

Figure 6.1 Drude-Lorentz module of silicon

where

S = Strength of the corresponding terms
P (rad/s) = Plasma frequency
R (rad/s) = Resonant frequency
D (rad/s) = Damping factor

The calculated absorption spectra is obtained without assuming any surface states. The model size was 2.5 × 2.5 μm with nanowire 10-16 μm in length and 150-400 nm in diameter on top of a 1 μm thick solid Si.

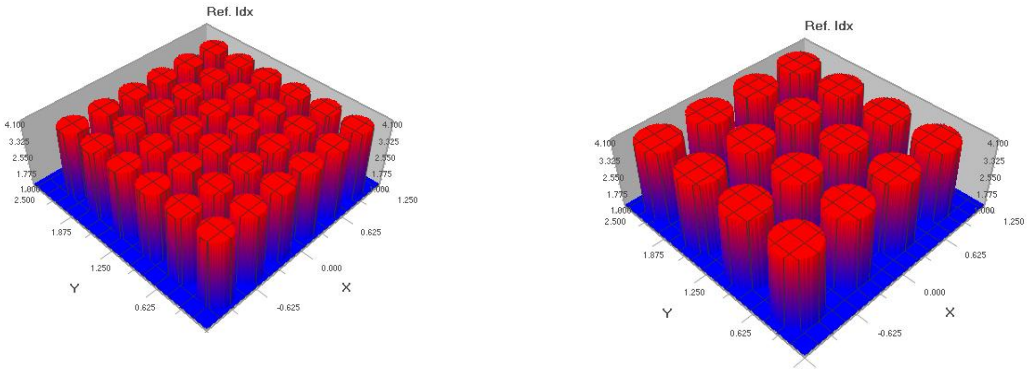

(a) (b)

Figure 6.2 snapshot of our designs for (a) d = 150 nm and (b) d = 400 nm.

4.4 Optical absorption results for different dimensions of Si nanowires: -

Figure 6.3 shows the agreement between the experimental and theoretical values of optical absorption spectra. The values of optical absorption has been obtained when model was 2.5 × 2.5 μm with diameter 150 nm and 10-14 μm in length. As presented, the difference between theoretical and experimental values is ~ 2.5 % at shorter wavelength because of the small roughness of the etched silicon.

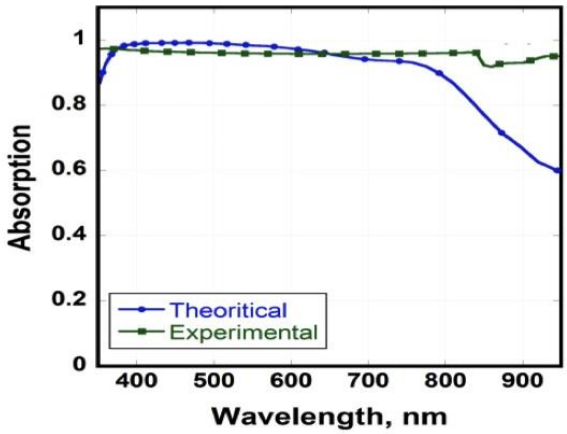

Figure 6.3 Comparison of the experimental and FDTD simulated absorption for the SiNWs of diameter 150 nm.

Another effect that already studied by using OptiFDTD simulation in this work is the effect of changing diameter of nanowires on absorption. The increase of SiNW's diameter leads to decrease in absorption as shown in Figure 6.4.

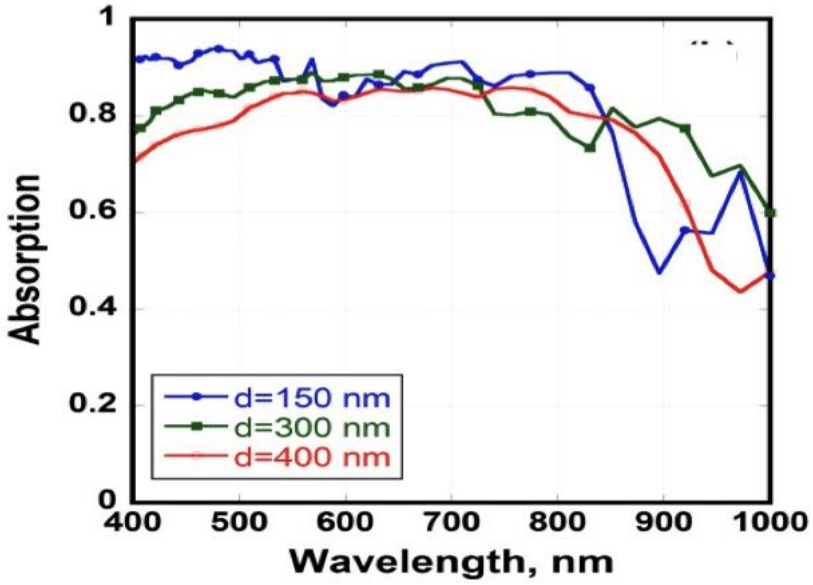

Figure 6.4 absorption vs. wavelength for different diameters of SiNWs

In these simulations, the diameter has been changed from 150 to 400 nm and length from 10 to 14 μm. The optical absorption of SiNWs is measured at wavelength range 350-950 nm. The peak of absorption increases with decreases of diameter and theses results match with our experimental results (Figure 6.4). At long wavelengths, the absorption of nanowires is very low that allows the light to penetrate through the nanowires and reflect back the silicon interface. The absorption of nanowires with different incident light angles are also simulated and shows that the absorption decreases with increasing the incident light angle as shown in Figure 6.5.

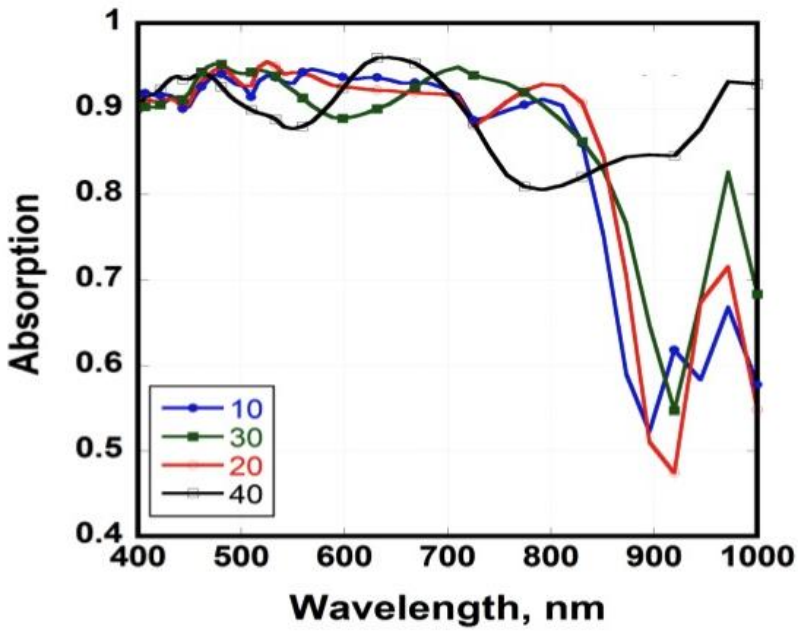

Figure 6.5 the relationship between the optical absorption and wavelength at different incident light angles.

References: -

[1] Zheng, Gengfeng, et al. "Synthesis and Fabrication of High-Performance n-Type Silicon Nanowire Transistors." Advanced Materials 16.21 (2004): 1890-1893.
[2] Nam, Chang-Yong, et al. "Diameter-dependent electromechanical properties of GaN nanowires." Nano letters 6.2 (2006): 153-158.
[3] Qian, Fang, et al. "Gallium nitride-based nanowire radial heterostructures for nanophotonics." Nano letters 4.10 (2004): 1975-1979.
[4] Zhang, Y., et al. "Control of catalytic reactions at the surface of a metal oxide nanowire by manipulating electron density inside it." Nano Letters 4.3 (2004): 403-407.
[5] Qi, Jifa, Angela M. Belcher, and John M. White. "Spectroscopy of individual silicon nanowires." Applied physics letters 82.16 (2003): 2616-2618.
[6] Shah, Arvind V., et al. "Basic efficiency limits, recent experimental results and novel light-trapping schemes in a-Si: H, μc-Si: H andmicromorph tandem'solar cells." Journal of Non-Crystalline Solids 338 (2004): 639-645.
[7] Qian, Fang, et al. "Core/multishell nanowire heterostructures as multicolor, high-efficiency light-emitting diodes." Nano letters 5.11 (2005): 2287-2291.
[8] Kim, Sun-Kyung, et al. "High-efficiency vertical GaN slab light-emitting diodes using self-coherent directional emitters." Optics express 18.11 (2010): 11025-11032.
[9] Ee, Ho-Seok, et al. "Design of polarization-selective light emitters using one-dimensional metal grating mirror." Optics express 19.2 (2011): 1609-1616.
[10] Kim, Sun-Kyung, et al. "Design of out-coupling structures with metal-dielectric surface relief." Optics Express 20.15 (2012): 17230-17236.
[11] Duan, Xiangfeng, et al. "Single-nanowire electrically driven lasers." Nature 421.6920 (2003): 241-245.
[12] Park, Hong-Gyu, et al. "Electrically driven single-cell photonic crystal laser." Science 305.5689 (2004): 1444-1447.
[13] Gradečak, Silvija, et al. "GaN nanowire lasers with low lasing thresholds." Applied Physics Letters 87.17 (2005): 173111.
[14] Park, Hong-Gyu, et al. "Microstadium single-nanowire laser." Applied Physics Letters 91.25 (2007): 251115-251115.
[15] Seo, Min-Kyo, et al. "Full three-dimensional subwavelength high-Q surface-plasmon-polariton cavity." Nano letters 9.12 (2009): 4078-4082.
[16] Kwon, Soon-Hong, et al. "Subwavelength plasmonic lasing from a semiconductor nanodisk with silver nanopan cavity." Nano letters 10.9 (2010): 3679-3683.
[17] Kang, Ju-Hyung, et al. "Ultrasmall subwavelength nanorod plasmonic cavity." Optics letters 36.11 (2011).
[18] Kang, Ju-Hyung, Hong-Gyu Park, and Soon-Hong Kwon. "Room-temperature high-Q channel-waveguide surface plasmon nanocavity." Optics express 19.15 (2011): 13892-13898.
[19] Park, Hong-Gyu, et al. "A wavelength-selective photonic-crystal waveguide coupled to a nanowire light source." Nature Photonics 2.10 (2008): 622-626.
[20] Barrelet, Carl J., et al. "Nonlinear mixing in nanowire subwavelength waveguides." Nano letters 11.7 (2011): 3022-3025.
[21] Kang, Ju-Hyung, et al. "Low-power nano-optical vortex trapping via plasmonic diabolo nanoantennas." Nature communications 2 (2011): 582.

[22] Cao, Linyou, et al. "Semiconductor nanowire optical antenna solar absorbers." Nano letters 10.2 (2010): 439-445.
[23] Taflove, A., and S. C. Hagness. "Computational Electrodynamics: The Finite-Difference Time-Domain Method (Artech House, 2005)." Artech House, Norwood, MA.
[24] Kempa, Thomas J., et al. "Coaxial multishell nanowires with high-quality electronic interfaces and tunable optical cavities for ultrathin photovoltaics." Proceedings of the National Academy of Sciences 109.5 (2012): 1407-1412.
[25] Kim, Sun-Kyung, et al. "Tuning light absorption in core/shell silicon nanowire photovoltaic devices through morphological design." Nano letters 12.9 (2012): 4971-4976.
[26] http://optiwave.com/category/products/component-design/optifdtd/optifdtd-application/
[27] Ritchie, R.H, "plasmon losses by fast electrons in thin film" Physical Review 1975, 106, 874-881.
[28] Raether, Heinz. Springer tracts in modern physics. Vol. 111. Springer-Verlag., 1988.
[29] Maier, Stefan Alexander. Plasmonics: Fundamentals and Applications: Fundamentals and Applications. Springer, 2007, 21-39
[30] Deutsch, Bradley, and Lukas Novotny. "Common-path interferometer rendering amplitude and phase of scattered light." U.S. Patent No. 7,876,450. 25 Jan. 2011.
[31] Zayats, Anatoly V., Igor I. Smolyaninov, and Alexei A. Maradudin. "Nano-optics of surface plasmon polaritons." Physics reports 408.3 (2005): 131-314.
[32] Yao, Bo, et al. "A model for the frequency dispersion of the high-k metal-oxide-semiconductor capacitance in accumulation." Applied Physics Letters 100.22 (2012): 222903.
[33] Pištora, J., et al. "Surface plasmon structures with ferromagnetic thin films." 18th Czech-Polish-Slovak Optical Conference on Wave and Quantum Aspects of Contemporary Optics. International Society for Optics and Photonics, 2012.
[34] Eldlio M, Che F, Cada M, " Lecture notes in engineering and computer science. In : proceeding of the world congress on enginerring and computer science, WCECS 2012, 24-6 oct, 2012, San Francisco, USA, 1078-1081.
[35] Rakic, Aleksandar D., et al. "Optical properties of metallic films for vertical-cavity optoelectronic devices." Applied optics 37.22 (1998): 5271-5283.
[36] Markovic, Mihailo I., and Aleksandar D. Rakic. "Determination of the reflection coefficients of laser light of wavelengths $\lambda \in$ (0.22 μm, 200 μm) from the surface of aluminum using the Lorentz-Drude model." Applied optics 29.24 (1990): 3479-3483.
[37] Marković, M. I., and A. D. Rakić. "Determination of optical properties of aluminium including electron reradiation in the Lorentz-Drude model." Optics & Laser Technology 22.6 (1990): 394-398. [38] S.T. Chu and S. K. Chaudhuri, J. Lightwave Technol. 7, 2033-2038 (1989).
[39] Shih, Min-Yi, et al. "Strong broadband optical absorption in silicon nanowire films." Journal of Nanophotonics 1.1 (2007): 013552-013552.

Chapter 7
Conclusion and Future Work

7.1 Conclusion

From chapters 5 and 6 the conclusions are:

- Single crystalline vertically-oriented Si nanowires can be fabricated with different diameters by metal assisted chemical etching method.
- The diameter of Si nanowires increases with increasing the etching time at temperatures in the range 60 – 80 ^{o}C.
- The absorption of SiNWs is strongly dependent on the diameter of the nanowires, where it increases with decreasing the diameter.
- Changing of the angle of incident light also affects on the amount of optical absorption. The average light absorption of Si nanowires with different diameter decreases with increasing the incident angles from 10-40^{o} in the wavelength range 350 and 850 nm.
- HR-TEM and all XRD diffraction peaks confirmed the presence of c-Si, indicating the high crystallinity of the fabricated nanowires. There is not any amorphous layer around the fabricated Si nanowires.
- All the Raman peaks have a red shift and are broadened compared to bulk c-Si.
- The confinement effect is obvious for all diameters as they have full width half maximum larger than 5 nm.
- The SiNWs show significant PL emission spectra with two peaks lying between 380 and 670 nm. The PL intensity increases with increasing the etching time till 16 min and then start to decreases at 19 min, then increases again due to porosity of SiNWs with an observed red shift.
- The I-V curves for different SiNW diameters showed that the small diameter has high short circuit current density and vice versa.
- The finite difference time domain simulations of silicon nanowires confirmed that the change of diameter has a strong effect on the optical properties of nanowires.
- Changing the diameter of Si nanowires has affected the absorption, where it increased with decreasing the diameter of SiNWs.
- The simulation results are in agreement with the measured absorption of the fabricated Si nanowires.
- The effect of changing incident light angle also studied by FDTD, where the absorption decreases with increasing the angle of incident light.

7.2 Future Work

- The second method of measuring I-V characterization that is p-n junction can be formed by depositing p-type Si on the fabricated n-SiNWs and then depositing metal contact on the two sides for connection as shown in Figure 7.1.

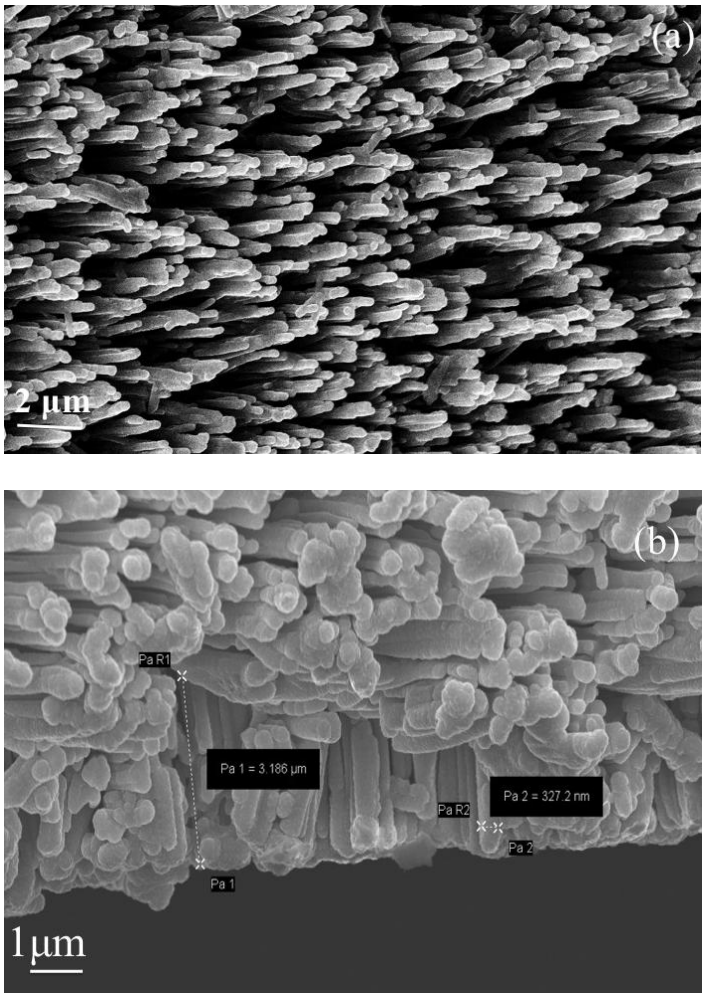

Figure 7.1 (a) , (b) FESEM of n-SiNWs after deposition by p-type Si, and (c) Schematic present the design of p-n junction based on SiNWs

Publications

[1] Abd el Razek, Sara H., Nageh K. Allam, and Mohamed Swillam. "Silicon Nanowires with controlled diameters for energy conversion applications." *Frontiers in Optics*. Optical Society of America, 2013.
[2] Sara Abdel Razek, Mohamed A. Swillam and Nageh K. Allam " Vertically-aligned crystalline silicon nanowires with controlled diameters for energy conversion applications: experimental and theoretical insights" *Journal of Applied Physics* 115, 2014.
[3] Sara Abdel Razek, Nageh K. Allam and Mohamed A. Swillam " Dependence of the I-V characteristics of SiNWs on their diameters" Under preparation.